

EFFECTS OF EDGE ROUGHNESS ON OPTICAL SCATTERING FROM  
PERIODIC MICROSTRUCTURES

by

Brent C. Bergner

A dissertation submitted to the faculty of  
the University of North Carolina at Charlotte  
in partial fulfillment of the requirements  
for the degree of Doctorate of Philosophy in  
Optical Science and Engineering

Charlotte

2009

Approved By:

---

Dr. Thomas J. Suleski

---

Dr. Angela D. Davies

---

Dr. Greg Gbur

---

Dr. Vasily Astratov

---

Dr. Michael A. Fiddy

---

Dr. Robert J. Hocken

© 2009  
Brent C. Bergner  
ALL RIGHTS RESERVED

## ABSTRACT

BRENT C. BERGNER. Effects of edge roughness on optical scattering from periodic microstructures. (Under the direction of DR. THOMAS J. SULESKI)

Planar photonic crystals and other microstructured surfaces have important applications in a number of emerging technologies. However, these structures can be difficult to fabricate in a consistent manner. Rapid, precise measurements of critical parameters are needed to control the fabrication process, but current measurement techniques tend to be slow and often require that the sample be modified in order to make the measurement. Optical scattering can provide a rapid, non-destructive, and precise method for measuring these structures, and optical scatterometry is a good candidate technique for measuring micro-structured surfaces for process control. However, variations in the profile, such as those caused by edge roughness, can make significant contributions to the uncertainty in scatterometry measurements. Because of the multi-dimensional nature of the problem, modeling these variations can be computationally expensive. This dissertation examines the effects of edge roughness on optical scatterometry signals. Rigorous numerical simulations show that the effects of edge roughness are sensitive to the correlation length and the frequency content of the roughness as well as its amplitude. However, these rigorous calculations are computationally expensive. A less computationally expensive model based on a generalized Bruggeman effective medium approximation is developed and shown to be effective for modeling the effects of short correlation length edge roughness on optical scatterometry signals.

## DEDICATION

I would like to dedicate this thesis to my parents, Charles and Alice Bergner, who have worked hard and always given me support and encouragement in all of my endeavors.

## ACKNOWLEDGEMENTS

I would like to acknowledge the help and support of all of my committee members as well as the other faculty and staff in the Department of Physics and Optical Sciences and the Center for Optoelectronics and Optical Communications at UNC Charlotte. I would especially like to thank Lou Deguzman, Robert Hudgins, Bruce Dudley and Alec Martin for their help in developing processes and utilizing the micro-fabrication facilities. I would also like to thank my fellow students for their loans of equipment and for the hours of commiseration. I would especially like to thank Pradeep Srinivasan, Aaron Cannistra, and Zachary Roth for their help on fabrication related issues.

Special thanks to Raymond “Tipper” Rumpf for helping me with the plane wave expansion code and related electromagnetic modeling problems and to Yi-Chen Chuang for our many insightful discussions on these subjects.

I would like to acknowledge Christopher Raymond and Yongdong Liu at Nanometrics for helping me to identify the problem of LER in optical scatterometry measurements and for allowing me access to one of their tools.

I appreciate the input from my friends and colleges at the National Institute of Standard and Technology. These include George Orgi, Heather Patrick, Jeaseong Hwang, Akira Hamamatsu, Gregg Gallatin. Special thanks to Martin Foldyna for reviewing my manuscript. Finally, I am very grateful to Thomas A. Germer for all of his help and for his patience.

This work was partially supported through the National Science and Engineering Initiative of the National Science Foundation under NSF Award Number DMI-0327077 and by the Charlotte Research Institute.

## TABLE OF CONTENTS

CHAPTER 1: INTRODUCTION	1
1.1. Application of Micro/Nano-Structured Surfaces	2
1.2. Techniques for Fabricating Micro/Nano-Structured Surfaces	8
1.3. Metrology for Micro/Nano Structured Surfaces	10
1.3.1 Optical Microscopy	10
1.3.2 Electron and X-Ray Microscopy	11
1.3.3 Scanning Probe Microscopy	12
1.3.4. Optical Scattering Techniques	13
CHAPTER 2: BACKGROUND	16
2.1. Optical Scattering	16
2.2. Uncertainty in Model Based Measurements	19
2.3. Edge Roughness	24
CHAPTER 3: THEORY	31
3.1. Rigorous Electromagnetic Modeling Techniques	32
3.1.1. Plane Wave Expansion (PWE) Method	33
3.1.2. Rigorous Coupled Wave Analysis (RCWA)	39
3.2. Volume Current Perturbation Theory	42
3.3. Effective Medium Approximations	48
3.3.1. Form Birefringence Approximations	49
3.3.2. Maxwell Garnett Effective Medium Approximation	51
3.3.3. Bruggeman Effective Medium Approximation	53

CHAPTER 4: NUMERICAL RESULTS	58
4.1. Rigorous Models of Gratings with LER	60
4.2. Effects of Roughness Parameters on the Scatterometry Signal	61
4.3. Optimization of ABEMA Parameters for a Specific Example	64
4.4. Limits of Extension of Optimized Model to Other Examples	67
CHAPTER 5: CONCLUSIONS	71
REFERENCES	75
APPENDIX A: OPTICAL SCATTEROMETRY INSTRUMENTS	97
APPENDIX B: MEASUREMENT OF NOMINAL GRATING PARAMETERS	101
APPENDIX C: ROUGHNESS ARTIFACT	107
APPENDIX D: EXPERIMENTAL DATA FROM ROUGH GRATINGS	114
APPENDIX E: SCATMECH MODELS	118
APPENDIX F: MATLAB™ m-Files	127

## CHAPTER 1: INTRODUCTION

Micro-structured and engineered surfaces have applications in such diverse disciplines as biology, chemistry, mechanical engineering and the optical sciences.

Evans and Bryan<sup>1</sup> define *engineered surfaces* as

*surfaces where the manufacturing process is optimized to generate variation in geometry and/or near surface material properties to give a specific function*

while *structured surfaces* are

*surfaces with a deterministic pattern of usually high aspect ratio geometric features designed to give a specific function*

This dissertation is primarily concerned with micro-structured surfaces, specifically, as they are applied to engineering the optical dispersion characteristics of materials. However, for both types of surfaces, it is important to quickly and accurately measure a small set of critical parameters that can be used to control the fabrication process<sup>2</sup>. Techniques based on mechanical stylus instruments, atomic force microscopy, scanning electron microscopy, or various optical instruments can be used to measure surface topography. However, each of these techniques has its advantages and limitations<sup>3</sup>. Optical scattering can provide a rapid, non-destructive method for measuring the properties of a surface. This dissertation explores the effects that edge roughness has on the results of a particular measurement technique, referred to as *optical scatterometry*, that uses optical scattering to determine the parameters of periodic micro-structures.

### 1.1. Application of Micro/Nano-Structured Surfaces

Improvements in metrology techniques and standards have been a driving force in sustaining the continued development of micro-lithography for fabrication of semiconductor electronics<sup>4</sup>. In addition to semiconductor electronics, micro- and nano-structured surfaces have applications in a number of other emerging technologies. For example, hydrophobic surfaces have been created using surface structure<sup>5</sup>. By structuring the surface, air can be trapped at the interface, further lowering the total surface energy and increasing the contact angle. These types of structures can be created using selective etching techniques and might be used to reduce frictional drag on the hulls of watercraft or to prevent condensation or ice build up on airplane wings<sup>6</sup>. It has also been suggested that structured hydrophobic and hydrophilic surfaces might be used to pin interfaces and guide flows in micro-fluidic devices<sup>7</sup>. The lotus leaf has a structured surface that tends to make it hydrophobic. As droplets move along these surfaces of the leaf they have tendency to transport contaminants, suggesting the possibility of fabricating a micro-structured, “self-cleaning” surfaces<sup>8</sup> with the potential for high volume household and commercial applications.

Micrometer scale features can also be used to improve the friction and wear characteristics of engineering surfaces<sup>9</sup>. The structures are thought to trap wear debris and act as reservoirs for lubricant<sup>10</sup>. Structuring the surface can also result in an increase in the hydrodynamic pressure, extending the elastohydrodynamic lubrication regime to lower sliding velocities, thereby reducing wear during starting and stopping<sup>11</sup>.

Structured surfaces can even aid in bone<sup>12</sup> and tissue<sup>13</sup> growth and attachment. Currently, much of the research in this area seems to be concerned with improving the

performance of dental implants<sup>14</sup>, but may also have implications for patient specific bone and tissue grafts in other parts of the body<sup>13</sup>.

In optical applications, micro-structured surfaces can act as surface relief diffractive optical elements (DOE)<sup>15-17</sup>. If the period of the structure is less than the wavelength of the light then the higher diffraction orders will be evanescent. In some cases, the optical properties of these structures may be modeled using an effective medium approximation (EMA)(Figure 1). The grating region is replaced with a homogeneous effective medium layer that has an index of refraction that is some combination of the indices of refraction of the constituent materials<sup>18</sup>. For the component of the incident field with the electric field polarized perpendicular to the grating vector (TE polarization), the effective permittivity ( $\epsilon_{eff}$ ) can be approximated by<sup>17</sup>

$$\epsilon_{eff} = \epsilon_s f + \epsilon_0 (1 - f) \quad (1.1)$$

and for the orthogonal polarization (TM polarization)

$$\frac{1}{\epsilon_{eff}} = \frac{1}{\epsilon_s} f + \frac{1}{\epsilon_0} (1 - f) \quad (1.2)$$

where  $\epsilon_0$  is the permittivity of the host material,  $\epsilon_s$  is the permittivity of the fill material, and  $f = w/P_x$  is the percentage of the total area consisting of the fill material. These sub-wavelength optical structures have been used, for example, to create antireflective surfaces<sup>19-21</sup>. Because the effective index of refraction of the sub-wavelength structured layer depends on the polarization, they can also be used to fabricate polarization sensitive components from homogeneous, isotropic materials<sup>22-26</sup>. Effective medium approximations (EMAs) will be discussed in detail in later chapters as a method for modeling the effect of roughness on optical scattering from periodic microstructures.

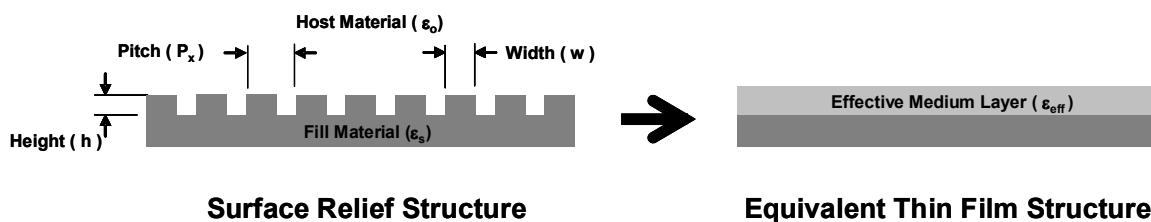


Figure 1 Using an EMA, a sub-wavelength grating can be modeled as a homogeneous effective medium layer with a generally anisotropic index of refraction that is some combination of the indices of refraction of the constituent materials.

Photonic crystals are examples of periodic variations in index of refraction that can be used to engineer the dispersive properties of optical materials<sup>27</sup>. In 1987, Sajeev John wrote a paper where he hypothesized that<sup>28</sup>:

*... carefully prepared three-dimensional photonic superlattices with moderate disorder may provide the key to the predictable and systematic observation of strong localization of photons in nondissipative materials with an everywhere real positive dielectric constant.*

and Eli Yablonovitch proposed that<sup>29</sup>:

*“... full three-dimensional periodicity of  $\lambda/2$  in the refractive index can result in a forbidden gap in the electromagnetic spectrum, near the wavelength  $\lambda$ , irrespective of the propagation direction “*

He went on to directly compare this phenomenon to the periodic electronic potentials used in semiconductor electronics applications. Since the publication of these two papers there has been great interest in the theory, application, and fabrication of these structures<sup>30</sup>.

The origin of the band gap can be explained using a theory developed by Lord Rayleigh in 1887 to explain vibrations of a string under periodically varying tension<sup>27,31,32</sup>. In a region of uniform index, a plot of frequency (energy) with respect to wavenumber (momentum) will be a straight line. This plot is called a *dispersion curve*

and the line is referred to as the *light line*. The slope of the light line is proportional to the group velocity of an electromagnetic wave in the material (Figure 2a). At each point on the dispersion curve, the ratio of the frequency to the wavelength is the phase velocity. When the material index is uniform, this dispersion diagram can be folded back onto itself without any loss of generality, forming multiple bands (Figure 2b). In a material with uniform index, the energy at the edge of the each band will be the same as the energy at the corresponding edge of the next band (see the dashed lines in Figure 2c). However, if a periodic variation is present in the index profile, the frequencies at points of symmetry will become degenerate. Bloch's theorem<sup>33</sup> states that the eigenmodes of this system will also be periodic. Solutions to the wave equation lead to a set of coupled differential equations with modes that are excluded from a range of allowed frequencies. These frequencies are within a photonic bandgap. At intermediate wave vectors between the symmetry points, the band diagram will bend in order to make the curve continuous. Natural examples of this effect can be found in opal gem stones, the iridescent wings of certain insects<sup>34</sup>, and even ancient Roman glass objects, where, over time, minerals leached from the glass leaving a matrix of voids<sup>35</sup>.

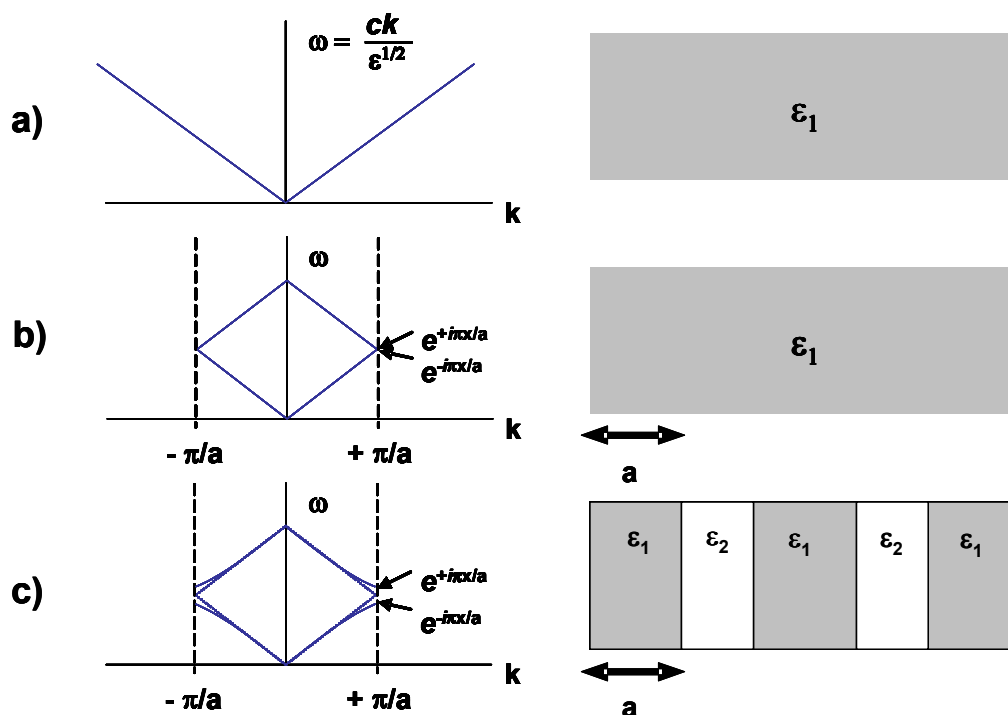


Figure 2 Explanation of the origin of the band gap in photonic crystals based on Lord Rayleigh's argument. a) In an area of uniform permittivity, the dispersion relationship is represented by straight lines with a slope that is proportional to the permittivity. b) The band diagram can be folded periodically without loss of generalization. c) If a periodic change in the permittivity is introduced, then the degeneracy at the edges of the band diagram will be broken. (Based on illustration from Joannopoulos et. al. *Photonic Crystals: Molding the Flow of Light*)<sup>27</sup>.

In regions of the dispersion curve with shallow slope, the group velocity of the light is slowed relative to the bulk properties<sup>36,37</sup>. This effect can be used to create optical delay lines and enhance non-linear optical effects in the material<sup>38</sup>. However, regions where the curve is steep can result in large optical dispersion<sup>39,40</sup>. By introducing controlled defects into these arrays, integrated optical devices such as waveguides, beam splitters, and resonant cavities can be created<sup>25,41</sup>.

Photonic crystals can also be used to improve the extraction efficiency of light emitting diodes (LEDs) used for solid state lighting<sup>42</sup>. Because LEDs produces light

through an electron-hole recombination at a semiconductor heterojunction, the source of the light is embedded within a high-index material. In order for this light to be used for applications such as signaling or solid state lighting, the light must be coupled to a surrounding, low-index medium (air). The Fresnel reflections at the semiconductor/air interface will reflect a significant portion of the light back into the semi-conductor where some of the energy will eventually be lost as heat. In addition, any light that is incident on the interface at large enough angles will be totally internally reflected. Simply roughening the surface can help to frustrate the total internal reflection. Micro-structuring the surface with inverted pyramids can be used to gradually transition from the high-index semi-conductor to the low-index air, essentially impedance matching the two materials<sup>43</sup>. Photonic crystal structures can also be used to increase light extraction by eliminating guided modes within the bandgap and by coupling light into leaky (propagating) modes<sup>44-46</sup>.

Another application of micro-structured surfaces is to improve the collection efficiency of photo-voltaic solar cells used to generate electricity<sup>47</sup>. As with LEDs, the high index contrast between the air and the device material causes losses due to Fresnel reflections. Structures such as the ones mentioned previously can be used to reduce these reflections. In addition, the efficiency of photon to electron conversion within the cell can be improved by either increasing the photon lifetime (the total time that the photon spends in the material) or by increasing the photon density of states (DOS) in the material. Both of these goals can be accomplished by the use of appropriate periodic structures. In the simplest case, a one-dimensional Bragg reflector deposited on the back surface of the cell can increase the physical path length in the material for some range of

frequencies. A two dimensional surface relief pattern on the back surface can further increase the path length by creating internal reflections in multiple directions<sup>48, 49</sup>. The periodic structures can be specifically designed to engineer the dispersion of the host material and increase the DOS in the absorbing region<sup>47,50,51</sup>.

However, for some photonic crystal applications, local variations of the boundary between the high index and low index materials (i.e. edge roughness) can reduce the band gap<sup>52</sup> and increase propagation losses<sup>53-55</sup>. While this may not be significant for applications that operate near the center of the band gap, the effect is pronounced near the band edges<sup>56</sup>. Even with improvements in fabrication techniques, edge roughness is expected to remain a significant problem for applications, such as slow light, that operate near the band edge<sup>53</sup>. In addition, as minimum feature sizes continue to decrease, edge roughness is also becoming an important factor for semiconductor device performance.<sup>57,58</sup>

## 1.2. Techniques for Fabricating Micro/Nano-Structured Surfaces

In many cases micro-structured surfaces can be fabricated using lithographic techniques developed for producing semi-conductor electronics and micro-electro-mechanical systems (MEMS)<sup>59</sup>, taking advantage of the significant resources that have been developed to support these industries. However, the resolution of optical lithography techniques is limited by the wavelength of the light that is used to expose the resist. To an extent the resolution limits of optical lithography can be extended by using a variety of techniques<sup>60</sup> such as: using shorter wavelengths in deep ultraviolet (DUV) or X-ray region of the spectrum; increasing the numerical aperture (NA) of the system by immersing the objective and substrate in a higher index fluid; using structured

illumination; taking advantage of phase shifts in the mask; changing the pattern on the mask to yield the desired result using optical proximity correction (OPC)<sup>61-64</sup>; or exposing the resist multiple times with a small shift in the position of the wafer<sup>65,66</sup>.

For specific applications other fabrication techniques may have advantages over conventional optical lithography. For example, interference lithography has been used to create large areas of periodic structures such as gratings, photonic crystals<sup>67,68</sup>, and patterned magnetic storage media<sup>69</sup>. However, the period of the pattern is limited by the wavelength of the light used in the interference setup.

Electron-beam lithography is capable of very high resolution patterning<sup>70</sup>, which has been used to fabricate planar photonic crystal structures<sup>71</sup> and integrated optical devices<sup>72</sup>. However, writing with an e-beam is a serial process, which is, in general, time consuming, expensive, and limited to planar structures.

Diamond machining is a flexible method for creating such diverse structures as simple gratings, retro-reflective micro-corner-cubes, Fresnel lenses, and free-form optical surfaces<sup>73</sup>. While specialized techniques have been developed for diamond machining ferrous metals, there are a limited number of materials that are suitable for diamond machining. Diamond machining is commonly used in conjunction with molding techniques.

The high production volumes and/or large surface areas required for some of the previously mentioned applications make micro/nano-replication techniques attractive. Micro/nano-replication techniques include nano-imprint lithography<sup>74-76</sup>, compression and injection molding<sup>77-79</sup>, and roll-to-roll (web) processes<sup>73,80,81</sup>. With these techniques, the time, expense, and technical skill that is needed to produce the initial master surface

can be leveraged to produce very complex surfaces on a large scale. There is little reason to think that these processes could not be extended to even smaller structures<sup>82</sup>. However, in order to control the fabrication process a fast, accurate, and non-destructive method for measuring these structures is needed<sup>81</sup>.

### 1.3. Metrology for Micro/Nano Structured Surfaces

Methods that have been used to measure attributes of micro/nano-structured surfaces include optical microscopy, electron microscopy, mechanical profilometry, atomic force microscopy, and scatterometry. Each of these techniques has advantages, limitations, and range of utility. In fact, an adequate picture of the process may only be achieved by using a combination of techniques<sup>83</sup>.

#### 1.3.1. Optical Microscopy

Optical microscopy is a familiar and useful method for examining small structures. As early as the first century A.D., the Roman philosopher Seneca observed that “Letters, however tiny and obscure, are seen larger and clearer through a glass ball filled with water.”<sup>84</sup> The father and son team of Hans and Zacharias Janssen are credited with combining lenses in a tube to create the first compound microscope in the late 16<sup>th</sup> century<sup>85</sup>. By the 19<sup>th</sup> century ruling engines were being used to create finer and finer gratings to compare the resolving power of microscopes until the pitch of the gratings finally exceeded the theoretical resolution limit of the microscopes<sup>86</sup>. Optical microscopy remains a prolific and useful method for observing small objects. The charge couple detector (CCD) camera and image processing software have helped to make the modern compound optical microscope a fast and precise way to measure features in variety of industries. While there are techniques for extending the useful range of optical

microscopy in limited situations<sup>87, 88</sup>, in principle, the resolution of optical microscopes are limited to

$$\Lambda \geq \frac{\lambda}{n \cdot \sin \theta} = \frac{\lambda}{NA} \quad (1.3)$$

for spatially coherent illumination, and

$$\Lambda \geq \frac{\lambda}{2n \cdot \sin \theta} = \frac{\lambda}{2 \cdot NA} \quad (1.4)$$

for spatially incoherent illumination, where  $\Lambda$  is the minimum resolvable period,  $\lambda$  is the wavelength of the light used to make the observation, and  $NA$  is the numerical aperture of the optical system. The numerical aperture is defined as

$$NA = n \sin \theta \quad (1.5)$$

where  $n$  is the index of refraction of the incident medium, and  $\theta$  is the half angle of the cone of incidence.

### 1.3.2. Electron and X-Ray Microscopy

Scanning electron microscopy (SEM) can provided “images” of micro/nano-structured surfaces with a very high effective magnification<sup>89</sup>. While optical microscopes operate with photons at wavelengths on the order of a few hundred nanometers, an electron with an energy 100 keV corresponds to an electron wavelength of twelve picometers. The “images” of an electron microscope are actually a composite result of scattered electrons that are collected as an electron beam is scanned across the surface. The ultimate resolution of the SEM is limited by the size of the interaction volume<sup>89</sup>. The interaction volume depends on several factors, including the energy of the incident electrons and the density of the material. Secondary electrons (SE) are electrons that are scattered with energies less than 50eV. They are typically scattered at large angles, and,

due to their low energies, originate from a small interaction volume, resulting in a high resolution image with resolvable feature sizes on the order of a few nanometers. Back scattered electrons (BSE) are scattered at higher energies. These electrons tend to originate from a larger interaction volume, resulting in lower resolutions (on the order of 10s of nanometers).

SEMs have found wide acceptance and specially calibrated SEMs are in common use in the semiconductor industry<sup>90</sup>. However, due to the high vacuum environment usually needed to obtain acceptable images, SEMs typically require long load times and special sample preparation. In addition, non-conducting substrates tend to accumulate charge during observation, further limiting the useful resolution.

### 1.3.3. Scanning Probe Microscopy

Mechanical profilometry is conceptually one of the simplest metrology methods for examining micro/nano-structured surfaces. A small stylus is moved across the surface of the sample with a controlled contact force. A disadvantage of mechanical profilometry is that the stylus makes physical contact with the surface. While attempts can be made to minimize the force, it cannot be completely eliminated or the stylus would not stay in contact with the surface. In extreme cases some argue that these forces may even permanently deform the surface<sup>91</sup>.

Atomic force microscopy (AFM) is similar to mechanical profilometry because a stylus is moved across the surface. However, instead of making physical contact with the surface, the atomic forces between the probe tip and the surface are measured. Typically, a control algorithm and piezo-electric transducers (PZT) are used to move the stylus in order to maintain a constant force while the position of the stylus is monitored by

observing the movement of a laser beam reflected from a mirror on the stylus. Atomic force microscopes are capable of extremely high resolution images, however, the nature of scanning a probe across the surface and the limitation of the response of the control system limit the throughput of these instruments<sup>3</sup>.

#### 1.3.4. Optical Scattering Techniques

Optical scattering techniques have been used extensively to measure the statistics of rough surfaces<sup>92</sup> and have been used to determine specific profile parameters of periodic microstructures<sup>93</sup>. These techniques do not depend on interpreting an image or a set of data points obtained by scanning a probe across a specific feature. Optical scattering techniques make an aggregate measurement over many features because the signal that is obtained is integrated over the spot size of the instrument.

Periodic features with dimensions on the order of the wavelength of the light that is used to probe the surface typically exhibit multiple diffraction orders, while sub-wavelength scale features only diffract the incident light into the zeroth order. To increase the sensitivity of scattering measurements for smaller structures shorter wavelengths can be used. Small angle x-ray scattering (SAXS) has been demonstrated to accurately measure critical dimensions (CD) with resolutions of less than ten nanometers<sup>94</sup> and has also been shown to be sensitive to side wall angle<sup>95</sup> and line edge roughness<sup>96</sup>. The x-ray source used in these experiments is typically a synchrotron x-ray source. If small, adequately intense laboratory sources can be developed, SAXS may prove to be a powerful technique for CD metrology<sup>90</sup>.

In general, the shape of the structure can not be determined analytically from the scattered signal<sup>97</sup>. However, computational techniques such as rigorous coupled wave

analysis (RCWA) or Green's function eigenanalysis (GFE) can be used to obtain a rigorous solution for the scatter from a hypothetical structure<sup>98</sup>. This solution is compared to experimental data and the structure of a sample can be determined using iterative methods to find the hypothetical structure that produces the same response as the experimental data. However, in practice it is usually determined by comparing the experimental data to a library of previously calculated solutions<sup>99</sup>(Figure 3). This technique is referred to as *optical scatterometry*. Optical scatterometry is becoming an increasingly useful tool for controlling the fabrication of micro/nano-structures used in the semiconductor electronics industry<sup>100-114</sup>, because it is non-destructive and can be used in-line, or even in-situ to control the process<sup>115-117</sup>.

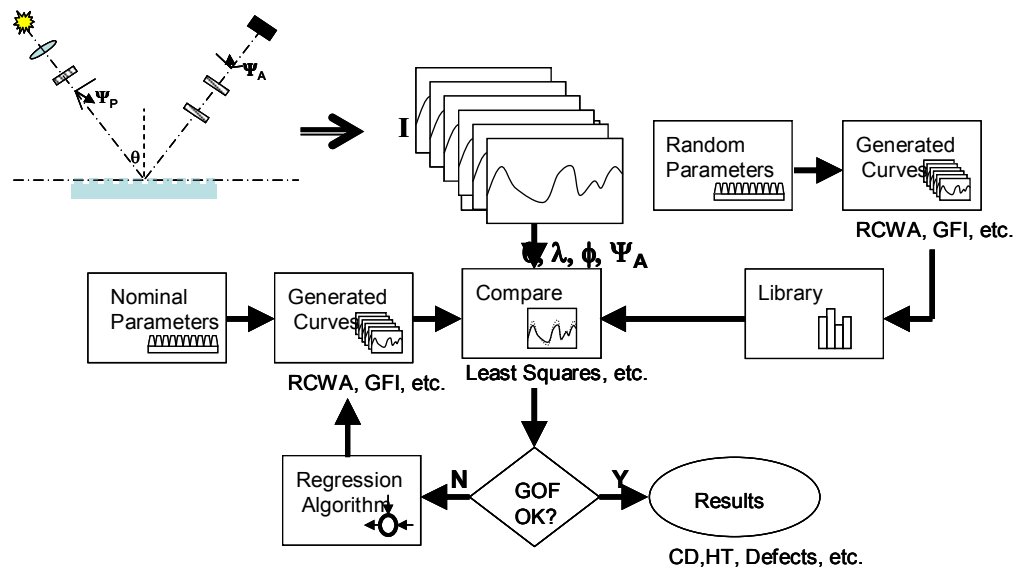


Figure 3. Flow chart of a general scatterometry algorithm illustrating use of libraries of pre-calculated solutions or the use of regression techniques to find the solution to the inverse problem.

This dissertation examines the effect of edge roughness on optical scatterometry signals. The 2007 International Technology Roadmap for Semiconductors identified the

ability to measure *Line Edge Roughness* (LER) as an important part of lithography process control<sup>118</sup>. Furthermore, the ability to measure and control edge roughness may prove to be critical for fabricating planar photonic crystal devices. If a robust, computationally efficient model can be developed for simulating the effects of edge roughness on optical scatterometry signals, it will allow metrologists to incorporate these effects in scatterometry models. This is important for two reasons. First, edge roughness might be measured directly using optical scatterometry if adequate models can be incorporated into the measurement system. Second, even approximate models would be useful in determining the contributions that edge roughness makes to the uncertainties in the estimates of other grating parameters that are measured using optical scatterometry.

In Chapter 2, approximation methods that have traditionally been used to model the effect of surface roughness on optical signals are examined, a method for propagating uncertainties in model based measurements is derived, and a description of line edge roughness (LER) based on self-affine functions is developed. In Chapter 3, some of the rigorous electromagnetic techniques that are used to model grating structures are examined and two approximation methods for use in modeling the effects of edge roughness on these structures are derived. In Chapter 4, a model for edge roughness based on a generalized anisotropic Bruggeman effective medium approximation (ABEMA) is developed and compared the results of rigorous calculations. Finally, in Chapter 5 the work is summarized and some possible future directions for research are discussed.

## CHAPTER 2: BACKGROUND

### 2.1. Optical Scattering

Optical scattering can refer to any number of phenomena concerning the interaction of optical radiation with matter<sup>119</sup>. In the context of this dissertation, except for a brief discussion of the historical application of diffuse scattering measurements to measure surface roughness statistics, optical scattering refers specifically to the interaction between incident optical radiation and periodic surface relief structures as measured by the specular reflectance (i.e. zeroth order diffraction efficiency).

Optical scattering can provide a powerful tool for characterizing surface structure. If the structure can be decomposed into its Fourier components, then each of these components acts as a diffraction grating<sup>120</sup>. The total scatter signature from the surface is a combination of the diffraction patterns from these individual gratings (Figure 4).

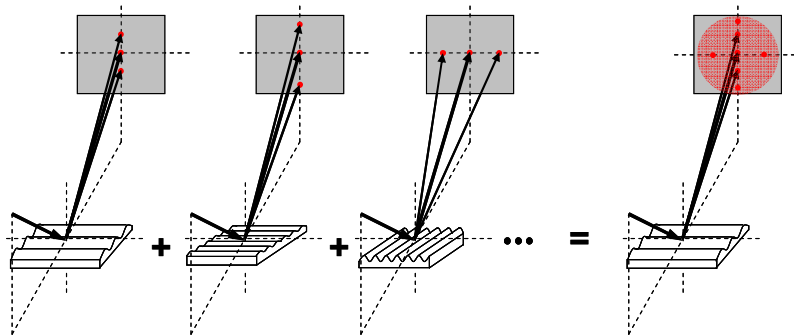


Figure 4. A complex micro-structure can be decomposed into its Fourier components and the total scatter from the surface is a combination of the diffraction patterns from these individual components.

The angular distribution of the diffraction orders from a single grating are given by

$$\Lambda (\sin \theta_d - \sin \theta_i) = m\lambda_0 \quad (2.1)$$

where  $\Lambda$  is the grating period,  $\theta_i$  is the angle of incidence with respect to the surface normal,  $\theta_d$  is the diffraction angle with respect to the surface normal,  $\lambda_0$  is the probe wavelength, and  $m$  is the order number. In the far field, the relative distribution of the energy into each of the diffraction orders can be determined using Kirchoff diffraction theory<sup>92</sup>. The result depends on the grating profile, the incident angle, the orientation of the plane of incidence with respect to the grating vector, and the polarization of the light.

For a relatively smooth surface, the relationship between the surface roughness and the scattered field can be adequately described in terms of small perturbations in the surface height. These perturbations are related to the terms of the Rayleigh expansion of the propagating field<sup>121, 122</sup>. The Rayleigh-Rice perturbation theory uses this observation to relate the power per unit solid angle in the scattered signal ( $dP/d\Omega_s$ ) to the two dimensional power spectral density (PSD) of the surface roughness  $S(f_x, f_y)$  (measured in units of inverse square length) using the formula:

$$\frac{dP/d\Omega_s}{P_i} = \left[ \frac{4\pi}{\lambda^4} \right] \cos \theta_i \cos^2 \theta_s Q S(f_x, f_y) d\Omega_s \quad (2.2)$$

where  $\theta_i$  is the angle of incidence,  $\theta_s$  is the angle of observation,  $\frac{4\pi}{\lambda^4}$  is a term that describes the wavelength dependence of the Rayleigh scattering,  $\cos \theta_i \cos^2 \theta_s$  is an obliquity factor, and  $Q$  is a term describing the specular reflectivity of the perfectly smooth surface (Figure 5). However, the Rayleigh-Rice perturbation theory is limited to

surfaces where that the average height of the roughness is much less than the wavelength and the surface slopes are small<sup>123</sup>.

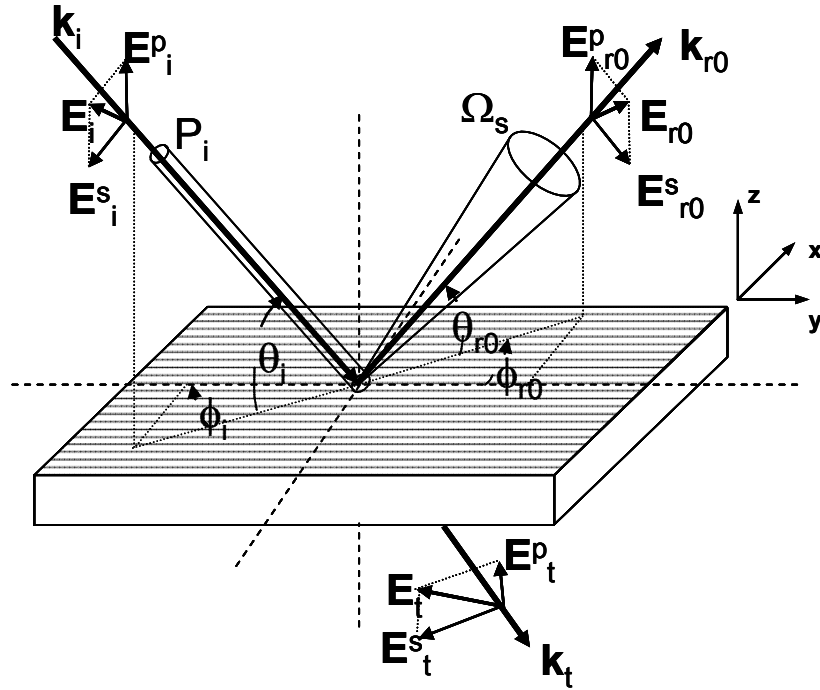


Figure 5. Definitions of the variables used describing optical scattering from a periodic structure.

If the period of the roughness is much less the wavelength of the incident light,

$$\frac{\lambda_0}{\Lambda} \geq 2 \quad (2.3)$$

then only the zero order diffraction peak (specular reflection) will be present. All of the other orders will be evanescent for every incident angle. However, information about the structure is still available by observing the dependence of the magnitude and phase of the reflectivity of the surface as a function of the angle of incidence, the wavelength of the incident light, and the incident polarization. Measurement of these parameters can be used to gain further information about the surface structure by modeling the scattered

signal using rigorous electromagnetic modeling techniques and finding a solution to the inverse problem.

In general, the term *scatterometry* can refer to any technique that uses observation of a scattered signal to determine the properties of the scattering medium or surface. This would include the techniques discussed so far. However, in semiconductor metrology applications the term scatterometry refers to a more specific set of techniques in which the scattered signal is compared to theoretical predictions of scattered signals from hypothetical models of the surface. Since, in general, the surface profile cannot be determined analytically from the scattered signal, the models are adjusted until the theoretical data can be fit to the experimental data within an acceptable uncertainty. Naqvi et. al. proposed using scattering measurements in this manner in 1992<sup>124</sup>. While the inverse solution cannot be shown to be unique, by applying appropriate constraints from *a priori* knowledge of the structures that are being fabricated, the technique can be used as an acceptable method for semiconductor process control<sup>83,102-105,108-111,113-117</sup>. Several companies have introduced commercially available metrology platforms using this principle. Descriptions of two instruments that used to take optical scatterometry measurements are included in Appendix A. A detailed example of an optical scatterometry measurement is included in Appendix B.

## 2.2. Uncertainty in Model Based Measurements

Given  $N$  sets of data  $\{x_i, y_i\}$ , where  $y_i$  is an *observation* (for example, a reflectance value  $|R_{ss}|$  or  $|R_{pp}|$ ), with variance  $\sigma_{y_i}^2$ , and  $x_i$  is a vector containing the  $P$  *measurement parameters* describing the conditions under which that observation was made (for example the wavelength, angle of incidence, and azimuthal angle at which the particular

reflectance value was observed, such that  $P = 3$  and  $\mathbf{x}_i = [\lambda_i, \theta_i, \phi_i]^T$ ), each with its own uncertainty  $u_{x_{ij}}$ , the goal of model based measurements is to find the set of  $M$  *model parameters*,  $\mathbf{a} = [a_1, a_2 \dots a_M]^T$ , and their associated uncertainties  $u_{a_m}$ , that optimize some *objective function* ( $S$ ) relating the results from some model to the observations. The assumption is that this optimal set of model parameters is a good estimate of the true values of the parameters. This model can be as simple as an analytic function such as  $f(\mathbf{x}_i, \mathbf{a}) = a_1 x_i + a_2$ , or it can be a relationship that must be calculated through a more complex algorithm (as in the case of RCWA).

The difference between the observed values ( $y_i$ ) and the modeled values ( $f(\mathbf{x}_i, \mathbf{a})$ ) is called the *residual* ( $r$ )

$$r_i = [y_i - f(\mathbf{x}_i, \mathbf{a})] \quad (2.4)$$

A common objective function is the weighted sum of the squares of the residuals

$$S = \sum_{i=1}^N w_i r_i^2 \quad (2.5)$$

where  $w_i$  is some weighting factor for the  $i^{\text{th}}$  residual. If  $w_i = 1$  then  $\sqrt{S/N}$  is the root mean square (RMS) difference between the observed data and the model. Another possible weighting factor, called a *statistical weighting factor*<sup>125</sup>, takes into consideration the possibility of the unequal uncertainties of the data and is given by:

$$w_i = \frac{1}{\sigma_{y_i}^2 + \sum_{j=1}^L \left( \frac{\partial f(\mathbf{x}_i, \mathbf{a})}{\partial x_j} \right)^2 \sigma_{x_{ij}}^2} \quad (2.6)$$

where  $\sigma_{y_i}^2$  is the variance in the  $i^{\text{th}}$  observation,  $\frac{\partial f(\mathbf{x}_i, \mathbf{a})}{\partial x_j}$  is the sensitivity of the  $i^{\text{th}}$  observation to changes in the  $j^{\text{th}}$  measurement parameter, and  $\sigma_{x_{ij}}^2$  is the variance of the  $j^{\text{th}}$

measurement parameter for the  $i^{\text{th}}$  observation. The denominator of (2.6) is simply the combined standard uncertainty in the  $i^{\text{th}}$  observation ( $u_{c_{y_i}}$ ) assuming: no systematic bias in the stated values of the measurement parameters, a normal distribution in the actual values of the measurement parameters about the stated value, and no covariance between the measurement parameters. A more complicated situation (such as including covariance between the measurement parameters) might be considered by using standard techniques to separately determining the combined standard uncertainty of each observation<sup>126</sup>, and then, without any further consideration as to how these uncertainties were determined, continuing with the procedure described in the subsequent text to determine the uncertainties in the model parameters.

The objective function can be optimized by setting its partial derivatives with respect to each of the model parameters to zero<sup>125</sup>. By substituting (2.4) into (2.5) and taking the partial derivative, for each measurement parameter

$$\frac{\delta S}{\delta a_m} = 2 \sum_{i=1}^N w_i r_i \frac{\delta r_i}{\delta a_m} = -2 \sum_{i=1}^N w_i [y_i - f(\mathbf{x}_i, \mathbf{a})] \frac{\delta f(\mathbf{x}_i, \mathbf{a})}{\delta a_m} = 0 \quad (2.7)$$

so that the objective function is optimized when

$$\sum_{i=1}^N w_i y_i \frac{\delta f(\mathbf{x}_i, \mathbf{a})}{\delta a_m} = \sum_{i=1}^N w_i f(\mathbf{x}_i, \mathbf{a}) \frac{\delta f(\mathbf{x}_i, \mathbf{a})}{\delta a_m} \quad (2.8)$$

If  $\alpha$  is the value of  $\mathbf{a}$  when the objective function is optimized, then  $\alpha$  represents the best estimates of the true values of the model parameters. However, since the optimum value of the objective function depends on the values of the measurement parameters ( $x_i$ ) and the observations ( $y_i$ ), each with their own uncertainty, there will an uncertainty in  $\alpha$  given by<sup>127</sup>

$$u_{\alpha_k} \equiv (\alpha_k - a_k) \quad (2.9)$$

Near the optimum value point  $f(\mathbf{x}_i, \mathbf{a})$  can be expanded in a first order Taylor series expansion about  $\mathbf{a}$  such that

$$f(\mathbf{x}_i, \mathbf{a}) = f(\mathbf{x}_i, \mathbf{a}) + \sum_{k=1}^M \frac{\partial f(\mathbf{x}_i, \mathbf{a})}{\partial \alpha_k} (\alpha_k - a_k) \quad (2.10)$$

Substituting (2.10) into (2.8) and assuming that  $\delta f(\mathbf{x}_i, \mathbf{a})/\delta a_m \rightarrow \partial f(\mathbf{x}_i, \mathbf{a})/\partial \alpha_m$  near  $\mathbf{a} = \mathbf{a}$

$$\sum_{i=1}^N w_i y_i \frac{\delta f(\mathbf{x}_i, \mathbf{a})}{\delta a_m} = \sum_{i=1}^N w_i f(\mathbf{x}_i, \mathbf{a}) \frac{\delta f(\mathbf{x}_i, \mathbf{a})}{\delta \alpha_m} + \sum_{i=1}^N \sum_{k=1}^M w_i \frac{\partial f(\mathbf{x}_i, \mathbf{a})}{\partial \alpha_k} \frac{\delta f(\mathbf{x}_i, \mathbf{a})}{\delta \alpha_m} (\alpha_k - a_k) \quad (2.11)$$

In matrix form this equation becomes

$$\mathbf{WJY} = \mathbf{WJE} + \mathbf{WCD} \quad (2.12)$$

where

$$\mathbf{Y} = \begin{bmatrix} y_1 \\ \vdots \\ y_N \end{bmatrix} \quad (2.13)$$

is a vector containing the values of the observations,

$$\mathbf{w} = \begin{bmatrix} w_1 & & 0 \\ & \ddots & \\ 0 & & w_N \end{bmatrix} \quad (2.14)$$

is a diagonal matrix of weighting factors for each data point,

$$\mathbf{J} = \begin{bmatrix} \frac{\partial f(\mathbf{x}_1, \mathbf{a})}{\partial a_1} & \dots & \frac{\partial f(\mathbf{x}_1, \mathbf{a})}{\partial a_M} \\ \vdots & \ddots & \vdots \\ \frac{\partial f(\mathbf{x}_N, \mathbf{a})}{\partial a_1} & \dots & \frac{\partial f(\mathbf{x}_N, \mathbf{a})}{\partial a_M} \end{bmatrix} \quad (2.15)$$

is an  $N \times M$  Jacobian matrix relating the modeled values to the model parameters,

$$\mathbf{E} = \begin{bmatrix} f(x_i, \alpha) \\ \vdots \\ f(x_N, \alpha) \end{bmatrix} \quad (2.16)$$

is vector containing the values of the model using the best estimates for the model parameters,

$$\mathbf{C} = \begin{bmatrix} \frac{\partial^2 f}{\partial \alpha_1^2} & \cdots & \frac{\partial^2 f}{\partial \alpha_1 \partial \alpha_M} \\ \vdots & \ddots & \vdots \\ \frac{\partial^2 f}{\partial \alpha_M \partial \alpha_1} & \cdots & \frac{\partial^2 f}{\partial \alpha_M^2} \end{bmatrix} \quad (2.17)$$

is the curvature (Hessian) matrix, for the objective function and

$$\mathbf{D} = \begin{bmatrix} (\alpha_1 - a_1) \\ \vdots \\ (\alpha_M - a_M) \end{bmatrix} \quad (2.18)$$

is a vector containing uncertainties in the best estimates of the model parameters. Once the optimum values of the model parameters have been calculated, equation (2.12) can be used to relate the uncertainties in the in the model parameters ( $\mathbf{u}_\alpha = (\alpha - \mathbf{a}) = \mathbf{D}$ ) to the uncertainties in the measurement parameters and the uncertainties in the observations.  $\mathbf{Y}$  and  $\mathbf{W}$  come from the measurement. Equation (2.10) can be used to estimate the values of the model parameters ( $\mathbf{E}$ ). However, the elements of  $\mathbf{J}$  and of  $\mathbf{C}$  must be determined from knowledge of the behavior of the model around the optimum values. The goal in Chapter 4 is to find a computationally efficient method for determining the elements of  $\mathbf{J}$  and  $\mathbf{C}$  that are related to edge roughness.

### 2.3. Edge Roughness

As critical dimensions (CD) decrease, line edge roughness (LER) and line width roughness (LWR), are becoming increasingly significant in determining device parameters<sup>57,58,128</sup>. Edge roughness and disorder can also significantly affect the band structure of photonic crystals<sup>52-55,129,130</sup>. While some authors have suggested techniques for designing photonic crystal structures that are less sensitive to these effects<sup>131</sup>, edge roughness remains a primary concern in realizing the potential of photonic crystal devices<sup>53,132</sup>.

There are a variety of descriptors that can be used to characterize LER/LWR<sup>133</sup>, including correlation length ( $\xi$ ), the autocorrelation function (ACF), the height-height correlation function (G), the power spectral density (PSD), and various fractal descriptors such as the roughness exponent ( $\alpha$ )<sup>134</sup>. One of the simplest and most common descriptors for line edge roughness is the root mean square (rms) deviation ( $\sigma$ ) from the average line position ( $\langle x \rangle$ ).

$$\sigma = \sqrt{\frac{1}{N} \sum_{i=1}^N (x_i - \langle x \rangle)^2} \quad (2.19)$$

where the location of the  $i^{\text{th}}$  point along the edge is given by coordinates  $\{x_i, y_i\}$  and N is the number of points in the sample<sup>135</sup>.

Another useful descriptor is the correlation length ( $\xi$ ). The correlation length is defined as the distance over which the auto-correlation function (ACF) is greater than or equal to  $1/e$ . For a discrete set of data, the autocorrelation function can be estimated using:

$$ACF(\Delta y) = \frac{1}{(N - m)\sigma^2} \sum_{i=1}^{N-m} (x_{i+m} - \langle x \rangle)(x_i - \langle x \rangle) \quad (2.20)$$

While complex, model based descriptions of edge roughness have been developed<sup>136</sup>, self-affine structures have been used to describe rough surfaces<sup>137</sup> and some authors have suggested that they also provide adequate descriptors for LER/LWR profiles<sup>133</sup>. A self-affine function has an autocorrelation function ( $ACF$ ) of the form:

$$ACF(\Delta y) = e^{-\left(\frac{\Delta y}{\xi}\right)^{2\alpha}} \quad (2.21)$$

where  $\rho$  is the distance between two points along the nominal edge,  $\xi$  is the linear correlation length of the rough edge, and  $\alpha$  is called the roughness exponent. The roughness exponent, also referred to as the Hurst exponent, is related to the fractal dimension of the edge and it can be used to describe the relative amount of high frequency content in the power spectrum (Figure 6)<sup>137</sup>. Profiles with a Gaussian autocorrelation functions have roughness exponent of one while profiles with exponential autocorrelation functions have relatively more high frequency content and a roughness exponent of one-half.

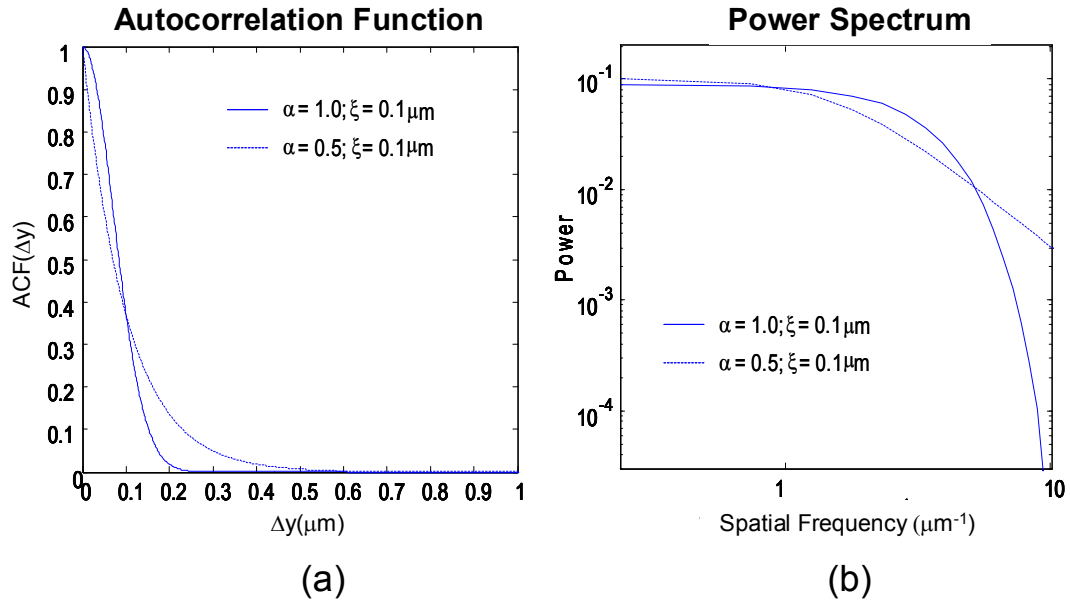


Figure 6 (a) The autocorrelation functions, and (b) the power spectral density of self-affine roughness profiles with exponential ( $\alpha = 0.5$ ) (dashed line) and Gaussian ( $\alpha = 1.0$ ) (solid line) autocorrelation functions. The power spectrum shows the relative increase in high spatial frequency content for the profile with the exponential autocorrelation function.

Figure 7 shows four examples of line edge profiles with different correlation lengths and roughness exponents. Various process steps used to lithographically fabricate gratings are thought to create edge profiles with different correlation length and roughness exponents, and some processes, such as reactive ion etching may introduce some directionality to the roughness<sup>138</sup>.

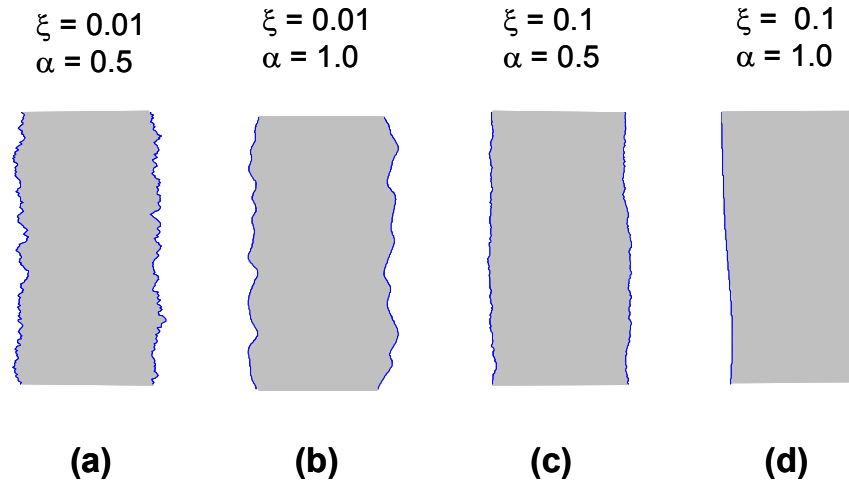


Figure 7 Examples of the two-dimensional grating profiles created to have various correlation lengths ( $\xi$ ) and roughness exponents ( $\alpha$ )

As with surface roughness measurements<sup>139</sup>, roughness measurements are sensitive to the scan length (area) of the measurement and the correlation length (function) of the roughness. The Metrology section of the 2007 International Technology Roadmap for Semiconductors<sup>118</sup> recommends that the “LER/LWR metric is thus defined as the  $3\sigma$  of the residuals measures along a 2  $\mu\text{m}$  line for the present; however, transistor performance could be more sensitive against in-gate roughness in the future” This dependence is of particular concern for comparing scatterometry measurements with other techniques since the scatterometry measurements inherently average values over the entire measurement area. However, Constantoudis et. al. have concluded through extensive numerical simulations that the calculated value of the rms deviation tends to asymptotically approach a fixed value as the edge length approaches ten times the correlation length of the roughness<sup>133</sup>.

There is currently no similar agreed upon metric for quantifying the deviation of the edge of a lithographically produced hole. However, Lee et. al.<sup>140</sup> have proposed a definition of contact edge roughness (CER)

$$CER = 3\sqrt{\frac{\sum_{i=1}^n [r(\theta_i) - r]^2}{n}} \quad (2.22)$$

where  $r(\theta_i)$  is the radius of the circle at angle  $\theta_i$ ,  $r$  is one-half of the CD (the mean radius of the circle), and  $n$  is the number of samples.

Many factors throughout the fabrication process may contribute to edge roughness. For conventional photolithographic based processes, diffusion of the photo-active generator (PAG) during the post-bake process has been studied extensively<sup>141, 142</sup>. The dry etch process can also contribute to LER<sup>138</sup>. Interference lithography techniques are particularly susceptible LER<sup>143</sup>. The actual nature of LER/LWR is a topic that is under active investigation<sup>144</sup>. Some processes may produce an isotropic roughness while others, such as plasma assisted etch processes, may introduce directionality to the roughness<sup>145</sup>. Work in this dissertation only examines the effect of an anisotropically rough edges on the scattering from sub-wavelength gratings. Calculating the reflectance from the three-dimensionally periodic gratings that are needed to simulate isotropic edge roughness would not have been practical and insight into the limits of the approximation methods can be gained using the two-dimensional LER models.

At one level, it is straightforward to determine roughness statistics from direct analysis of profile data obtained by SEM and AFM<sup>140,146-154</sup>. However, for top-down SEM measurements, the image quality can have a significant effect on the measured edge roughness. For example, Nelson et. al. were able to obtain estimates of rms edge

roughness of 3 nm ( $1\sigma$ ) for an poorly stigmatized image and an estimate of 23 nm ( $1\sigma$ ) for an image with correct stigmatism<sup>150</sup>. AFM measurements are extremely time consuming and often require special instruments and tooling<sup>154</sup>.

Petit and Boher have used Fourier transform scatterometry to look at out of plane scattering from edge roughness<sup>155</sup>. Similar techniques for measuring edge roughness using Coblentz spheres have been proposed by Bischoff et. al.<sup>156</sup>. Germer has computationally examined the effect of edge roughness on optical scatterometry signals using a mean field approximation based on Monte Carlo simulations using one dimensional rigorous coupled wave analysis<sup>157</sup>. All of these studies have used techniques that are limited to measuring roughness with correlation lengths that are greater than the wavelength of the probe light. Since x-rays have a much smaller wavelength, CD-SAXS has been examined as a method for measuring smaller correlation length roughness using higher order diffraction peaks<sup>96,158,159</sup>. Even more exotic metrology techniques such as small angle neutron scattering have been proposed<sup>160</sup>.

Edge roughness is potentially a significant source of uncertainty in optical scatterometry measurements<sup>161,162</sup>. Brill has proposed a variety of methods that might be considered for measuring edge roughness using optical scatterometry<sup>163</sup>. However, further investigation is needed to incorporate the methods and develop models for edge roughness that can be incorporated into practical scatterometry systems.

For this study, initial investigations into the effect of edge roughness on optical scatterometry signals involved fabricating a set of artifacts with intentional edge roughness. The artifacts were created in silicon with e-beam lithography, using a Raith 150 e-beam lithography system<sup>70</sup>, and etched into the silicon using reactive ion etching

with a STS Silicon Fast Etcher<sup>164</sup>. A detailed description of the artifacts is included in Appendix C. However, as detailed in Appendix D, measurements on these artifacts proved to be problematic and few conclusions can be made from the experimental data. These issues demonstrate the need for appropriate theoretical models of effects of line edge roughness on optical scatterometry signals.

However, modeling optical scatterometry signals from gratings with edge roughness can quickly become very computationally expensive. The remaining chapters examine how approximation methods might be applied to simplify these models and decrease computation expense of modeling edge roughness. These approximation methods could make it practical to include edge roughness as a parameter in optical scatterometry models. Once edge roughness is incorporated into the models the contribution of edge roughness to the uncertainty in other parameters can be evaluated as outlined in section 2.2.

## CHAPTER 3: THEORY

Optical scatterometry measurements rely on fitting some theoretical model to the measured data. Rigorous coupled wave analysis (RCWA) has emerged as the predominant model used for optical scatterometry measurements on periodic structures. The effect of LER/LWR on optical scatterometry signals can be simulated using a rigorous coupled wave analysis for a biperiodic structure (2D RCWA). However, the computational expense needed to model edge roughness in this way can be prohibitive. For example, if one retains  $\pm 10$  orders in each of the two dimensions of the field expansions, the calculation is theoretically about 9000 times more computationally expensive than if one retained  $\pm 10$  orders for one-dimensionally periodic structures (1D RCWA). In practice, to calculate a set of forty-seven reflectivities (one for each of forty-seven different incident angles) requires approximately one hour and forty minutes on Intel Xeon 2.40GHz dual core processor using the 2D RCWA while the calculation using the 1D RCWA took only 7.2 seconds on the same system. An approximation that enables an estimate of the effects of LER, without requiring a full 2D RCWA simulation, would allow such effects to be accounted for in scatterometry measurements. In this chapter, a plane wave expansion (PWE) method is derived which leads into a description of the RCWA algorithm. Two approximation methods are also examined, the *volume current perturbation theory* and the *generalized anisotropic Bruggeman effective medium approximation (ABEMA)*. The volume current perturbation method has been used

previously to predict band edge shifts in photonic crystals caused by edge roughness<sup>130,165</sup>. The generalized anisotropic Bruggeman effective medium theory has been used to model anisotropic thin film structures<sup>166</sup>. In Chapter 4, the generalized anisotropic Bruggeman effective medium theory is used to model the effects of edge roughness on optical scatterometry signals.

### 3.1. Rigorous Electromagnetic Modeling Techniques

Methods for rigorously solving Maxwell's equations in optical system can, in general, be divided into two categories<sup>167,168</sup>. One set of methods uses Maxwell's equations to calculate the fields at discrete points in the spatial domain, while the other set in some way calculates the properties of the fields in the spatial frequency domain.

In the former, the field is propagated through the system by solving Maxwell's equations at each point, given the solutions at nearby points. These methods include finite element methods (FEM) and the Finite Difference Time Domain (FDTD) and Finite Difference Frequency Domain (FDFD) methods<sup>169, 170</sup>. They are straightforward and have found wide application in software for designing photonic crystal devices and other complex optical structures. However, the computational expense of these models tends to scale inversely with the grid spacing needed to approximate the profile.

The second category of methods involves calculating the spatial frequencies of the electromagnetic fields. The details of the computation vary among the different techniques, however, in general they all in some way:

1. Form an expression for the electric or magnetic field in each region of interest.
2. Apply the electromagnetic boundary conditions across regions.

### 3. Solve the resulting set of linear equations.

This category includes a number of related methods, including modal methods (MM)<sup>171-174</sup>, the transfer matrix (T-Matrix) method<sup>175</sup>, the scattering matrix (S-Matrix) method<sup>176-180</sup>, rigorous coupled wave analysis (RCWA)<sup>181-185</sup>, and the plane wave expansion (PWE) method<sup>168,186,187</sup>.

#### 3.1.1. Plane Wave Expansion (PWE) Method

The plane wave expansion (PWE) method is a computational method for determining the band structure of a material with a periodically perturbed permittivity profile by solving for the eigen-modes of the system at various spatial frequencies (k-vectors).

The relationships between the electric and magnetic fields are rigorously described by Maxwell's equations<sup>188</sup>. In cgs (centimeter, gram, second) units

$$\nabla \cdot \mathbf{D} = 4\pi\rho \quad (3.1)$$

$$\nabla \times \mathbf{H} = \frac{1}{c} \frac{\partial \mathbf{D}}{\partial t} + \frac{4\pi}{c} \mathbf{J} \quad (3.2)$$

$$\nabla \times \mathbf{E} = -\frac{1}{c} \frac{\partial \mathbf{B}}{\partial t} \quad (3.3)$$

$$\nabla \cdot \mathbf{B} = 0 \quad (3.4)$$

where  $\mathbf{D}$  is the electric displacement field,  $\rho$  is the free electric charge density,  $\mathbf{H}$  is the magnetic field,  $c$  is the speed of light in vacuum,  $\mathbf{J}$  is the free current density,  $\mathbf{E}$  is the electric field, and  $\mathbf{B}$  is the magnetic induction. The constitutive equations relate the electric field to the electric displacement and the magnetic field to the magnetic induction in a linear, isotropic material through

$$\mathbf{D} = \epsilon \mathbf{E} \quad (3.5)$$

and

$$\mathbf{B} = \mu\mathbf{H} \quad (3.6)$$

where  $\varepsilon = (1 + \chi_e)\varepsilon_0$  is the electric permittivity of the medium, given its electric susceptibility ( $\chi_e$ ) and the permittivity of free space ( $\varepsilon_0$ ), and  $\mu = (1 + \chi_m)\mu_0$  is the magnetic permeability of the medium, given the magnetic susceptibility ( $\chi_m$ ) and the permeability of free space ( $\mu_0$ ). Most problems related to optics involve materials that can be considered non-magnetic. Therefore, for optical systems  $\mu = 1$  (in cgs units) so that  $\mathbf{B} = \mathbf{H}$ .

The Bloch (Floquet) theorem states that<sup>33</sup>

*The eigenfunctions of the wave equation for a periodic potential are the product of a plane wave  $e^{i\mathbf{k}\cdot\mathbf{r}}$  times a function  $u_k(\mathbf{r})$  with the periodicity of the crystal lattice.*

$$\Psi_k(\mathbf{r}) = u_k(\mathbf{r})e^{i\mathbf{k}\cdot\mathbf{r}} \quad (3.7)$$

This implies that, given a periodic dielectric permittivity function ( $\varepsilon$ ), the electric and magnetic fields may be decomposed into a set of plane-wave solutions<sup>186</sup>. For time periodic fields, each of these solutions may be expressed as

$$\mathbf{E} = \mathbf{E}_0 e^{-i\omega t} \quad (3.8)$$

$$\mathbf{H} = \mathbf{H}_0 e^{-i\omega t} \quad (3.9)$$

with time derivatives

$$\frac{d\mathbf{E}}{dt} = -i\omega\mathbf{E}_0 e^{-i\omega t} = -i\omega\mathbf{E} \quad (3.10)$$

$$\frac{d\mathbf{H}}{dt} = -i\omega\mathbf{H}_0 e^{-i\omega t} = -i\omega\mathbf{H} \quad (3.11)$$

Substituting equation (3.11) into equation (3.2) and equation (3.3), using equation (3.5) and equation (3.6) to eliminate  $\mathbf{B}$  and  $\mathbf{D}$ , and assuming for the moment that  $\mathbf{J} = 0$  (and  $\mu = 1$ )

$$\nabla \times \mathbf{H} = \varepsilon \frac{1}{c} \frac{\partial \mathbf{E}}{\partial t} = -\varepsilon \frac{\omega}{c} i \mathbf{E} \quad (3.12)$$

and

$$\nabla \times \mathbf{E} = -\frac{1}{c} \frac{\partial \mathbf{H}}{\partial t} = \frac{\omega}{c} i \mathbf{H} \quad (3.13)$$

Solving equation (3.13) for  $\mathbf{H}$  and substituting into equation (3.12) results in a linear operator eigenvalue problem

$$\frac{1}{\varepsilon} \nabla \times \nabla \times \mathbf{E} = \left( \frac{\omega}{c} \right)^2 \mathbf{E} \quad (3.14)$$

with a linear eigen-operator  $\frac{1}{\varepsilon} \nabla \times \nabla \times$  and eigenvalues  $(\omega/c)^2$ . Solving equation (3.12) for  $\mathbf{E}$  and substituting into equation (3.13) results in a similar eigenvalue equation in  $\mathbf{H}$

$$\nabla \times \frac{1}{\varepsilon} \nabla \times \mathbf{H} = \left( \frac{\omega}{c} \right)^2 \mathbf{H} \quad (3.15)$$

For lossless systems,  $\varepsilon$  is real and equations (3.14) and (3.15) are Hermetian eigen-problems that have real eigenvalues and a complete, orthogonal sets of eigen-states<sup>189</sup>.

Since in deriving equation (3.14) and equation (3.15) the permittivity profile ( $\varepsilon$ ) was assumed to be periodic, it can be expanded in terms of some complete periodic basis set, such as a Fourier series, such that

$$\varepsilon(\mathbf{r}) = \sum_{\mathbf{G}\lambda} \varepsilon(\mathbf{G}) e^{i(\mathbf{G}\cdot\mathbf{r})} \quad (3.16)$$

where  $\mathbf{r}$  is a vector representing the spatial position and  $\mathbf{G}$  is the corresponding vector in reciprocal space.

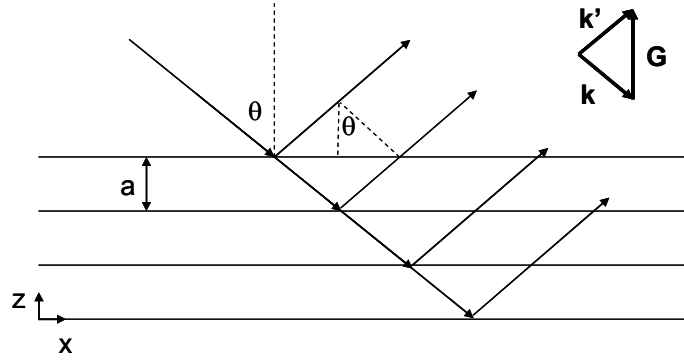


Figure 8. Definition of variables used to describe a Bloch wave.

Referring to Figure 8, the reflected  $\mathbf{k}$ -vector ( $\mathbf{k}'$ ) can be related to the incident wave-vector ( $\mathbf{k}$ ) through

$$\mathbf{k}' = (\mathbf{k} + \mathbf{G}) \quad (3.17)$$

Using equation (3.7), the electric and magnetic fields can be expressed as

$$E_{\omega}^k(\mathbf{r}) = \sum_{G\lambda} e_{G\lambda} \mathbf{e}_{\lambda} e^{i[(\mathbf{k}+\mathbf{G})\cdot\mathbf{r}]} \quad (3.18)$$

and

$$H_{\omega}^k(\mathbf{r}) = \sum_{G\lambda} h_{G\lambda} \mathbf{e}_{\lambda} e^{i[(\mathbf{k}+\mathbf{G})\cdot\mathbf{r}]} \quad (3.19)$$

where  $\mathbf{e}_{\lambda}$  is the unit vector representing the polarization direction and  $e_{G\lambda}$  and  $h_{G\lambda}$  are the Bloch modes of the system. Equations (3.14) and (3.15) can be solved for the characteristic frequencies (eigenvalues) of each of these Bloch modes (eigenvectors). The dispersion diagram (band-diagram) is created by plotting these characteristic frequencies as a function of the incident wave-vectors (Figure 9).

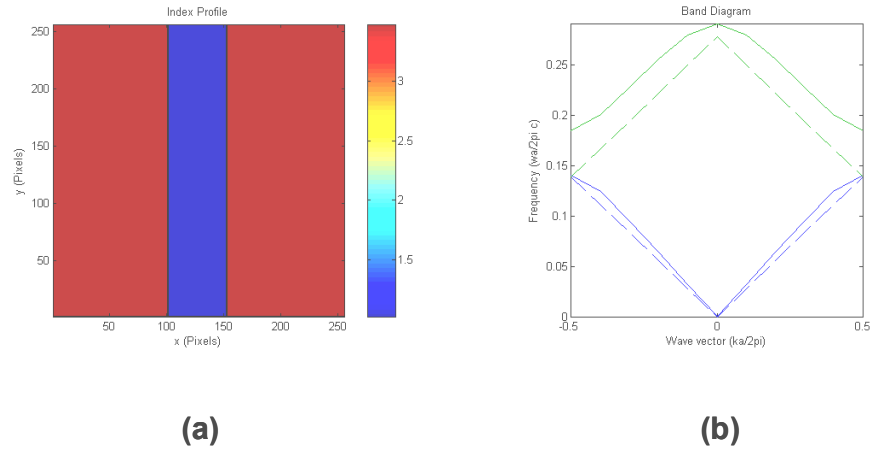


Figure 9. a) The index profile for one period of a simple lamellar grating and b) the dispersion diagram for the grating calculated using the PWE method. The dashed lines are for the homogeneous low index medium and the solid lines are for the periodic structure.

A flowchart of an implementation of the plane wave expansion method is shown shown in Figure 10.

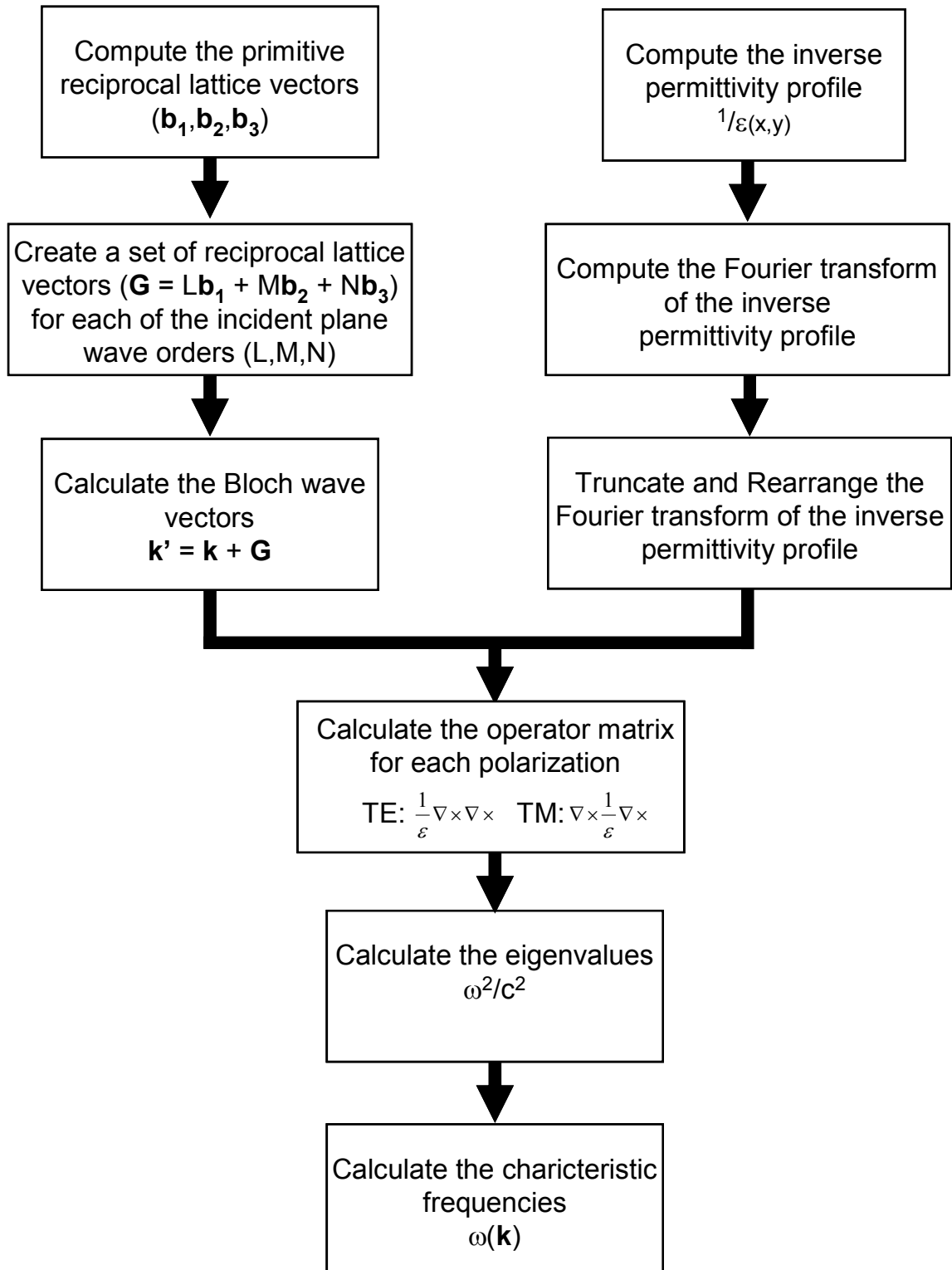


Figure 10. Flowchart describing an algorithm for implementing the plane wave expansion (PWE) method for calculating the dispersion of a periodic medium.

### 3.1.2. Rigorous Coupled Wave Analysis (RCWA)

In homogeneous media, the permittivity values ( $\varepsilon$ ) are constant and equation (3.14) reduces to the Helmholtz equations

$$(\nabla^2 - k^2)\mathbf{E} = 0 \quad (3.20)$$

where  $k = 2\pi n/\lambda_0$ ,  $n$  is the generally complex index of refraction of the medium and  $\lambda_0$  is the free space wavelength of the field. Equation (3.20) has particular solutions of the form

$$\mathbf{E} = A e^{i(k_x x + k_y y + k_z z)} \quad (3.21)$$

where  $[k_x, k_y, k_z]$  are the components of a wave vector perpendicular to a plane wavefront and  $A$  is a proportionality constant determined by the boundary conditions of the problem. The general solution is then

$$\mathbf{E}(x, y, z) = \sum_{m=-\infty}^{\infty} A_m e^{i(k_{x_m} x + k_{y_m} y + k_{z_m} z)} + \sum_{n=-\infty}^{\infty} B_n e^{i(k_{x_n} x + k_{y_n} y - k_{z_n} z)} \quad (3.22)$$

Equation (3.22) is the Rayleigh expansion<sup>190</sup> for the total field within the homogeneous region. It is the sum of forward propagating and evanescent components and backward propagating and evanescent components (Figure 11).

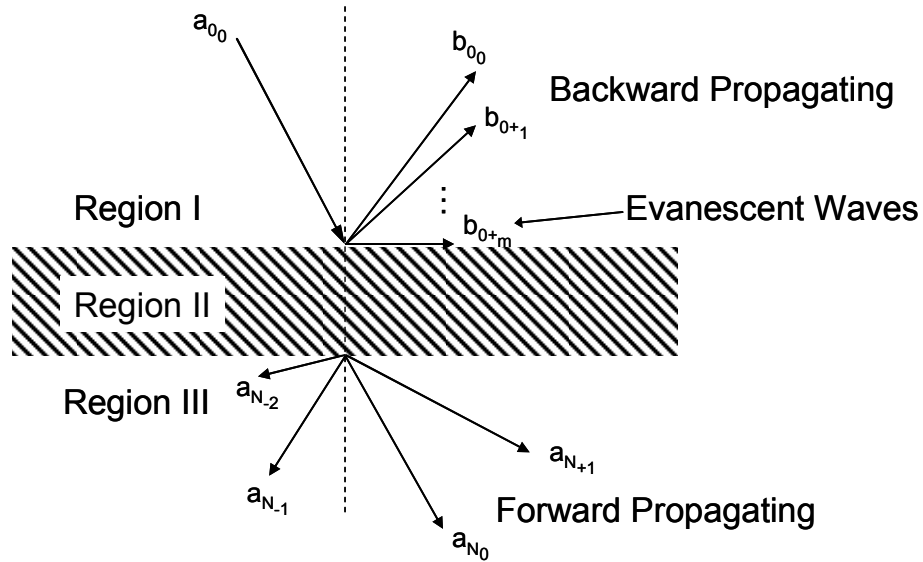


Figure 11. Definition of terms used in the description of RCWA

In an isotropic, homogeneous media, the relationship between the terms in the Rayleigh expansion remains fixed. However, a change in the permittivity will cause a mixing between the components<sup>191</sup>. For example, if a forward propagating plane wave traverses the boundary between a low index medium and a higher index medium, some of the energy in the forward propagating wave will be coupled into a backward propagating (i.e. reflected) wave. For the homogeneous media it is relatively straightforward to calculate the fraction of the ratio of the incident and reflected fields<sup>192</sup>.

The situation is somewhat more complex if one or more of the layers has a periodically perturbed permittivity profile. RCWA is a computational method used to relate the spatial frequencies (Fourier components) of reflected and transmitted fields to the incident field by calculating the coupling strengths between incident and reflected fields in a material with a periodically perturbed permittivity profile and matching the boundary conditions at the interfaces.

As with homogeneous thin films<sup>192</sup>, the incident, and diffracted fields can be related to each other using a transfer matrix (T). However, the transfer matrix must account for all modes that are supported by the periodic structure.

$$\begin{bmatrix} a_0 \\ b_0 \end{bmatrix} = \mathbf{T} \begin{bmatrix} a_N \\ b_N \end{bmatrix} \quad (3.23)$$

where  $a_0$  are the Rayleigh coefficients for the forward propagating (and/or evanescent) incident waves,  $b_0$  are the Rayleigh coefficients for the backward propagating (and/or evanescent) diffracted waves in the incident medium (the “reflected” diffraction orders),  $a_N$  is a vector representing the Rayleigh coefficients for the forward propagating (transmitted) diffraction orders, and  $b_N$  is a vector representing the Rayleigh coefficients for the backward propagating orders in the transmitted medium (this term is usually considered to be zero). Unfortunately, this formulation of the problem is susceptible to numerical instabilities due to exponentially growing terms in the propagation matrices for optically thick gratings<sup>193</sup>. This problem was solved by rearranging the terms in (3.23) so that the incident components of the field ( $a_0$  and  $b_N$ ) are related to the reflected and transmitted components ( $a_N$  and  $b_0$ ) through a scattering matrix (S)

$$\begin{bmatrix} a_0 \\ b_N \end{bmatrix} = \mathbf{S} \begin{bmatrix} a_N \\ b_0 \end{bmatrix} \quad (3.24)$$

In Chapter 4, the specular reflectance functions of a rough periodic grating are calculated using RCW algorithms as described by Moharam *et al.*<sup>183,184</sup> with a modification proposed by Lelanne and Morris<sup>185</sup> and Li<sup>194</sup> and extended to two dimensionally periodic structures by Li<sup>173</sup>. The software that was used for the 1D RCWA simulations is available online<sup>195</sup> while the software used for the 2D RCWA simulations will be made available to the general public in a future release of the software. Examples of the script language used to control the software are included in Appendix E.

### 3.2. Volume Current Perturbation Theory

In deriving the equations for the plane wave expansion method, it was assumed that there were no current sources in the system. A more general solution can be derived if the free current term is considered, so that equation (3.12) becomes

$$\nabla \times \mathbf{H} = \varepsilon \frac{1}{c} \frac{\partial \mathbf{E}}{\partial t} + \frac{4\pi}{c} \mathbf{J} \quad (3.25)$$

Substituting (3.10) into (3.25)

$$\nabla \times \mathbf{H} = \varepsilon \frac{-i\omega}{c} \mathbf{E} + \frac{4\pi}{c} \mathbf{J} \quad (3.26)$$

and, solving for the electric field

$$\mathbf{E} = \frac{c}{-i\varepsilon\omega} \nabla \times \mathbf{H} - \frac{c}{-i\varepsilon\omega} \frac{4\pi}{c} \mathbf{J} \quad (3.27)$$

Using the relationship in equation (3.11) and substituting equation (3.27) into equation (3.13) then gives

$$\nabla \times \left[ \frac{c}{-i\varepsilon\omega} \nabla \times \mathbf{H} + \frac{4\pi}{-i\varepsilon\omega} \mathbf{J} \right] = -\frac{i\omega}{c} \mathbf{H} \quad (3.28)$$

So that, finally

$$\nabla \times \frac{1}{\epsilon} \nabla \times \mathbf{H} - \nabla \times \frac{4\pi}{\epsilon} \mathbf{J} = \left(\frac{\omega}{c}\right)^2 \mathbf{H} \quad (3.29)$$

where  $\mathbf{J}$  is the current density. Perturbation methods can be used to calculate a shift in the characteristic frequencies (eigen-frequencies) of a system due to small changes in the operator<sup>196</sup>. Equation (3.29) is of the form

$$\mathbf{A}\mathbf{x} + \mathbf{b} = \lambda\mathbf{x} \quad (3.30)$$

Therefore, a perturbation ( $b$ ) on the original eigenvalue problem ( $\mathbf{A}\mathbf{x} = \lambda\mathbf{x}$ ) can be thought of as the addition of a field due to a current  $\mathbf{J}$ . For a shifting dielectric boundary,  $\mathbf{J}$  is proportional to  $\Delta\epsilon\mathbf{E}$ , where  $\mathbf{E}$  is the electric field in the unperturbed system and  $\Delta\epsilon$  is a small change in the permittivity<sup>130</sup>.

If the eigenvalue equation for the unperturbed system is represented by  $\mathbf{A}x = \lambda x$  where  $\lambda$  are the eigenvalues and  $x$  are the associated eigenvectors of the unperturbed system, then the perturbed system can be represented by<sup>196</sup>

$$\mathbf{A}y + d\alpha \cdot b = zy \quad (3.31)$$

where  $y$  are the eigenvectors and  $z$  are the eigenvalues of the perturbed system and  $d\alpha$  is a parameter equal to some small perturbation factor. If the perturbation is small then the change in the eigenvalues and associated eigenvectors are also expected to be small.

Expanding the  $y$  and  $z$  terms in equation (3.31) in powers of  $d\alpha$

$$y = x^{(0)} + d\alpha x^{(1)} + d\alpha^2 x^{(2)} \dots \quad (3.32)$$

and

$$z = \lambda^{(0)} + d\alpha\lambda^{(1)} + d\alpha^2\lambda^{(2)} \dots \quad (3.33)$$

where  $\lambda^{(n)}$  and  $x^{(n)}$  are the n-th order perturbation terms for the eigenvalues and associated eigenvectors. Note that  $\lambda^{(0)}$  and  $x^{(0)}$  are simply the eigenvalues and eigenvectors for the unperturbed system. Substituting equations (3.32) and (3.33) into equation(3.31), neglecting higher order terms in  $d\alpha$ , and equating like powers of  $d\alpha$ ,

$$\mathbf{A}x^{(0)} = \lambda^{(0)}x^{(0)} \quad (3.34)$$

$$\mathbf{A}x^{(1)} + b = \lambda^{(0)}x^{(1)} + \lambda^{(1)}x^{(0)} \quad (3.35)$$

Note that equation (3.34) is simply the equation for the unperturbed system. Rearranging the terms in equation (3.35) gives

$$\left( \mathbf{A} - \lambda^{(0)} \right) x^{(1)} = \lambda^{(1)}x^{(0)} - b \quad (3.36)$$

Since  $\mathbf{A}$  is Hermitian,  $x^{(0)\dagger} \mathbf{A} x^{(0)} = \lambda^{(0)}$  where  $x^{(0)\dagger}$  is the complex conjugate transpose of  $x^{(0)}$ . Therefore,  $x^{(0)\dagger} (\mathbf{A} - \lambda^{(0)}) = 0$ . By multiplying equation (3.36) by  $x^{(0)\dagger}$  the left hand side can be eliminated. Then, solving for the first order perturbation of the eigenvalue

$$\lambda^{(1)} = \frac{x^{(0)\dagger} b}{x^{(0)\dagger} x^{(0)}} \quad (3.37)$$

Applying equation (3.37) to equation (3.33), comparing with equation (3.29), and dividing both sides by  $d\alpha$ , we obtain

$$\frac{d\omega}{d\alpha} = -\frac{\omega^{(0)} \mathbf{E}^{(0)\dagger} \frac{d\varepsilon}{d\alpha} \mathbf{E}^{(0)}}{2 \mathbf{E}^{(0)\dagger} \varepsilon \mathbf{E}^{(0)}} \quad (3.38)$$

where  $d\omega/d\alpha$  is the sensitivity of the system to the perturbation factor at a particular eigen-frequency ( $\omega^{(0)}$ ) with an associated eigenvector  $\mathbf{E}^{(0)}$ ,  $d\varepsilon/d\alpha$  is the rate of shift in the permittivity profile with  $\alpha$ , and  $\varepsilon$  is the permittivity profile of the unperturbed system. The system is most sensitive to  $d\alpha$  when  $d\alpha/d\omega$  is large. The denominator in equation (3.38) can be viewed as the total energy in the unperturbed mode, while the numerator is the rate of change in the energy in the mode with respect to the perturbation. Ideally, the system would be operated where it is least sensitive to the perturbation, but measured where it is most sensitive.

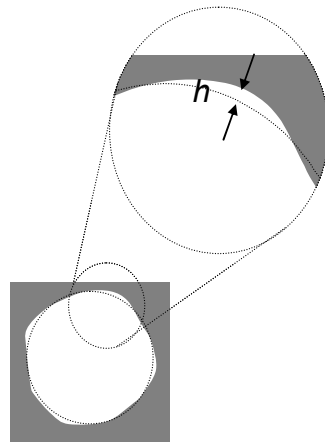


Figure 12. Illustration of a perturbation to the system by shifting the dielectric boundary

Johnson et. al.<sup>197</sup> have derived an expression for the change in the energy of the modes in terms of a shift in the dielectric boundary ( $dh/d\alpha$ ) (Figure 12).

$$E^{(0)\dagger} \frac{d\varepsilon}{d\alpha} \mathbf{E}^{(0)} = \int \left( \frac{dh}{d\alpha} \right) \left[ \Delta\varepsilon_{12} \left| \mathbf{E}_{\parallel}^{(0)} \right|^2 - \Delta(\varepsilon_{12}^{-1}) \left| \mathbf{D}_{\perp}^{(0)} \right|^2 \right] dA \quad (3.39)$$

where  $\Delta\varepsilon_{12}$  and  $\Delta(\varepsilon_{12}^{-1})$  are the differences in the permittivity and in the inverse permittivity  $E_{\parallel}^{(0)}$  is the component of the unperturbed electric field that is parallel to the boundary, and  $D_{\perp}^{(0)}$  is the component of the electric displacement perpendicular to the boundary. Since the normal component of the electric field is discontinuous at the boundary, care must be taken in calculating  $D_{\perp}^{(0)}$ <sup>198</sup>. This problem can be solved by calculating  $D_{\perp}^{(0)}$  from  $E_{\perp}^{(0)}$  using

$$\mathbf{D}_{\perp}^{(0)} = \tilde{\boldsymbol{\varepsilon}} \mathbf{E}_{\perp}^{(0)} \quad (3.40)$$

where

$$\tilde{\boldsymbol{\varepsilon}}^{-1} = \int g_s(x - x') \boldsymbol{\varepsilon}^{-1}(x') dx' \quad (3.41)$$

Equation (3.41) is the convolution of the inverse of the permittivity profile with some smoothing function. A cosine squared function, truncated at  $\pm\pi$  radians, satisfies the requirements for the smoothing function specified by Johnson et al.<sup>197</sup> and has a slope that approaches zero at the edge of the filter. A flowchart for one possible implementation the volume current perturbation method using the plane wave expansion method is shown in Figure 13.

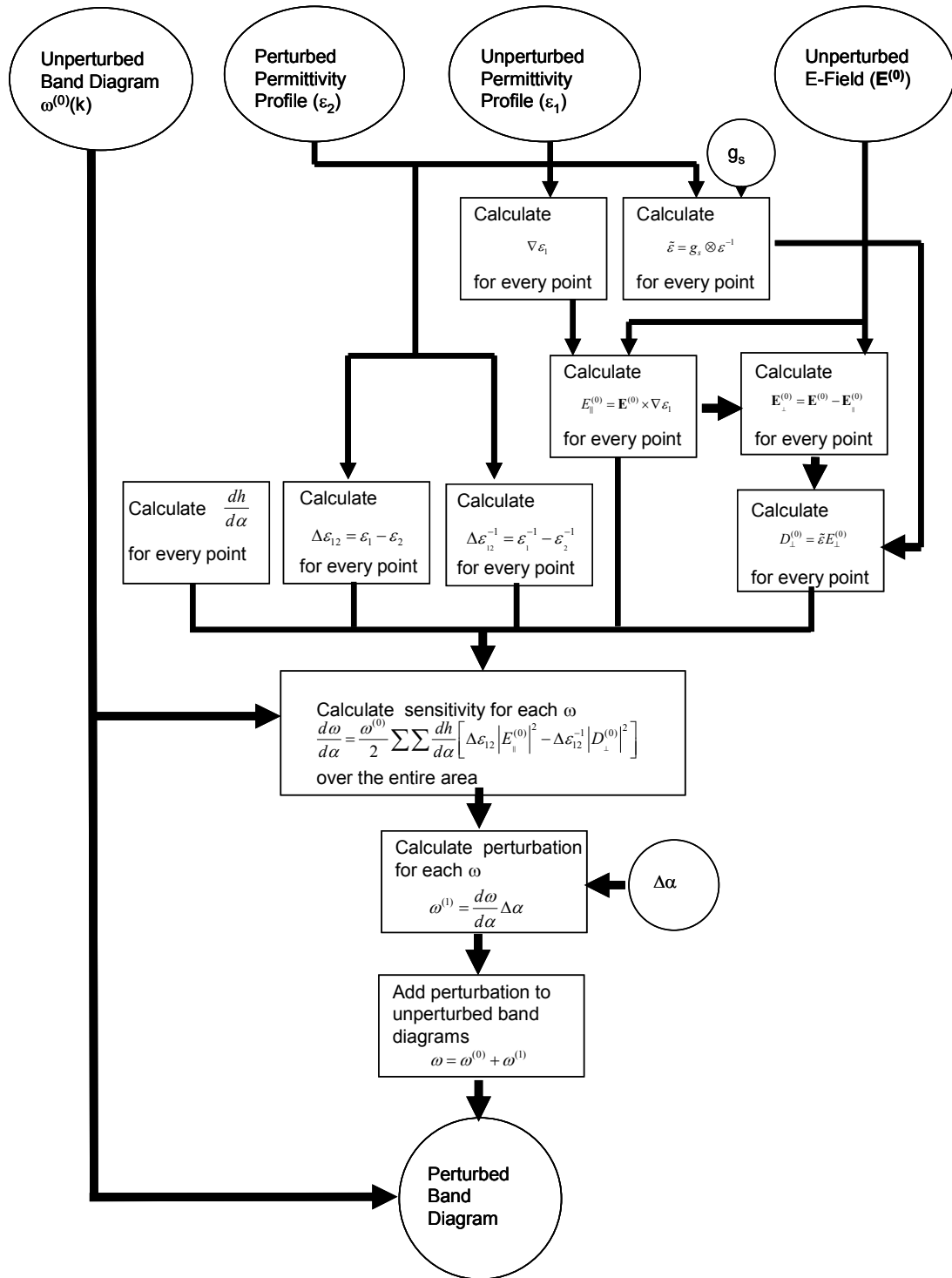


Figure 13. Flow chart of the algorithm used to calculate the perturbation in the band diagram due to shifts in the dielectric boundaries.

There is significant initial computational overhead associated with the perturbation method due to the need to calculate the electric field and the electric displacement for each of the plane wave components in the unperturbed system. However, once the fields for the unperturbed system have been calculated, new perturbations can be quickly assessed by simple addition, subtraction, and scalar multiplication operations. Care must also be taken because the results are only valid for small perturbations from the nominal structure. The validity of the method should be confirmed on a case by case basis by comparing representative perturbations with other methods. The validity may be extended by including higher order terms in equation (3.32) and equation(3.33).

Since the eigenvalue problem for the RCWA algorithm is similar to the eigenvalue problem for the PWE method, a similar approximation technique might be possible for calculating new solutions for slightly different RCWA problems. For example, the reflectance for a slightly rough grating might be calculated from the solutions for the nominal grating without solving the 2D RCWA problem. However, more work is needed to develop an appropriate volume current perturbation method for RCWA algorithms.

### 3.3. Effective Medium Approximations

Effective medium approximations have already been mentioned in section 1.1 in relationship to subwavelength diffractive optical elements. In much of the literature on sub-wavelength diffractive optical elements<sup>17</sup> equations (1.1) and (1.2) are correctly referred to as effective medium approximations (EMA). However, in this dissertation these equations will be referred to as the form birefringence effective medium approximation (FBEMA) to distinguish them from the effective medium approximations derived directly from the classic formalism attributed to Maxwell Garnett<sup>199, 200</sup>. In

section 3.3.3 the FBEMA equations are shown to be a special case of the generalized anisotropic Bruggman effective medium approximation (ABEMA). The ABEMA is used to model the effect of edge roughness on optical scatterometry signals in Chapter 4.

### 3.3.1. Form Birefringence Approximations

An anisotropic effective medium approximation for modeling sub-wavelength lamellar gratings can be derived by considering the continuity of the electric field within “a regular assembly of parallel plates” as described in Born and Wolf<sup>19</sup>(Figure 14). If the distance between the plates (i.e. period of the grating) is much less than the wavelength of the incident light, and the lateral extent of the plates (depth of the grating) is large compared to the wavelength, then the field within the grating region can be considered to be uniform. The electric displacement normal to the interface between the high and low index region within the grating ( $D_{\perp}$ ) must then be continuous so that

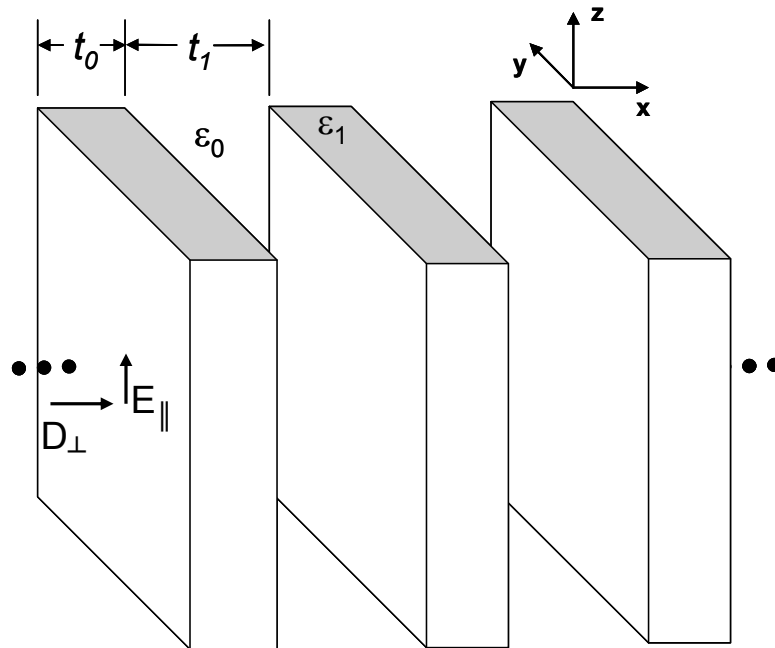


Figure 14. Definition of variables used in the calculation of the form birefringence of a "regular assembly of parallel plates" as described by Born and Wolf<sup>19</sup>.

$$D_{\perp} = \varepsilon_1 E_{1\perp} = \varepsilon_0 E_{0\perp} \quad (3.42)$$

where  $\varepsilon_1$  and  $\varepsilon_0$  are the permittivities of the high index and low index regions of the grating, respectively, and  $E_{1\perp}$  and  $E_{0\perp}$  are the components of the electric field perpendicular to the interface within each material. Therefore, the mean electric field perpendicular to the interface ( $\langle E_{\perp} \rangle$ ) is

$$\langle E_{\perp} \rangle = \frac{t_0 E_{0\perp} + t_1 E_{1\perp}}{t_0 + t_1} = \frac{t_0 \frac{D_{\perp}}{\varepsilon_0} + t_1 \frac{D_{\perp}}{\varepsilon_1}}{t_0 + t_1} = \frac{D_{\perp}}{\varepsilon_{\perp}} \quad (3.43)$$

where  $t_0$  is the thickness of the high index region and  $t_1$  is the thickness of the low index region. The effective inverse permittivity for the field perpendicular to the grating profile is

$$\left( \frac{1}{\varepsilon_{\perp}} \right) = \langle E_{\perp} \rangle / D_{\perp} = \frac{t_0}{t_0 + t_1} \left( \frac{1}{\varepsilon_0} \right) + \frac{t_1}{t_0 + t_1} \left( \frac{1}{\varepsilon_1} \right) = (1 - f) \left( \frac{1}{\varepsilon_0} \right) + f \left( \frac{1}{\varepsilon_1} \right) \quad (3.44)$$

where  $f = t_1 / (t_0 + t_1)$  is the fraction of grating period occupied by the high index material.

Equation (3.44) is just the harmonic average of the high index and low index regions.

Similarly, if we consider the component of the electric field that is tangential to the interface ( $E_{\parallel}$ ), then

$$E_{\parallel} = \frac{D_{1\parallel}}{\varepsilon_1} = \frac{D_{0\parallel}}{\varepsilon_0} \quad (3.45)$$

so that the mean electric displacement parallel to the interface ( $\langle D_{\parallel} \rangle$ ) is

$$\langle D_{\parallel} \rangle = \frac{t_0 \varepsilon_0 E_{\parallel} + t_1 \varepsilon_1 E_{\parallel}}{t_0 + t_1} = \varepsilon_{\parallel} E_{\parallel} \quad (3.46)$$

and the effective permittivity for the field parallel to the interface is simply the geometric average of the high index and low index regions

$$\varepsilon_{\parallel} = (1 - f) \varepsilon_0 + f \varepsilon_1 \quad (3.47)$$

These results are equivalent to the results obtained by Yariv and Yeh<sup>201</sup> by neglecting higher order terms in a series expansion of the dispersion relationship of Bloch waves in periodic media as explained qualitatively in section 1.1 and calculated using the PWE method in section 3.1.1. These results are also equivalent to the results obtained by Southwell<sup>43</sup> in analogy to the dispersion relationship for periodic thin films, and by Rytov<sup>202</sup> in considering an approximation for multiple scattering in stratified media.

### 3.3.2. Maxwell Garnett Effective Medium Approximation

Classical effective medium approximations<sup>199,200,203</sup> are derived based on the assumption that the effective medium can be modeled as inclusions distributed in a homogeneous host medium. If these inclusions are small in comparison with the wavelength of the incident field then the field can be considered to be uniform over the extent of the inclusion. The polarizability ( $\alpha$ ) of a homogeneous, spherical inclusion, with permittivity  $\varepsilon$ , in an otherwise homogeneous dielectric medium, with permittivity  $\varepsilon_h$ , in the presence of a uniform field and in the absence of free charge is<sup>188</sup>

$$\alpha = 3\varepsilon_h V \frac{\varepsilon - \varepsilon_h}{\varepsilon + 2\varepsilon_h} \quad (3.48)$$

where  $V$  is the volume of the spherical inclusion. In the presence of a uniform field ( $\mathbf{E}_0$ ), the spherical inclusion acts as an induced electric dipole with a dipole moment ( $\mathbf{p}$ ) having a magnitude

$$p = -E_0 \frac{(\epsilon_1 - \epsilon_h)}{(\epsilon_1 + 2\epsilon_h)} a^3 \quad (3.49)$$

oriented in a direction as to oppose to the applied field. In the absence of dipole-dipole interactions, Maxwell Garnett showed that the relationship between the effective permittivity of materials made up of sparsely distributed spherical inclusions is of the form<sup>200</sup>

$$\frac{\epsilon_{eff} - \epsilon_h}{\epsilon_{eff} + 2\epsilon_h} = \sum_{i=1}^N f_i \frac{\epsilon_i - \epsilon_h}{\epsilon_i + 2\epsilon_h} \quad (3.50)$$

where  $\epsilon_{eff}$  is the effective permittivity,  $\epsilon_h$  is the permittivity of the host medium,  $\epsilon_i$  is the permittivity of the  $i^{th}$  constituent material, and  $f_i$  is the volume fraction of the  $i^{th}$  constituent material. This equation assumes that the volume fraction of the inclusions are small and gives divergent answers for the effective permittivity in the case of near equal volume fractions when the role of the host and inclusion material are interchanged. Since this formulation does not account for interactions between dipoles (or higher order multipoles), its accuracy is limited to cases where the distribution of the inclusions is sparse. For example, the plot in Figure 15 shows the effective permittivity calculated for a vacuum/silicon mixture as a function for the volume fraction of silicon using either

silicon or vacuum as the host material. It is clear from this graph that the choice of host material makes a difference in the results and that these results differ significantly when the volume fill fractions are nearly equal.

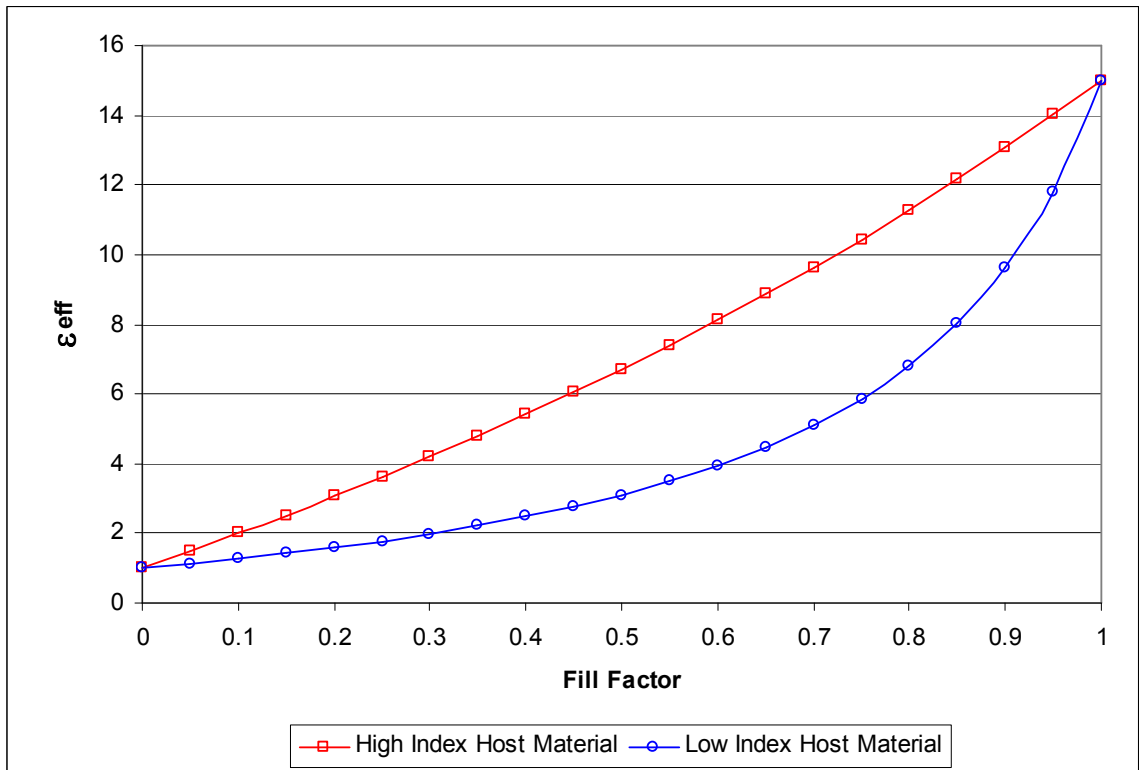


Figure 15. Plot of the effective permittivity calculated for an air/silicon mixture using the Maxwell-Garnett formula with either the high-index material (dashed line) or the low index material (solid line) as the host material, showing the inconsistencies in the calculation.

### 3.3.3. Bruggeman Effective Medium Approximation

Bruggeman corrected this problem by making the assumption that the host medium is the effective medium<sup>203-205</sup>, so that, for a two component mixture, the formula for the effective permittivity becomes

$$f_0 \frac{\varepsilon_0 - \varepsilon_{eff}}{\varepsilon_0 + 2\varepsilon_{eff}} + f_1 \frac{\varepsilon_1 - \varepsilon_{eff}}{\varepsilon_1 + 2\varepsilon_{eff}} = 0 \quad (3.51)$$

This relationship leads to a quadratic equation that can be solved for the effective permittivity.

$$\varepsilon_{eff} = \frac{-b \pm \sqrt{b^2 - 4ac}}{2a}$$

$$a = -2(f_0 + f_1) \quad (3.52)$$

$$b = (2f_0 - f_1)\varepsilon_0 + (2f_1 - f_0)\varepsilon_1$$

$$c = (f_0 + f_1)\varepsilon_0\varepsilon_1$$

It can also be shown that the form birefringence approximations in equations (3.44) and (3.47) are equivalent to the Bruggeman approximation in the case of elliptical inclusions. For the spherical inclusion, the solution to the Laplace equation was aided by the spherical symmetry of the problem. For more arbitrary shapes, a closed-form solution is not generally possible. Sihvola and other have calculated the polarizability of several classes of shapes by solving the integral equation formulation for the static potential using the Method of Moments (MoM)<sup>206,207</sup>. However, for permittivity contrasts of less than an order of magnitude, the permittivity of an arbitrary shape can be closely approximated by that of an ellipsoid with similar aspect ratios<sup>208</sup>. The polarizability for an ellipsoid along the  $i^{\text{th}}$  axis is given by<sup>208-210</sup>

$$\alpha_{N,i} = 3\varepsilon_0 V \frac{\varepsilon_1 - \varepsilon_0}{\varepsilon_1/\varepsilon_0 + L_i(\varepsilon_1 - \varepsilon_0)} \quad (3.53)$$

where  $L_i$ , the depolarization factor along the  $i^{\text{th}}$  axis can be determined by solving

$$L_i = \frac{a_i a_j a_k}{2} \int_0^\infty \frac{1}{(s + a_i^2) \sqrt{(s + a_i^2)(s + a_j^2)(s + a_k^2)}} ds \quad (3.54)$$

where  $a_i, a_j, a_k$  are the lengths of the semi-axes of the ellipsoid.

$$\text{For a sphere:} \quad L_x = L_y = L_z = 1/3$$

$$\text{For a thin disk:} \quad \begin{aligned} L_x &= L_y = 0 \\ L_z &= 1 \end{aligned}$$

$$\text{For a thin needle} \quad \begin{aligned} L_x &= L_y = 1/2 \\ L_z &= 0 \end{aligned}$$

Using equation (3.53), equation (3.50) can be recast in terms of the polarizability of a non-spherical inclusion such that along the  $i^{\text{th}}$  axis

$$f_0 \frac{\varepsilon_0 - \varepsilon_{eff}}{\varepsilon_0/\varepsilon_{eff} + L_i(\varepsilon_0 - \varepsilon_{eff})} + f_1 \frac{\varepsilon_1 - \varepsilon_{eff}}{\varepsilon_1/\varepsilon_{eff} + L_i(\varepsilon_1 - \varepsilon_{eff})} = 0 \quad (3.55)$$

This is consistent with the results obtained by Stroud in relation to the conductivity of non-spherical particles<sup>211</sup> and with the more general solutions in terms of polarization dyadics obtained by Makay<sup>166</sup>.

With some algebra, equation (3.55) can be arranged in terms of  $\varepsilon_{eff}$

$$\begin{aligned} & [(L_i - 1)(f_0 + f_1)] \varepsilon_{eff}^2 + \\ & [f_0 (\varepsilon_0 - L_i \varepsilon_0 - L_i \varepsilon_1) + f_1 (\varepsilon_1 - L_i \varepsilon_0 - L_i \varepsilon_1)] \varepsilon_{eff} + L_i (f_0 + f_1) \varepsilon_0 \varepsilon_1 = 0 \end{aligned} \quad (3.56)$$

In the limit of a thin disk this generalized anisotropic Bruggeman EMA (ABEMA) reduces to the FBEMA. The regular assembly of parallel plates in Figure 14 can be

approximated by an array of thin disks oriented such that  $L_x = 1$  and  $L_y = L_z = 0$ . For the electric field component oriented in the y-direction or the z-direction

$$(f_0 + f_1)\varepsilon_{eff}^2 = (f_0\varepsilon_0 + f_1\varepsilon_1)\varepsilon_{eff}, \quad (3.57)$$

so that when  $f_0 + f_1 = 1$

$$\varepsilon_{eff} = \frac{f_0\varepsilon_0 + f_1\varepsilon_1}{(f_0 + f_1)} = (1 - f_1)\varepsilon_0 + f_1\varepsilon_1 \quad (3.58)$$

which agrees with equation (3.47). For the component of the electric field in the x-direction

$$[-f_0\varepsilon_1 - f_1\varepsilon_0]\varepsilon_{eff} + (f_0 + f_1)\varepsilon_0\varepsilon_1 = 0, \quad (3.59)$$

so that when  $f_0 + f_1 = 1$

$$\frac{1}{\varepsilon_{eff}} = \frac{(f_0\varepsilon_1 + f_1\varepsilon_0)}{(f_0 + f_1)\varepsilon_0\varepsilon_1} = (1 - f_1)\frac{1}{\varepsilon_0} + f_1\frac{1}{\varepsilon_1}, \quad (3.60)$$

which agrees with equation (3.44).

For an array of thin needles oriented with their long axis in the z-direction,  $L_x = L_y = 1/2$  and  $L_z = 0$ . The effective permittivity direction will again be given by equation (3.57) while the effective permittivity in the x and y-directions will be given by solving the quadratic equation

$$\begin{aligned} & \frac{1}{2}[-(f_1 + f_2)]\varepsilon_{eff}^2 + \frac{1}{2}[(f_1 - f_2)(\varepsilon_1 - \varepsilon_2)]\varepsilon_{eff} + (f_1 + f_2)\varepsilon_1\varepsilon_2 \\ & = -\frac{1}{2}\varepsilon_{eff}^2 + \frac{1}{2}[(2f_1 - 1)(\varepsilon_1 - \varepsilon_2)]\varepsilon_{eff} + \varepsilon_1\varepsilon_2 = 0 \end{aligned} \quad (3.61)$$

In chapter 4 it will be shown that a model based on a generalized ABEMA can provide a computationally efficient method for modeling the effects of LER in scatterometry measurements. A MATLAB™ m-file for calculating the effective index values using the ABEMA is included in Appendix F.

## CHAPTER 4: NUMERICAL RESULTS

Line edge roughness (LER) has been identified as a potentially significant source of uncertainty for optical scatterometry measurements<sup>161</sup>. While witness gratings that are measured using optical scatterometry are typically one-dimensionally periodic (at least at the moment), roughness tends to break the transverse symmetry of the system and imposes an inherently three-dimensional nature to the problem. The computational resources needed to numerically model these systems can increase quickly as more Fourier coefficients (or smaller grid sizes) are needed for the solutions to converge. An approximation technique which restores the problem to a one-dimensionally periodic system would reduce the computational expense of adding LER to optical scatterometry models.

In this chapter, scatterometry signatures from a randomly rough periodic grating were calculated using a 2D RCWA algorithm and compared with the results from a 1D RCWA model that replaced the roughness by an effective medium layer (Figure 16).

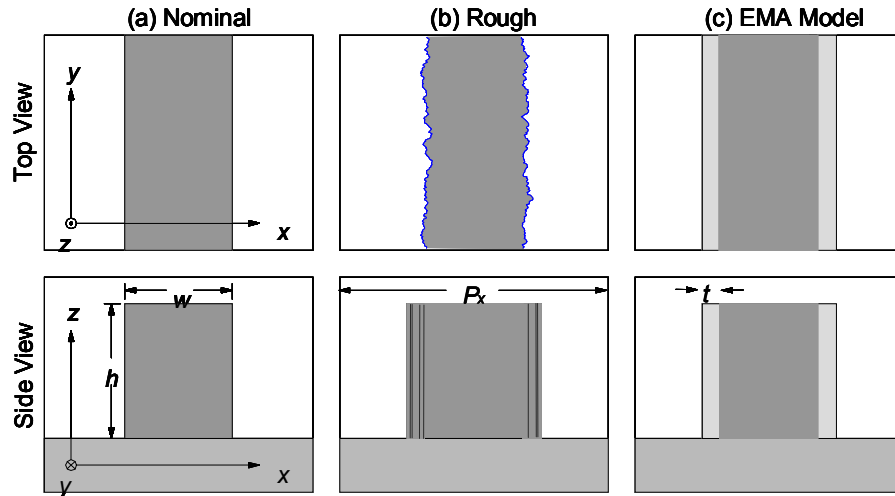


Figure 16 Examples of the index profiles within a one period by one period cell used in the simulations. The figures show (a) the nominal profile, (b) a 2D periodic profile used to directly calculate the effect of LER using a 2D RCW algorithm, and (c) a 1D periodic profile used to approximate the effect of the LER with an effective medium layer. Profiles with a large peak to valley roughness are shown for clarity. Much smaller roughness amplitudes were used in the simulations. The dark areas correspond to areas containing the grating material, the gray area corresponds to the effective medium layer, and the light areas correspond to areas containing the fill material.

The comparisons between the models are based on a nominal unperturbed silicon grating with vertical sidewalls, a period of  $P_x = 200$  nm, a linewidth of  $w = 100$  nm, and a height of  $h = 200$  nm. The structure of the nominal grating is illustrated in Figure 16(a). Roughness was simulated by perturbing the edges of the grating as shown in Figure 16(b). The sides of the line were modulated independently, corresponding to uncorrelated LER. The 2D RCW algorithm must be used to model this structure. For the EMA models, the modulated regions of Figure 16(b) are replaced by uniform effective medium layers illustrated in Figure 16(c). This structure can be modeled with a 1D RCW algorithm, yielding a significant savings in computational expense.

#### 4.1. Rigorous Models of Gratings with LER

The RCWA algorithm requires that the electric and magnetic fields are each expanded in a Floquet series. The algorithm converges on an exact solution when the number of Floquet expansion orders ( $G$ ) that are retained for the calculation approaches infinity. However, the number of operations that are needed for the computation is proportional to  $G^3$  for the 1D RCW algorithm. For the 2D RCW algorithm this increase to  $G_x^3$  for the grating direction and  $G_y^3$  for the transverse direction, where  $G_x$  and  $G_y$  are the number of terms that are retained in each direction. For the examples in this chapter, the expansions were truncated to  $\pm 10$  orders in each dimension, corresponding to a total of 21 total orders for the one-dimensionally periodic gratings. For the two-dimensionally periodic gratings the orders were truncated to  $\pm 10$  orders in the direction along the grating vector and  $\pm 20$  orders on the transverse direction, for a total of 841 orders. By examining the relative change in the results of the 2D RCW calculation as more orders were added, the numerical error in the calculated reflectance due to the truncation of the Fourier series was estimated to be less than 0.005.

Various roughness profiles with known statistics were created using the procedure outlined by Zhao et. al.<sup>137</sup>. In summary, the procedure involves:

1. Calculating the auto-correlation (ACF) function for the desired profile
2. Using the Wiener-Khinchin theorem to calculate the power spectral density (PSD) of the profile.
3. Multiplying the square root of the PSD by a random phase function.
4. Taking the inverse Fourier transform to recover a random profile in the spatial domain with a known PSD.

This was the method used to create the profiles shown earlier in section 2.3. A MATLAB™ m-file for generating self-affine profiles is included in Appendix F. In practice, a separate realization of the roughness profile was generated for every change of variable in the input to the 2D RCWA algorithm (such as wavelength or angle of incidence). An average of fifteen realizations was sufficient to obtain a reasonable convergence; the standard difference between the mean of fourteen iterations and the mean of fifteen iterations was an order of magnitude smaller than the numerical errors due to the truncation of the Fourier series.

#### 4.2. Effects of Roughness Parameters on the Scatterometry Signal

Figure 17 shows the angle-resolved reflectance for the nominal grating probed with a wavelength of 633 nm as predicted by the 2D RCW calculations. The grating is oriented such that the grating vector lies in the plane of incidence (classical mounting). The electric field for s-polarization (often called transverse-electric or TE polarization) and the magnetic field for p-polarization (often called transverse-magnetic or TM polarization) are normal to the grating vector and parallel to the lines. Initial simulations confirmed that, even for large rms roughness values, the coupling between polarizations is less than 1 part in  $10^6$  for gratings in the classical mounting. Therefore, for this analysis, the specular reflectance for each polarization is considered independently. The reflectance differences are larger for some incident angles than for others, and for this particular example, the p-polarized reflectance is much less sensitive to the roughness than the s-polarized reflectance.

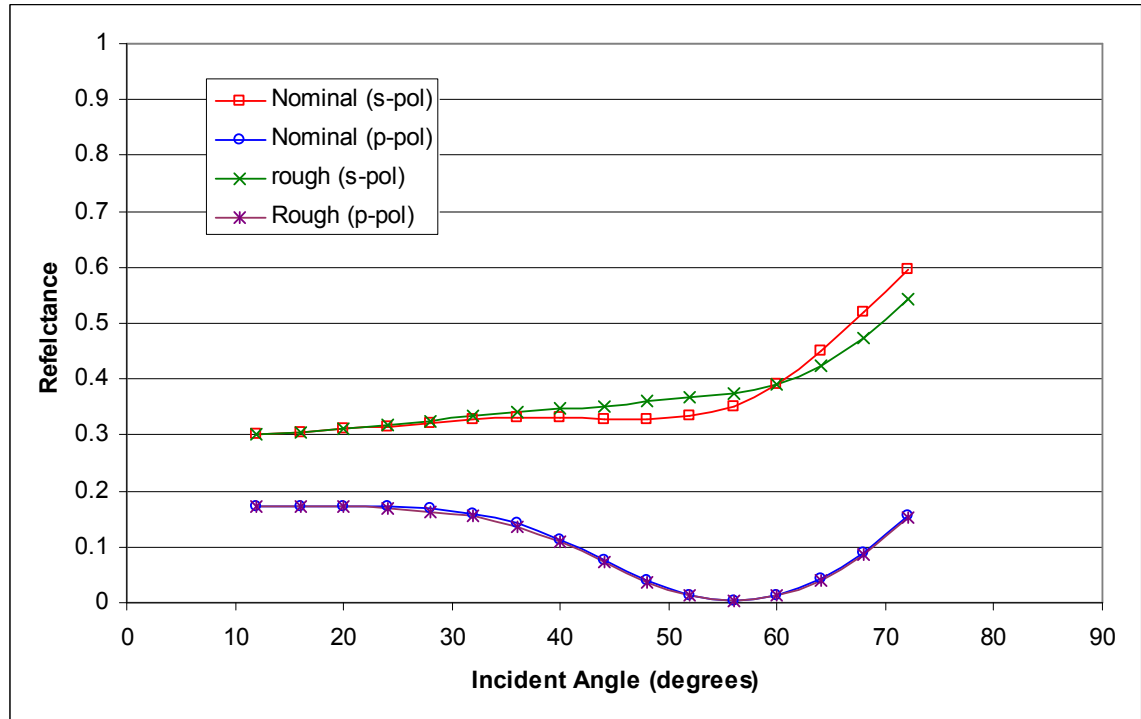
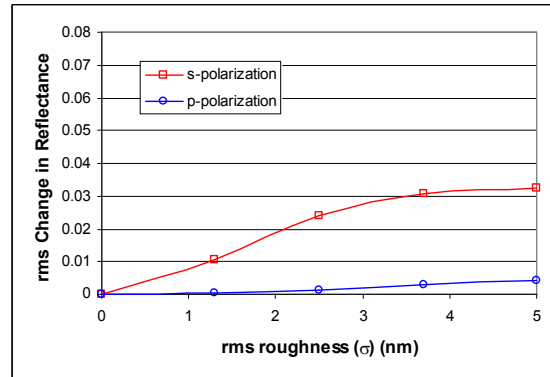
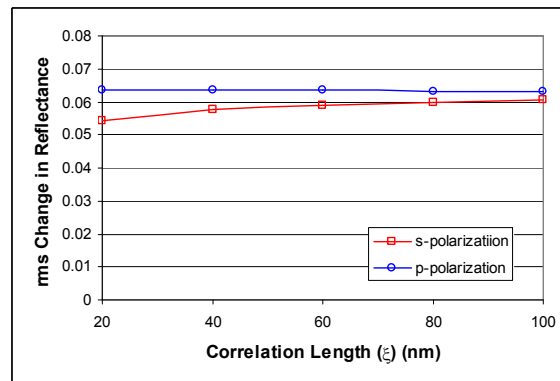


Figure 17 Angle resolved scattering signal (reflectance) from a silicon grating with a 200nm pitch, 100 nm width, and 200 nm depth simulated for a 632.8 nm wavelength incident beam. The curves are for the ( $\square$ ) s-polarization and ( $\circ$ ) p-polarization reflectance from the nominal grating and for ( $\times$ ) s-polarization and ( $*$ ) p-polarization for a grating with LER defined by  $\sigma = 2.5$  nm,  $\xi = 20$  nm, and  $\alpha = 0.5$ . For this particular example the change in the p-polarization due to the LER is small.

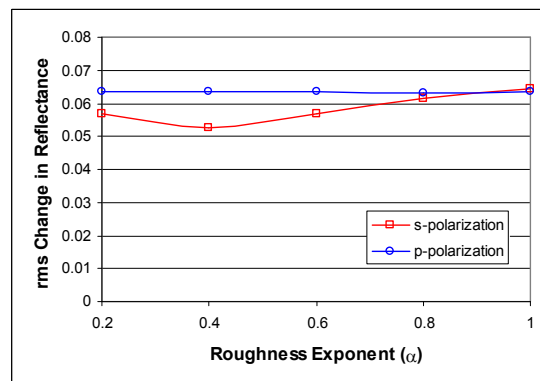
Figure 18 shows the rms difference between the nominal grating and a grating with line width roughness as a function of the three roughness parameters described in section 2.3. These graphs indicate that the change in the reflectance signal due to line width roughness is a function not only of the rms amplitude of the roughness, but also its correlation length and, to some extent, the relative frequency content of the roughness as expressed by the roughness exponent. Therefore, it would not be reasonable to expect that a single effective medium approximation could perfectly model the line width roughness characterized by a range of roughness parameters using only the effective medium layer thickness ( $t$ ) as a variable.



(a)



(b)



(c)

Figure 18 Graphs indicating the relative effects of variations in the rms amplitude ( $\sigma$ ), correlation length ( $\xi$ ), and roughness exponent ( $\alpha$ ) of the line width roughness on the angle resolved scattering signal from a silicon grating with a 200nm pitch, 100 nm width, and 200 nm depth simulated for a 632.8 nm wavelength incident beam. For each graph the line width roughness is defined by (a)  $\alpha = 0.5$ ,  $\xi = 20$  nm and various rms roughness amplitudes ( $\sigma$ ) from 0.5 nm to 5 nm (b)  $\sigma = 2.5$  nm,  $\alpha = 0.5$ , and various correlation lengths ( $\xi$ ) from 10 nm to 100 nm; (c)  $\sigma = 2.5$  nm,  $\xi = 20$  nm, and various roughness exponents ( $\alpha$ ) from 0.1 to 1.

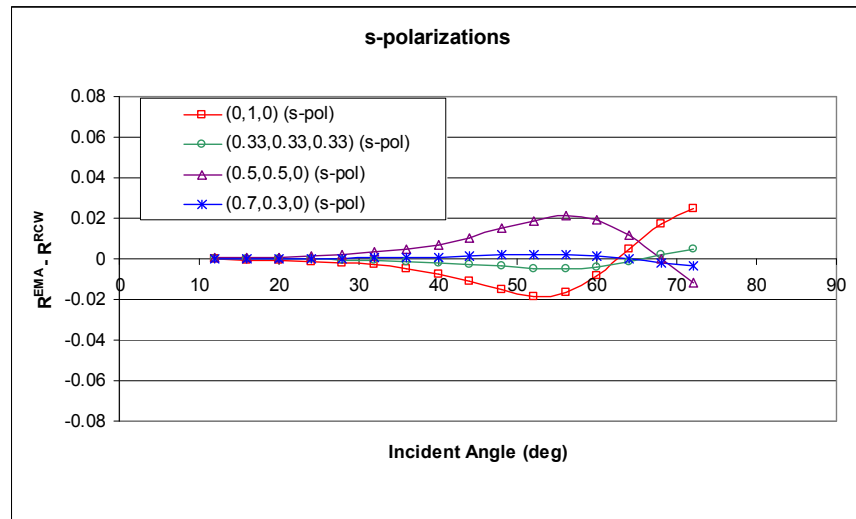
### 4.3. Optimization of ABEMA Parameters for a Specific Example

First, an attempt was made to find a set of effective medium parameters that can be used to model the effects of LER predicted by the 2D RCW calculations for a specific set of roughness parameters and then generalize that model. An examination of the literature on line width roughness<sup>133,134,136,138,212-214</sup> indicates that typical values for the correlation length range between 5 nm and 30 nm, roughness exponents can range between 0.15 and 1, and typical rms roughness values are around 2.5 nm. For a specific example we will examine the fit between different effective medium models and a grating with LER characterized by  $\sigma = 2.5$  nm,  $\xi = 20$  nm, and  $\alpha = 0.5$ .

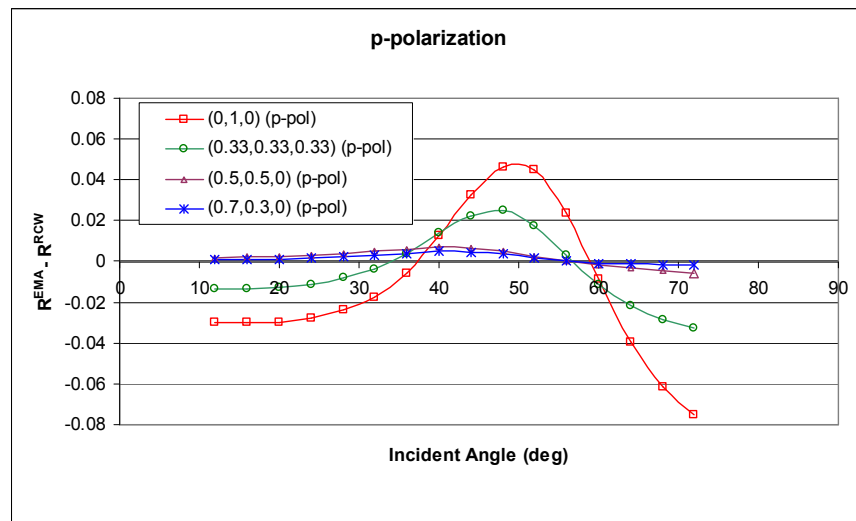
The quality of the fit between the data calculated using the 2D RCW algorithm and the data calculated using a particular EMA model can be quantitatively expressed using an objective function (S)<sup>125</sup>. For this case a weighting factor was chosen such that:

$$S = \sqrt{\frac{\sum_{i=1}^N (x_i^{EMA} - x_i^{RCW})^2}{N}} \quad (4.1)$$

where  $N$  is the number of data points,  $x_i^{EMA}$  is the  $i_{th}$  data point calculated using the EMA model, and  $x_i^{RCW}$  is the mean of the  $i_{th}$  data point calculated using the 2D RCW algorithm. This is simply the root mean square difference between the two data sets. The term in the numerator  $(x_i^{EMA} - x_i^{RCW})$  is referred to as the *residual difference*.



(a)



(b)

Figure 19 Residual difference between reflectance from the grating with LER defined by  $\sigma = 2.5$  nm,  $\xi = 20$  nm,  $\alpha = 0.5$  calculated using a 2D RCW algorithm and the reflectance calculated using a 1D RCW algorithm and ( $\square$ ) an ABEMA with  $(L_x, L_y, L_z) = (0, 1, 0)$ ,  $f = 50\%$ , and  $t = 2\sigma$ ; ( $\circ$ ) an ABEMA with  $(L_x, L_y, L_z) = (0.33, 0.33, 0.33)$ ,  $f = 50\%$ , and  $t = 2\sigma$ ; ( $\Delta$ ) an ABEMA with  $(L_x, L_y, L_z) = (0.5, 0.5, 0)$ ,  $f = 50\%$ , and  $t = 2\sigma$ ; and ( $*$ ) an ABEMA with  $(L_x, L_y, L_z) = (0.7, 0.3, 0)$ ,  $f = 50\%$ , and  $t = 2\sigma$  for (a) s-polarization and (b) the p-polarization. The nominal grating has a pitch  $P_x = 200$  nm, width  $w = 100$  nm, and height  $h = 200$  nm.

The graphs in Figure 19 show these residual differences in the reflectance calculated using the 2D RCW algorithm applied to LER with  $\sigma = 2.5$  nm,  $\xi = 20$  nm, and  $\alpha = 0.5$  and the reflectance calculated using a 1D RCW algorithm and ABEMAs with different sets of parameters. The effective index values used for the ABEMA were calculated using the MATLAB™ m-file in Appendix F. For any particular combination of best fit depolarization factors there was a specific effective medium layer thickness that minimized the objective function. Because of the computational efficiency gained by using the ABEMA model, it was possible to search through various EMA parameter sets for a combination of depolarization factors ( $L_x, L_y, L_z$ ) and fill factors ( $f$ ) that minimized the objective function for any particular effective medium layer thickness ( $t$ ). For the sample case with a layer thickness of  $2\sigma = 5.0$  nm and a LER characterized by  $\sigma = 2.5$  nm,  $\xi = 20$  nm, and  $\alpha = 0.5$ , the objective function had a minimum for  $(L_x, L_y, L_z) = (0.7, 0.3, 0)$  and  $f = 50$  %. In addition:

1. The fit for the p-polarization is relatively insensitive to changes in  $L_x$  and  $L_y$  while the fit for the s-polarization is very sensitive to changes in these parameters.
2. The fit for the p-polarization is sensitive to changes in  $L_z$  while the fit for the s-polarization is dominated by changes in  $L_x$  and  $L_y$ .
3. The best fit values for  $L_z$  depends on the fill factor.
4. The best fit values of  $L_x$  and  $L_y$  depend on the correlation length ( $\xi$ ) of the roughness (see Figure 20).

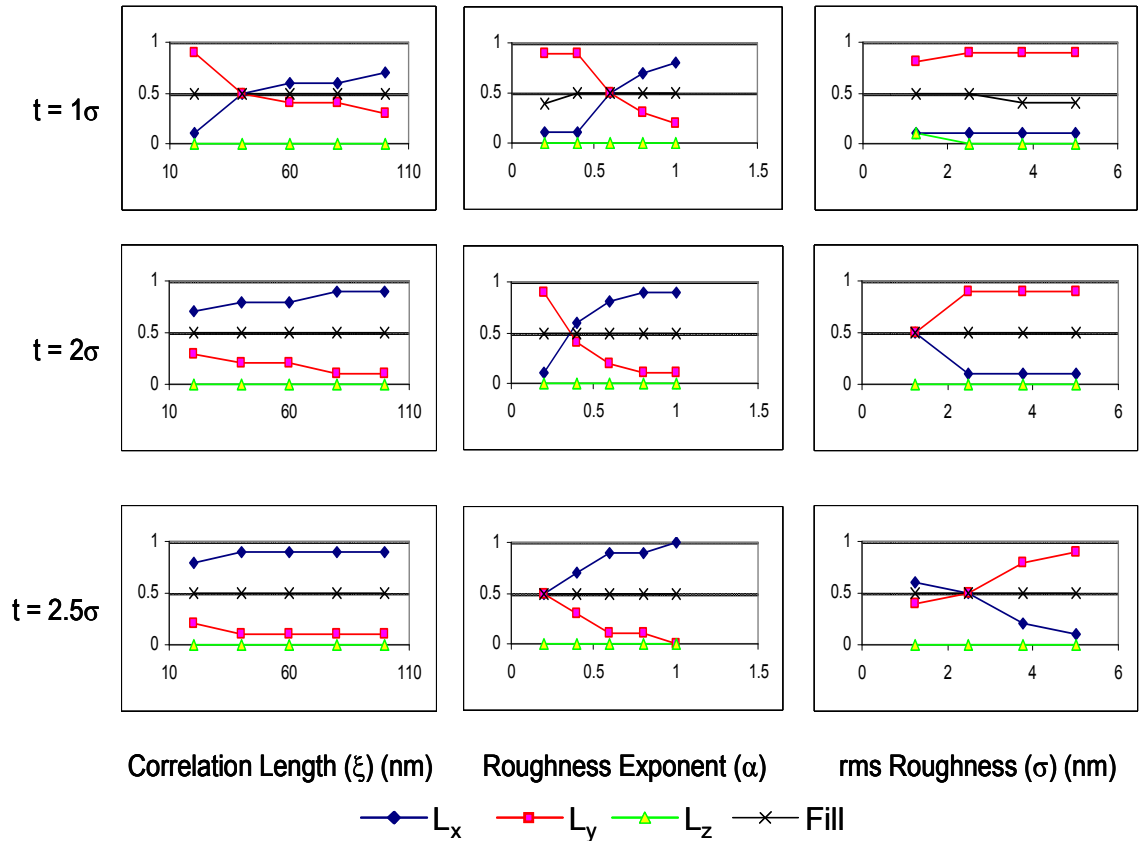


Figure 20 Best fit EMA parameters ( $\diamond$ )  $L_x$ , ( $\blacksquare$ )  $L_y$ , ( $\Delta$ )  $L_z$ , and ( $\times$ ) fill factor as a function of (left hand column) correlation length ( $\xi$ ); (central column) roughness exponent ( $\alpha$ ), and (right hand column) rms roughness ( $\sigma$ ) for the grating with LER defined by  $\sigma = 2.5$  nm,  $\xi = 20$  nm, and  $\alpha = 0.5$  calculated using a 2D RCW algorithm and the reflectance calculated using a 1D RCW algorithm and an EMA with fill factor  $f = 50\%$ , and (top row) effective medium layer thickness  $t = 1\sigma$ , (middle row)  $t = 2\sigma$ , and (bottom row)  $t = 2.5\sigma$ . The nominal grating has a pitch  $P_x = 200$  nm, width  $w = 100$  nm, and height  $h = 200$  nm. The best fit parameters are determined by minimizing the root sum square of objective functions for the s-polarization and for the p-polarization reflectance.

#### 4.4. Limits of Extension of Optimized Model to Other Examples

The next step is to attempt to extend the ABEMA model to other measurement configurations. Not only may this help to reduce the expense in calculating the theoretical wavelength resolved spectra for real gratings, but it also provides some insight into the limits of the EMA models. To this end, the 2D RCWA algorithm was used to

calculate the wavelength resolved specular reflectance at a 65 degree incident angle for the nominal grating with LER characterized by  $\sigma = 2.5$  nm,  $\xi = 20$  nm, and  $\alpha = 0.5$  and compared the data to similar results calculated using the optimized ABEMA model.

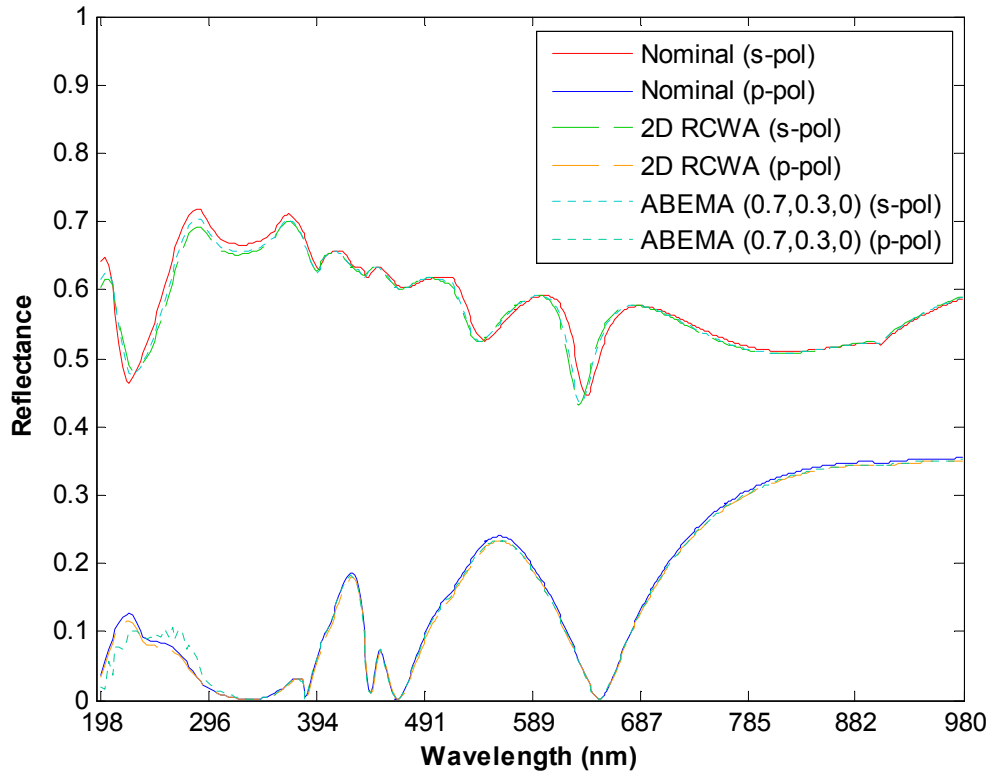


Figure 21 Wavelength dependent specular reflectance for an incident angle of 65 degrees for the nominal grating with a pitch  $P_x = 200$  nm, width  $w = 100$  nm, and height  $h = 200$  nm (solid lines), for the grating with LER defined by  $\sigma = 2.5$  nm,  $\xi = 20$  nm,  $\alpha = 0.5$  calculated using a 2D RCW algorithm (long-dashed lines), and for the grating with an effective medium layer defined by  $(L_x, L_y, L_z) = (0.5, 0.5, 0)$ ,  $f = 50\%$ , and  $t = 2\sigma$ . The upper curves are for the s-polarization and the lower curves are for the p-polarization.

Just as for the angle resolved data, the ABEMA model matches the 2D RCW calculations for the s-polarization for long wavelengths. The ABEMA model matches the 2D RCW very well for longer wavelengths ( $S < 0.007$  between 600 nm and 980 nm) but starts to deviate for wavelengths less than 400 nm ( $S = 0.012$  between 198 nm and 400 nm). Since the RCWA is slower to converge for shorter wavelengths, care must be

taken when drawing conclusions about the wavelength dependent fit of the ABEMA model to the 2D RCWA model. However, the ABEMA model seems to break down when the correlation length of the roughness is greater than approximately 1/20 of the incident wavelength. This is consistent with the long wavelength approximation used the ABEMA derivation. Maxwell Garnett's EMA formulation assumes that the inclusions are much smaller than the wavelength.

Finally, the optimum ABEMA model ( $L_x = 0.7$ ,  $L_y = 0.3$ ,  $L_z = 0$ ,  $f = 50\%$ ) that was developed for the nominal grating ( $P_y = 200$  nm,  $w = 100$  nm,  $d = 200$  nm) was applied to other, related gratings. In the first case the line width ( $w$ ) was changed to 50 nm (25% of the grating pitch) and then to 150 nm (75% of the grating pitch). The model was also applied to shallow ( $h = 50$  nm) and deep ( $h = 500$  nm) gratings. The results are shown in Figure 22.

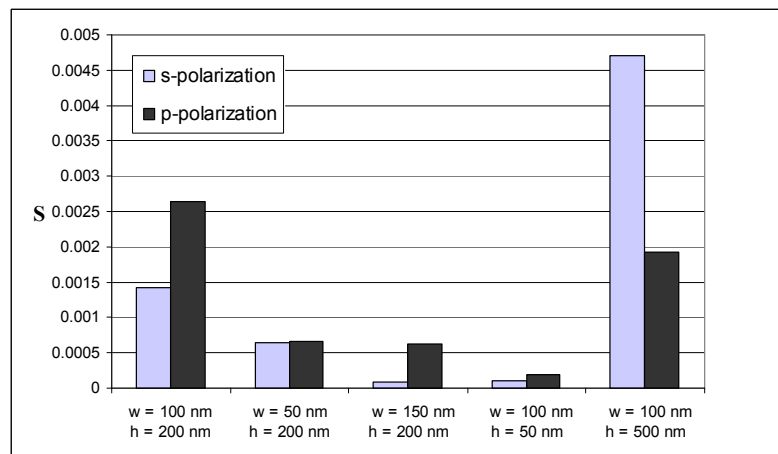


Figure 22 Objective functions (rms difference between the angularly resolved scattering data calculated using the 2D RCW algorithm and the angularly resolved scattering data calculated using the EMA model with  $(L_x, L_y, L_z) = (0.7, 0.3, 0)$  and 50% fill for various gratings with LER defined by  $s = 2.5$  nm,  $x = 20$  nm,  $a = 0.5$ . The nominal grating has a pitch ( $P_x$ ) of 200 nm, a width ( $w$ ) of 100 nm, and a height ( $h$ ) of 200 nm. Either the width ( $w$ ) or height ( $h$ ) of the grating was changed for the other four examples.

The ABEMA model worked just as well for the gratings with different line widths as for the nominal grating for which it was developed. This has important implications if the ABEMA model is to be used to study the effect that LER might have on critical dimension (CD) measurements using optical scatterometry. However, the ABEMA model did not work well for modeling gratings with different heights. While the actual fits for the shallow grating ( $h = 50$  nm) are significantly better than the other gratings, this is misleading because the change in the signal due to LER is very small in this instance. The fits for the deep grating ( $h = 500$  nm) show that the ABEMA that was optimized for modeling LER on the nominal grating does not work well for gratings with different heights. Intuitively this seems reasonable. The relationship between the rms roughness value and the height of the grating does not change for gratings with different line widths. However, for gratings with different heights, the ratio between the height ( $h$ ) and the thickness ( $t$ ) of the effective medium layer changes (see the side view in Figure 16) and it might be expected to have a different set of optimum depolarization values.

## CHAPTER 5: CONCLUSIONS

A generalized anisotropic Bruggeman effective medium approximation (ABEMA) was developed as an alternative to 2D RCWA simulation for modeling the effect of edge roughness on optical scatterometry signals. The ABEMA model provides a less computationally expensive method for modeling LER than models using 2D RCWA. The computation time needed to model the effect of LER on a single angle resolved optical scatterometry signature was reduced from more than one and a half hours to less than ten seconds for the example presented in Chapter 4. LER is becoming an increasingly important factor in semiconductor process control<sup>118</sup> and edge roughness will be an important factor in determining the performance planar photonic crystal devices.<sup>53</sup> This less computationally expensive model will make it practical to include edge roughness effects in optical scatterometry models so that the uncertainty contributions due to edge roughness can be appropriately considered. It may also enable to direct measurement of edge roughness using optical scatterometry techniques.

Chapter 1 presented a brief overview of some of the applications of micro-structured surfaces, the fabrication techniques that are used to make these surfaces, and the measurement techniques that might be used to control the fabrication process. Optical scatterometry is introduced as a rapid, non-destructive, and precise method for measuring micro-structured surfaces. In Chapter 2, optical scattering was discussed as a method for measuring surface roughness. The Rayleigh-Rice perturbation theory has been used to

model scattering from optically smooth surfaces<sup>121,122</sup> while effective medium approximations have been used to model interfacial roughness in thin film stacks<sup>215</sup>. In a similar manner, the volume current perturbation theory outlined in Chapter 3 might be used for modeling long correlation length variations in grating structures, while an effective medium theory may prove useful in modeling edge roughness with characteristic length scales that are much less than the wavelength of the light used to interrogate the structure.

In chapter 4 it is shown that simple periodic structures do not give the same results as a more realistic LER model based on self-affine functions so that a more complicated model is required to model the effects of realistic edge roughness. This more complicated model required an average of 2D RCWA calculations for multiple realizations of uncorrelated self-affine functions. Various EMA models were compared to the 2D RCWA results for a specific grating and a specific set of roughness parameters. A form birefringence effective medium approximation (FBEMA) has been proposed in the patent literature and isotropic Bruggeman effective medium approximation (IBEMA) that is commonly used to model interfacial roughness in ellipsometric measurements of thin film stacks. While the results from these models generally follow the changes caused by the LER, it was shown that a generalized ABEMA can be optimized to more closely approximate the 2D RCWA results for a specific set of roughness parameters. This approximation can be used to greatly reduce the time needed to evaluate the effects of edge roughness in optical scatterometry measurements. By optimizing the ABEMA parameters, the useful range of effective medium approximations has been extended.

Further work is needed to probe the limits of the ABEMA model and to examine the possible overlap with perturbation<sup>197</sup> and mean field<sup>157</sup> techniques. The ABEMA model would not be expected to work well for roughness with correlation lengths that are not small compared to the wavelength of light. However perturbation techniques and mean field techniques would not be expected to work well for sharp deviations from the nominal grating. The perturbation techniques that are developed in Chapter 3 for the PWE method need to be extended to the RCWA algorithm and the results of all three approximation methods need to be compared with rigorous simulations of optical scatterometry signals from gratings with LER having a range of correlation lengths.

In this work it was not possible to directly compare either the rigorous numerical results or results from the approximation to experimental data. The LER artifacts that were fabricated by using e-beam lithography had much longer correlation lengths than can be modeled using the ABEMA. In addition the sample areas that were practical using high resolution e-beam lithography were too small to be measured with scatterometry systems without introducing bias due to overfilling the sample area. The background signal from the area around the sample region might be separated from the desired signal by measuring more elements of the Mueller matrix<sup>216,217</sup>. Because of the long correlation length of the LER artifacts that were fabricated, perturbation techniques or mean field approximations might be more appropriate for modeling measured data. LER artifacts with larger sample areas and more realistic LER statistics might be created by varying the process conditions used to fabricate replicated gratings.<sup>218</sup>

If these models presented in this dissertation are to be incorporated into commercial scatterometry systems more comprehensive studies over a larger range of grating

parameters, roughness parameters, and measurement conditions will be needed to confirm the robustness of the model. Optimum ABEMA parameters will need to be determined for each specific system, but may be extended to other systems as described in Chapter 4. Round-robin studies have compared measurements of LER from SEM images<sup>149,153</sup>, and CD-SAXS data<sup>219</sup> with measurements taken from AFM profiles. Similar studies will need to be conducted to compare LER measurements from optical scatterometry data to these other techniques.

## REFERENCES

1. C. J. Evans and J. B. Bryan, "Structured, Textured or Engineered Surfaces," CIRP Annals - Manufacturing Technology 48(2), 541-556 (1999).
2. K. Stout, "Engineering Surfaces - a Philosophy of Manufacture (A Proposal for Good Manufacturing Practice) " Journal of Engineering Manufacture, 212(3), 169 - 174 (1998).
3. P. M. Lonardo, D. A. Lucca and L. D. Chiffre, "Emerging trends in surface metrology," CIRP Annals - Manufacturing Technology 51(2), 701-723 (2002).
4. *Economic impact of measurement in the semiconductor industry*, National Institute of Standards and Technology, Gaithersburg, MD (1997).
5. N. J. Shirtcliffe, G. McHale, M. I. Newton and G. Chabrol, "Dual-scale roughness produces unusually water-repellent surfaces " Adv. Mater, 16, 1929-19832 (2004).
6. B. R. D'Urso and J. T. Simpson, "Composite, Nanostructured, Super-Hydrophobic Material", USPTO 7,258,731 (2007).
7. J. Atencia and D. J. Beebe, "Controlled microfluidic interfaces," Nature, 437(7059), 648-655 (2005).
8. R. Blossey, "Self-cleaning surfaces - virtual realities," Nature Materials, 2(301-306 (2003).
9. C. Donnet and A. Erdemir, "Solid lubricant coatings: recent developments and future trends," Tribology Letters, 17(3), 389-397 (2004).
10. A. Erdemir, "Review of engineered tribological interfaces for improved boundary lubrication," Tribology International, 38(3), 249-256 (2005).
11. M. Geiger, S. Roth and W. Becker, "Influence of laser-produced microstructures on the tribological behaviour of ceramics," Surface and Coatings Technology, 100-101(17-22 (1998).
12. F. H. Jones, "Teeth and bones: applications of surface science to dental materials and related biomaterials," Surface Science Reports, 42(3-5), 79-205 (2001).

13. D. W. Hutmacher, M. Sittinger and M. V. Risbud, "Scaffold-based tissue engineering: rational for computer aided design and solid free-form fabrication systems," *Trends in Biotechnology*, 22(7), 354-362 (2004).
14. F. Pfiffer, B. Herzog, D. Kern, L. Schniedeler, J. Geis-Gerstorfer and H. Wolburg, "Cell reactions to microstructures implant surfaces," *Microelectronic Engineering* 67-68, 913-922 (2003).
15. S. H. Lee, *Diffractive and Miniaturized Optics* SPIE, Bellingham, WA (1993).
16. J. N. Mait and D. W. Prather, *Selected papers on Subwavelength Diffractive Optics*, SPIE (2001).
17. D. C. O'Shea, T. J. Suleski, A. D. Kathman and D. W. Prather, *Diffractive Optics: Design, Fabrication, and Test*, SPIE Press, Bellingham, WA (2004).
18. P. Lalanne and D. Lemerrier, "On the effective medium theory of subwavelength periodic structures," *Journal Of Modern Optics*, 43(10), 2063-2085 (1996).
19. T. Gaylord, W. E. Baird and M. G. Moharam, "Zero-reflectivity high spatial-frequency rectangular-groove dielectric surface-relief gratings," *Applied Optics*, 25(24), 4562-4567 (1986).
20. M. E. Motamedi, W. H. Southwell and W. J. Gunning, "Antireflection surfaces in silicon using binary optics technology," *Applied Optics*, 31(22), 4371-4376 (1992).
21. Z. N. Yu, H. Gao, W. Wu, H. X. Ge and S. Y. Chou, "Fabrication of large area subwavelength antireflection structures on Si using trilayer resist nanoimprint lithography and liftoff," *Journal Of Vacuum Science & Technology B*, 21(6), 2874-2877 (2003).
22. H. Kikuta, Y. Ohira and K. Iwata, "Achromatic quarter-wave plates using the dispersion of form birefringence," *Applied Optics*, 36(7), 1566-1572 (1997).
23. Z. N. Yu, P. Deshpande, W. Wu, J. Wang and S. Y. Chou, "Reflective polarizer based on a stacked double-layer subwavelength metal grating structure fabricated using nanoimprint lithography," *Applied Physics Letters*, 77(7), 927-929 (2000).

24. P. C. Deguzman and G. P. Nordin, "Stacked subwavelength gratings as circular polarization filters," *Applied Optics*, 40(31), 5731-5737 (2001).
25. E. Hasman, Z. Bomzon, A. Niv, G. Biener and V. Kleiner, "Polarization beam-splitters and optical switches based on space-variant computer-generated subwavelength quasi-periodic structures," *Optics Communications*, 209(1-3), 45-54 (2002).
26. Y. Gorodetski, G. Biener, A. Niv, V. Kleiner and E. Hasman, "Space-variant polarization manipulation for far-field polarimetry by use of subwavelength dielectric gratings," *Optics Letters*, 30(17), 2245-2247 (2005).
27. J. D. Joannopoulos, R. D. Mead and J. N. Winn, *Photonic crystals: Molding the flow of light*, Princeton University Press, Princeton (1995).
28. S. John, "Strong localization of photons in certain disordered dielectric superlattices," *Physical Review Letters*, 58(23), 2486 (1987).
29. E. Yablonovitch, "Inhibited spontaneous emission in solid-state physics and electronics," *Physical Review Letters*, 58(20), 2059-2062 (1987).
30. J. P. Dowling, "Photonic & Sonic Band-Gap and Metamaterial Bibliography," Available at <http://phys.lsu.edu/~jdowling/pbgbib.html>, (2008).
31. S. Johnson, *SC608: Photonic crystals: A crash course, from bandgaps to fibers*, SPIE, San Jose, CA (2007).
32. L. Rayleigh, "On the maintenance of vibrations by forces of double frequency, and on the propagation of waves through a medium endowed with a periodic structure," *Philosophical Magazine*, 24(145-159) (1887).
33. C. Kittel, *Introduction to Solid State Physics*, John Wiley & Sons, New York (1968).
34. S. Berthier, E. Charron and A. Da Silva, "Determination of the cuticle index of the scales of the iridescent butterfly *Morpho menelaus*," *Optics Communications*, 228(4-6), 349-356 (2003).
35. Smithsonian National Museum of Natural History, "Western Cultures Exhibit", (Washington, D.C., 2008).

36. S. Assefa, S. J. McNab and Y. A. Vlasov, "Transmission of slow light through photonic crystal waveguide bends," *Opt. Lett.*, 31(6), 745-747 (2006).
37. H. Gersen, T. J. Karle, R. J. P. Engelen, W. Bogaerts, J. P. Korterik, N. F. van Hulst, T. F. Krauss and L. Kuipers, "Real-space observation of ultraslow light in photonic crystal waveguides," *Physical Review Letters*, 94(7), (2005).
38. M. Soljacic, S. G. Johnson, S. H. Fan, M. Ibanescu, E. Ippen and J. D. Joannopoulos, "Photonic-crystal slow-light enhancement of nonlinear phase sensitivity," *Journal Of The Optical Society Of America B-Optical Physics*, 19(9), 2052-2059 (2002).
39. H. Kosaka, T. Kawashima, A. Tomita, M. Notomi, T. Tamamura, T. Sato and S. Kawakami, "Superprism phenomena in photonic crystals," *Physical Review B*, 58(16), 10096-10099 (1998).
40. M. Notomi, K. Yamada, A. Shinya, J. Takahashi, C. Takahashi and I. Yokohama, "Extremely large group-velocity dispersion of line-defect waveguides in photonic crystal slabs," *Physical Review Letters*, 87(25), (2001).
41. J. M. Lourtioz, H. Benisty, A. Chelnokov, S. David and S. Olivier, "Photonic crystals and the real world of optical telecommunications," *Annales Des Telecommunications-Annals Of Telecommunications*, 58(9-10), 1197-1237 (2003).
42. H. K. Cho, J. Jang, J. H. Choi, J. Choi, J. Kim, J. S. Lee, B. Lee, Y. H. Choe, K. D. Lee and S. H. Kim, "Light extraction enhancement from nano-imprinted photonic crystal GaN-based blue light-emitting diodes," *Optics Express*, 14(19), 8654-8660 (2006).
43. W. H. Southwell, "Pyramid-array surface-relief structures producing antireflection index matching on optical surfaces," *J. Opt. Soc. Am.*, 8(3), 549-553 (1991).
44. H.-Y. Ryu, J.-K. Hwang, Y.-H. Lee and A. Y.-H. Lee, "Enhancement of light extraction from two-dimensional photonic crystal slab structures," *IEEE Journal of Selected Topics in Quantum Electronics*, 8(2), 231-236 (2002).
45. A. A. Erchak, D. J. Ripin, S. Fan, P. Rakich, J. D. Joannopoulos, E. P. Ippen, G. S. Petrich and L. A. Kolodziejski, "Enhanced coupling to vertical radiation using a two-dimensional photonic crystal in a semiconductor light-emitting diode," *Applied Physics Letters*, 78, 563 (2001).

46. M. Boroditsky, T. F. Krauss, R. Coccioli, R. Vrijen, R. Bhat and E. Yablonovitch, "Light extraction from optically pumped light-emitting diode by thin-slab photonic crystals," *Applied Physics Letters*, 75(8), 1036-1038 (1999).
47. P. Bermel, C. Luo, L. Zeng, L. C. Kimerling and J. D. Joannopoulos, "Improving thin-film crystalline silicon solar cell efficiencies with photonic crystals," *Optics Express*, 15(25), 16986-17000 (2007).
48. I. A. M. Barnett and M. G. Mauk, "Thin active-layer solar cell with multiple internal reflections", USPTO 4,818,337 (1989)
49. E. Yablonovitch and G. D. Cody, "Intensity enhancement in textured optical sheets for solar cells," *Electron Devices, IEEE Transactions on*, 29(2), 300-305 (1982).
50. P. Sheng, A. N. Bloch and R. S. Stepleman, "Wavelength-selective absorption enhancement in thin-film solar cells," *Applied Physics Letters*, 43(579) (1983).
51. I. J. M. Gee, "Optically enhanced absorption in thin silicon layers using photonic crystals," at Photovoltaic Specialists Conference, 2002. Conference Record of the Twenty-Ninth IEEE (2002).
52. C. G. Poulton, M. Muller and W. Freude, "Scattering from sidewall deformations in photonic crystals," *Journal Of The Optical Society Of America B-Optical Physics*, 22(6), 1211-1220 (2005).
53. S. Hughes, L. Ramunno, J. F. Young and J. E. Sipe, "Extrinsic optical scattering loss in photonic crystal waveguides: Role of fabrication disorder and photon group velocity," *Physical Review Letters*, 94(3), (2005).
54. K. R. Maskaly, W. C. Carter, R. D. Averitt and J. L. Maxwell, "The effect of interfacial roughness on the normal incidence bandgap of one-dimensional photonic crystals," *Optics Express*, 13(21), 8380-8389 (2005).
55. T. P. Pearsall, D. Nedjlkovic, S. A. Kuchinsky, V. Goljatin and A. Y. Kutikov, "Measurement of losses in planar photonic crystals," *PROC SPIE 4655*, 53-62 (2002).
56. A. Rodriguez, M. Ibanescu, J. D. Joannopoulos and S. G. Johnson, "Disorder-immune confinement of light in photonic-crystal cavities," *Optics letters*, 30(23), 3192-3194 (2005).

57. E. Baravelli, A. Dixit, R. Rooyackers, M. Jurczak, N. Speciale and K. De Meyer, "Impact of Line-Edge Roughness on FinFET Matching Performance," *IEEE Transactions on Electron Devices*, 54(9), 2466-2474 (2007).
58. W. Steinhögl, G. Schindler, G. Steinlesberger, M. Traving and M. Engelhardt, "Impact of line edge roughness on the resistivity of nanometer-scale interconnects," *Microelectronic Engineering*, 76(1-4), 126-130 (2004).
59. M. J. Madou, *Fundamentals of Microfabrication: The Science of Miniturization*, CRC Press, Boca Raton, FL (2002).
60. S. R. J. Brueck and X. Chen, "Spatial frequency analysis of optical lithography resolution enhancement techniques," *Journal of Vacuum Science & Technology B: Microelectronics and Nanometer Structures*, 17, 908 (1999).
61. A. Yen, A. Tritchkov, J. P. Stirniman, G. Vandenberghe, R. Jonckheere and K. Ronse, "Characterization and correction of optical proximity effects in deep-ultraviolet lithography using behavior modeling," *Journal of Vacuum Science & Technology B: Microelectronics and Nanometer Structures*, 14, 4175 (1996).
62. E. Barouch, U. Hollerbach and R. R. Vallishayee, "OPTIMASK: an OPC algorithm for chrome and phase-shift mask design," *PROC SPIE 2440*, 192 (1995).
63. M. Hsu, D. Van Den Broeke, T. Laidig, K. E. Wampler, U. Hollerbach, R. Socha, J. F. Chen, S. Hsu and X. Shi, "Model-based scattering bars implementation for 65nm and 45nm nodes using IML technology," *PROC SPIE 5853*, 659 (2005).
64. A. Yen, S. S. Yu, J. H. Chen, C. K. Chen, T. S. Gau and B. J. Lin, "Low-k optical lithography for 100 nm logic technology and beyond," *Journal of Vacuum Science & Technology B: Microelectronics and Nanometer Structures*, 19, 2329 (2001).
65. M. Maenhoudt, J. Versluijs, H. Struyf, J. Van Olmen and M. Van Hove, "Double patterning scheme for sub-0.25  $\mu\text{m}$  single damascene structures at  $\text{NA} = 0.75$ ,  $\lambda = 193\text{nm}$ ," *PROC SPIE 5754*, 1508 (2005).
66. H. Nakamura, Y. Onishi, K. Sato, S. Tanaka, S. Mimotogi, K. Hashimoto and S. Inoue, "Contact hole formation by multiple exposure technique in ultralow k lithography," *Journal of Microlithography, Microfabrication, and Microsystems*, 4, 023005 (2005).

67. A. Feigel, Z. Kotler and B. Sfez, "Scalable interference lithography alignment for fabrication of three-dimensional photonic crystals," *Optics Letters*, 27(9), 746-748 (2002).
68. A. Feigel, Z. Kotler, B. Sfez, A. Arsh, M. Klebanov and V. Lyubin, "Chalcogenide glass-based three-dimensional photonic crystals," *Applied Physics Letters*, 77(3221) (2000).
69. H. H. Solak and C. David, "Patterning of circular structure arrays with interference lithography," *Journal Of Vacuum Science & Technology B*, 21(6), 2883-2887 (2003).
70. J. G. Goodberlet, J. T. Hastings and H. I. Smith, "Performance of the Raith 150 electron-beam lithography system," *Journal Of Vacuum Science & Technology B*, 19(6), 2499-2503 (2001).
71. M. Belotti, M. Galli, D. Bajoni, L. C. Andreani, G. Guizzetti, D. Decanini and Y. Chen, "Investigation of SOI photonic crystals fabricated by both electron-beam lithography and nanoimprint lithography," *Microelectronic Engineering*, 73-74, 405-411 (2004).
72. Y. Y. Huang, G. T. Paloczi, A. Yariv, C. Zhang and L. R. Dalton, "Fabrication and replication of polymer integrated optical devices using electron-beam lithography and soft lithography," *Journal Of Physical Chemistry B*, 108(25), 8606-8613 (2004).
73. M. A. Davies, C. J. Evans, R. R. Vohra, B. C. Bergner and S. R. Patterson, "Application of precision diamond machining to the manufacture of microphotonic components," *PROC SPIE* 5183, 94-108 (2003).
74. Y. N. Xia and G. M. Whitesides, "Soft lithography," *Angewandte Chemie-International Edition*, 37(5), 551-575 (1998).
75. S. Y. Chou, P. R. Krauss and P. J. Renstrom, "Nanoimprint lithography," *Journal Of Vacuum Science & Technology B*, 14(6), 4129-4133 (1996).
76. C. M. S. Torres, S. Zankovych, J. Seekamp, A. P. Kam, C. C. Cedeno, T. Hoffmann, J. Ahopelto, F. Reuther, K. Pfeiffer, G. Bleidiessel, G. Gruetzner, M. V. Maximov and B. Heidari, "Nanoimprint lithography: an alternative nanofabrication approach," *Materials Science & Engineering C-Biomimetic And Supramolecular Systems*, 23(1-2), 23-31 (2003).

77. M. T. Gale, "Replication techniques for diffractive optical elements," *Microelectronic Engineering*, 34(3-4), 321-339 (1997).
78. M. T. Gale, C. Gimkiewicz, S. Obi, M. Schnieper, J. Sochtig, H. Thiele and S. Westenhofer, "Replication technology for optical microsystems," *Optics And Lasers In Engineering*, 43(3-5), 373-386 (2005).
79. M. T. Gale, M. Rossi, H. Schutz, P. Ehbets, H. P. Herzig and D. Prongue, "Continuous-relief diffractive optical-elements for 2-dimensional array generation," *Applied Optics*, 32(14), 2526-2533 (1993).
80. M. B. Chan-Park and W. K. Neo, "Ultraviolet embossing for patterning high aspect ratio polymeric microstructures," *Microsystem Technologies*, 9(6), 501 (2003).
81. M. Watts, "Advances in roll to roll processing of optics," *PROC SPIE 6883*, 688305 (2008)..
83. Y. Toyoshima, I. Kawata, Y. Usami, Y. Mitsui, A. Sezginer, E. Maiken, K.-C. Chan, K. Johnson and D. Yonenaga, "Complementary use of scatterometry and SEM for photoresist profile and CD determination," *PROC SPIE 4689*, 196-205 (2002).
84. Seneca, *Seneca in Ten Volumes*, Harvard University Press, Cambridge, MA (1971)
85. J. N. Mait, "A history of imaging: Revisiting the past to chart the future," *Optics and Photonic News*, 22-27. (February 2006).
86. C. Evans, *Precision Engineering: an Evolutionary View*, Cranfield Press, Bedford, UK (1989).
87. S. P. Morgan, E. Choi, M. G. Somekh and C. W. See, "Interferometric optical microscopy of subwavelength grooves," *Optics Communications*, 187(1-3), 29-38 (2001).
88. M. Totzeck and H. J. Tiziani, "Interference microscopy of sub-lambda structures: A rigorous computation method and measurements," *Optics Communications*, 136(1-2), 61-74 (1997).

89. E. M. Slayter and H. S. Slayter, *Light and Electron Microscopy*, Cambridge University Press, Cambridge (1992).
90. S. Knight, R. Dixon, R. L. Jones, E. K. Lin, N. G. Orji, R. Silver, J. S. Villarrubia, A. E. Vladar and W.-l. Wu, "Advanced metrology needs for nanoelectronics lithography," *Ultimate lithography*, 7(8), 931 (2006).
91. T. R. Thomas, *Rough Surfaces*, Imperial Collage Press, London (1999).
92. J. C. Stover, *Optical Scattering: Measurement and Analysis*, SPIE, Bellingham, WA (1995).
93. C. J. Raymond, M. R. Murnane, S. S. H. Naqvi and J. R. McNeil, "Metrology Of Subwavelength Photoresist Gratings Using Optical Scatterometry," *Journal Of Vacuum Science & Technology B*, 13(4), 1484-1495 (1995).
94. R. L. Jones, T. Hu, E. K. Lin, W.-L. Wu, R. Kolb, D. M. Casa, P. J. Bolton and G. G. Barclay, "Small angle x-ray scattering for sub-100 nm pattern characterization," *Applied Physics Letters*, 83(19), 4059-4061 (2003).
95. T. J. Hu, R. L. Jones, W. L. Wu, E. K. Lin, Q. H. Lin, D. Keane, S. Weigand and J. Quintana, "Small angle x-ray scattering metrology for sidewall angle and cross section of nanometer scale line gratings," *Journal Of Applied Physics*, 96(4), 1983-1987 (2004).
96. R. L. Jones, W.-l. Wu, C.-q. Wang, E. K. Lin, K.-W. Choi, B. J. Rice, G. M. Thompson, S. J. Weigand and D. T. Keane, "Characterization of line edge roughness using CD SAXS," *PROC SPIE 6152*, 61520N (2006).
97. C. J. Raymond, M. E. Littau, A. Chuprin and S. Ward, "Comparison of solutions to the scatterometry inverse problem," *PROC SPIE 5375*, 564-575 (2004).
98. V. Machavariani, S. Garber and Y. Cohen, "Scatterometry: interpretation by different methods of electromagnetic simulation," *PROC SPIE 4689*, 177-188 (2002).
99. R. M. Peters, R. H. Chiao, T. Eckert, R. Labra, D. Nappa, S. Tang and J. Washington, "Production control of shallow trench isolation (STI) at the 130-nm node using spectroscopic ellipsometry-based profile metrology," *PROC SPIE 5375*, 798-806 (2004).

100. D. Herisson, D. Neira, C. Fernand, P. Thony, D. Henry, S. Kremer, M. Polli, M. Guevremont and A. Elazami, "Spectroscopic ellipsometry for lithography front-end level CD control: a complete analysis for production integration," PROC SPIE 5038, 264-273 (2003).
101. J. Huang, K. Barry, C.-M. Ke, B. Lin, A. Li, C. J. Raymond, M. E. Littau, T. Pitts and P. Nagy, "Application of 3D scatterometry to contacts and vias at 90nm and beyond," PROC SPIE 5752, 1266-1270 (2005).
102. L.-J. Chen, C.-M. Ke, S. S. Yu, T.-S. Gau, P.-H. Chen, Y. C. Ku, B. J. Lin, D. Engelhard, D. Hetzer, J. Y. Yang, K. A. Barry, L. Yap and W. Yang, "Application of scatterometry for CD and profile metrology in 193-nm lithography process development," PROC SPIE 5038, 568-576 (2003).
103. R. C.-J. Chen, F.-C. Chen, Y.-Y. Luo, B.-C. Perng, Y.-H. Chiu and H.-J. Tao, "Application of spectroscopic ellipsometry based scatterometry for ultra thin spacer structure," PROC SPIE 5375, 1374-1381 (2004).
104. V. A. Yakovlev, S. Bosch-Charpenay, P. A. Rosenthal, P. R. Solomon, J. Xu, J. C. Stover, M. J. Anc and M. L. Alles, "Characterization of Si-on-insulator buried layers by FTIR and scatterometry," PROC SPIE 4103, 90-97 (2000).
105. B. K. Minhas, S. A. Coulombe, S. S. H. Naqvi and J. R. McNeil, "Ellipsometric scatterometry for the metrology of sub-0.1- $\mu\text{m}$  -linewidth structures," Applied Optics, 37(22), 5112-5115 (1998).
106. M. E. Littau, C. J. Raymond, C. J. Gould and C. Gambill, "Novel implementations of scatterometry for lithography process control," PROC SPIE 4689, 506-516 (2002).
107. D. M. Shyu and M. H. Lu, "Overlay metrological system for overlaid linear gratings by an interferoscatterometer," Review Of Scientific Instruments, 76(8), 085103 (2005).
108. K. R. Lensing, C. Miller, G. Chudleigh, B. Swain, M. Laughery and A. Viswanathan, "Scatterometry feasibility studies for 0.13-micron flash memory lithography applications: enabling integrated metrology," PROC SPIE 5375, 307-316 (2004).
109. C. J. Raymond, M. E. Littau, R. J. Markle and M. A. Purdy, "Scatterometry for shallow trench isolation (STI) process metrology," PROC SPIE 4344, 716-725 (2001).

110. S. A. Coulombe, B. K. Minhas, C. J. Raymond, S. S. H. Naqvi and J. R. McNeil, "Scatterometry measurement of sub-0.1 micrometer linewidth gratings," *Journal Of Vacuum Science & Technology B*, 16(1), 80-87 (1998).
111. M. Sendelbach and C. N. Archie, "Scatterometry measurement precision and accuracy below 70 nm," *PROC SPIE 5038*, 224-238 (2003).
112. H.-T. Huang, G. Raghavendra, A. Sezginer, K. Johnson, F. E. Stanke, M. L. Zimmerman, C. Cheung, M. Miyagi and B. Singh, "Scatterometry-based overlay metrology," *PROC SPIE 5038*, 126-137 (2003).
113. T. Hingst, T. Marschner, M. Moert, J. Homilius, M. Guevremont, J. Hopkins and A. Elazami, "Spectroscopic Ellipsometry based Scatterometry enabling 193nm Litho and Etch process control for the 110nm technology node and beyond," *PROC SPIE 5038*, 274-285 (2003).
114. J.-a. Kim, S.-J. Kim, S.-B. Chin, S.-H. Oh, D.-H. Goo, S.-J. Lee, S.-G. Woo, H.-K. Cho, W.-S. Han, J.-T. Moon, C. J. Raymond, M. E. Littau, B. J. Youn and C.-J. Sohn, "Successful application of angular scatterometry to process control in sub-100-nm DRAM device," *PROC SPIE 5375*, 541-549 (2004).
115. M. S. Yeung and E. Barouch, "Electromagnetic scatterometry applied to in-situ metrology," *PROC SPIE 4344*, 484-495 (2001).
116. E. Barouch and S. L. Knodle, "Scatterometry as a practical in-situ metrology technology," *PROC SPIE 5038*, 559-567 (2003).
117. P. Thony, D. Herisson and D. Henry, "Evaluation of scatterometry tools for integrated metrology," at SEMI session on Integrated Metrology, München (2003).
118. *International Technology Roadmap for Semiconductors: Metrology*, (2007)
119. M. Born and E. Wolf, *Principles of Optics: Electromagnetic Theory of Propagation, Interference and Diffraction of Light* Cambridge University Press, New York (1999).
120. E. L. Church, "The measurement of surface texture and topography by differential light scattering," *Wear*, 57(1), 93-105 (1979).

121. E. L. Church and J. M. Zavada, "Residual surface roughness of diamond-turned optics," *Appl. Opt.*, 14, 1788-1795 (1975).
122. H. E. Bennett and J. O. Porteus, "Relation Between Surface Roughness and Specular Reflectance at Normal Incidence," *J. Opt. Soc. Am.*, 51, 123-129 (1961).
123. R. Schiffer, "Reflectivity of a slightly rough surface," *Applied Optics*, 26(4), 704-711 (1987).
124. S. S. H. Naqvi, S. Gaspar, K. Hickman, K. Bishop and J. R. McNeil, "Linewidth Measurement Of Gratings On Photomasks - A Simple Technique," *Applied Optics*, 31(10), 1377-1384 (1992).
125. J. Wolberg, *Data Analysis Using the Method of Least Squares*, Springer, Berlin (2006).
126. B. N. Taylor, C. E. Kuyatt and T. National Institute of Standards and, *Guidelines for Evaluating and Expressing the Uncertainty of NIST Measurement Results*, US Dept. of Commerce, Technology Administration, National Institute of Standards and Technology, (1994).
127. J. Wolberg, *Prediction Analysis*, D. Van Nostrand Company, Princeton (1967).
128. A. Yamaguchi, K. Ichinose, S. Shimamoto, H. Fukuda, R. Tsuchiya, K. Ohnishi, H. Kawada and T. Iizumi, "Metrology of LER: influence of line-edge roughness (LER) on transistor performance," *PROC SPIE 5375*, 468 (2004).
129. W. Bogaerts, P. Bienstman and R. Baets, "Scattering at sidewall roughness in photonic crystal slabs," *Optics Letters*, 28(9), 689-691 (2003).
130. S. G. Johnson, M. I. Povinelli, M. Soljacic, A. Karalis, S. Jacobs and J. D. Joannopoulos, "Roughness losses and volume-current methods in photonic-crystal waveguides," *Applied Physics B-Lasers And Optics*, 81(2-3), 283-293 (2005).
131. J. Yang, F. Shanhui and D. A. B. Miller, "Systematic photonic crystal device design: global and local optimization and sensitivity analysis," *IEEE Journal of Quantum Electronics*, 42(3), 266 (2006).

132. S. Mookherjea and A. Oh, "Effect of disorder on slow light velocity in optical slow-wave structures," *Opt. Lett.*, 32, 289-291 (2007).
133. V. Constantoudis, G. P. Patsis, L. H. A. Leunissen and E. Gogolides, "Toward a complete description of linewidth roughness: a comparison of different methods for vertical and spatial LER and LWR analysis and CD variation," *PROC SPIE 5375*, 967 (2004).
134. V. Constantoudis, G. P. Patsis, L. H. A. Leunissen and E. Gogolides, "Line edge roughness and critical dimension variation: Fractal characterization and comparison using model functions," *Journal of Vacuum Science & Technology B: Microelectronics and Nanometer Structures*, 22, 1974 (2004).
135. V. Constantoudis, E. Gogolides, G. P. Patsis, A. Tserepi and E. S. Valamontes, "Characterization and simulation of surface and line-edge roughness in photoresists," *Journal of Vacuum Science & Technology B: Microelectronics and Nanometer Structures*, 19, 2694 (2001).
136. G. M. Gallatin, "Resist blur and line edge roughness (Invited Paper)," *PROC SPIE SPIE 5754*, 38 (2005).
137. Y. Zhao, G.-C. Wang and T.-M. Lu, *Characterization of amorphous and crystalline rough surfaces: Principles and applications*, Academic Press, San Diego (2001).
138. V. Constantoudis, G. Kokkoris, P. Xydi, E. Gogolides, E. Pargon and M. Martin, "Line edge roughness transfer during plasma etching: modeling approaches and comparison with experimental results," *PROC SPIE 7273*, 72732J (2009).
139. D. Whitehouse, *Surfaces and Their Measurement*, Kogan Page Science, London (2002).
140. T. Y. Lee, D. Ihm, H. C. Kang, J. B. Lee, B. H. Lee, S. B. Chin, D. H. Cho and C. L. Song, "Experimental study of contact edge roughness on sub-100 nm various circular shapes," *PROC SPIE 5752*, 516-526 (2005).
141. G. W. Reynolds and J. W. Taylor, "Factors contributing to sidewall roughness in a positive-tone, chemically amplified resist exposed by x-ray lithography," *Journal of Vacuum Science & Technology B: Microelectronics and Nanometer Structures*, 17, 334 (1999).

142. M. Yoshizawa and S. Moriya, "Study of the acid-diffusion effect on line edge roughness using the edge roughness evaluation method," *Journal Of Vacuum Science & Technology B*, 20(4), 1342-1347 (2002).
143. M. I. Sanchez, W. D. Hinsberg, F. A. Houle, J. A. Hoffnagle, H. Ito and C. V. Nguyen, "Aerial image contrast using interferometric lithography: effect on line-edge roughness," *PROC 3678*, 160 (1999).
144. Personal Communications with G. M. Gallatin, San Jose, CA (2009).
145. D. L. Goldfarb, A. P. Mahorowala, G. M. Gallatin, K. E. Petrillo, K. Temple, M. Angelopoulos, S. Rasgon, H. H. Sawin, S. D. Allen and M. C. Lawson, "Effect of thin-film imaging on line edge roughness transfer to underlayers during etch processes," *Journal of Vacuum Science & Technology B: Microelectronics and Nanometer Structures*, 22, 647 (2004).
146. Y. Martin and H. K. Wickramasinghe, "Method for imaging sidewalls by atomic force microscopy," *Applied Physics Letters*, 64(19), 2498-2500 (1994).
147. S. E. Fuller and M. Young, "Photomask-edge-roughness characterization using an atomic force microscope," *PROC SPIE 3332*, 433-440 (1998).
148. A. Nikitin, A. Sicignano, D. Yerebin, M. Sandy and T. Goldburt, "Critical issues in quantifying line edge roughness," *PROC SPIE 5752*, 1098-1106 (2005).
149. C. Nelson, S. C. Palmateer, A. R. Forte and T. M. Lyszczarz, "Comparison of metrology methods for quantifying the line edge roughness of patterned features," *Journal of Vacuum Science & Technology B: Microelectronics and Nanometer Structures*, 17(6), 2488-2498 (1999).
150. C. M. Nelson-Thomas, S. C. Palmateer and T. M. Lyszczarz, "Metrology methods for the quantification of edge roughness," *PROC SPIE 3332*, 19-29 (1998).
151. M. N.-T. Carla, C. P. Susan, R. F. Anthony, G. C. Susan, S. Deneault and M. L. Theodore, "Metrology methods for quantifying edge roughness: II," *PROC SPIE 3677*, 53-61 (1999).

152. A. G. Bony, A. Heid, Y. Takakura, K. Satzke and P. Meyrueis, "Waveguide sidewall roughness estimation via shape-from-shading surface reconstruction of SEM pictures," *PROC SPIE 5355*, 103-110 (2004).
153. G. W. Reynolds and J. W. Taylor, "Correlation of atomic force microscopy sidewall roughness measurements with scanning electron microscopy line-edge roughness measurements on chemically amplified resists exposed by x-ray lithography," *Journal of Vacuum Science & Technology B: Microelectronics and Nanometer Structures*, 17, 2723 (1999).
154. N. G. Orji, T. V. Vorburger, J. Fu, R. G. Dixson, C. V. Nguyen and J. Raja, "Line edge roughness metrology using atomic force microscopes," *Measurement Science and Technology*, 16(11), 2147-2154 (2005).
155. P. Boher, J. Petit, T. Leroux, J. Foucher, Y. Desieres, J. Hazart and P. Chaton, "Optical Fourier transform scatterometry for LER and LWR metrology," *PROC SPIE 5752*, 192-203 (2005).
156. J. Bischoff, E. Drege and S. Yedur, "Edge roughness measurement in optical metrology", *USPTO 7,046,375 B2* (2006).
157. T. A. Germer, "Effect of line and trench profile variation on specular and diffuse reflectance from a periodic structure," *J. Opt. Soc. Am. A* 24(3), 696-701 (2007).
158. B. Bunday, "Line edge roughness characterization of sub-50nm structures using CD-SAXS: Round-robin benchmark results," *PROC SPIE 6518*, 65181O (2007).
159. R. L. Jones, T. Hu, C. L. Soles, E. K. Lin, W.-l. Wu, D. M. Casa and A. Mahorowala, "Preliminary evaluation of line-edge roughness metrology based on CD-SAXS," *PROC SPIE 5375*, 191-198 (2004).
160. E. K. Lin, W. Wu, Q. Lin and M. Angelopoulos, "Feature-shape and line-edge roughness measurement of deep submicron lithographic structures using small-angle neutron scattering," *PROC SPIE 4344*, 414 (2001).
161. R. Silver, T. Germer, R. Attota, B. M. Barnes, B. Bunday, J. Allgair, E. Marx and J. Jun, "Fundamental limits of optical critical dimension metrology: a simulation study," *PROC SPIE 6518*, 65180U (2007).

162. F. Scholze, C. Laubis, U. Dersch, J. Pomplun, S. Burger and F. Schmidt, "The influence of line edge roughness and CD uniformity on EUV scatterometry for CD characterization of EUV masks," *PROC SPIE* 6617, 66171 (2007).
163. B. Brill, "Optical measurements of line edge roughness", USPTO 7,184,152 (2007).
164. J. K. Bhardwaj and H. Ashraf, "Advanced silicon etching using high-density plasmas," *PROC SPIE* 2639, 224-233 (1995).
165. S. G. Johnson, M. L. Povinelli, P. Bienstman, M. Skorobogatiy, M. Soljacic, M. Ibanescu, E. Lidorikis and J. D. Joannopoulos, "Coupling, scattering, and perturbation theory: Semi-analytical analyses of photonic-crystal waveguides," *IEEE Proceedings of 5th International Conference on Transparent Optical Networks* (2003).
166. T. G. Makay, "Homogenization of linear and nonlinear complex composite materials," in *Introduction to complex mediums for optics and electromagnetics*, W. S. Weiglhofer, and A. Lakhakia, eds., SPIE Press, Bellingham, WA (2003).
167. M. Nevière and E. Popov, "Grating Electromagnetic Theory User Guide," *The Journal of Imaging Science and Technology*, 41(4), 315 (1997).
168. R. C. Rumpf, *Design and optimization of nano-optical elements by coupling fabrication to optical behavior*, Ph.D. Thesis, University of Central Florida (2006).
169. K. S. Kunz and R. J. Luebbers, *The finite difference time domain method for electromagnetics*, CRC Press, Boca Raton, FL (1993).
170. A. Taflove and S. C. Hagness, *Computational electrodynamics: The finite-difference time-domain method*, Artech House Norwood, MA, (1995).
171. M. M. Jiang, T. Tamir and S. Z. Zhang, "Modal theory of diffraction by multilayered gratings containing dielectric and metallic components," *J. Opt. Soc. Am. A-Opt. Image Sci. Vis.*, 19(8), 1722-1722 (2002).
172. L. F. Li, "Multilayer Modal Method for Diffraction Gratings of Arbitrary Profile, Depth, and Permittivity," *J. Opt. Soc. Am. A-Opt. Image Sci. Vis.*, 11(5), 1685-1685 (1994).

173. L. F. Li, "New formulation of the Fourier modal method for crossed surface-relief gratings," *J. Opt. Soc. Am. A-Opt. Image Sci. Vis.*, 14(10), 2758-2767 (1997).
174. C. H. Lin, K. M. Leung and T. Tamir, "Modal transmission-line theory of three-dimensional periodic structures with arbitrary lattice configurations," *J. Opt. Soc. Am. A-Opt. Image Sci. Vis.*, 19(10), 2005-2017 (2002).
175. Z. Y. Li and L. L. Lin, "Photonic band structures solved by a plane-wave-based transfer-matrix method," *Physical Review E*, 67(4), 46607 (2003).
176. L. C. Botten, T. P. White, A. A. Asatryan, T. N. Langtry, C. M. de Sterke and R. C. McPhedran, "Bloch mode scattering matrix methods for modeling extended photonic crystal structures. I. Theory," *Physical Review E*, 70(5), (2004).
177. N. P. K. Cotter, T. W. Preist and J. R. Sambles, "Scattering-Matrix Approach To Multilayer Diffraction," *J. Opt. Soc. Am. A-Opt. Image Sci. Vis.*, 12(5), 1097-1103 (1995).
178. S. F. Mingaleev and K. Busch, "Scattering matrix approach to large-scale photonic crystal circuits," *Optics Letters*, 28(8), 619-621 (2003).
179. T. P. White, L. C. Botten, C. M. de Sterke, R. C. McPhedran, A. A. Asatryan and T. N. Langtry, "Bloch mode scattering matrix methods for modeling extended photonic crystal structures. II. Applications," *Physical Review E*, 70(5), (2004).
180. D. M. Whittaker and I. S. Culshaw, "Scattering-matrix treatment of patterned multilayer photonic structures," *Physical Review B*, 60(4), 2610-2618 (1999).
181. M. G. Moharam and T. K. Gaylord, "Rigorous Coupled-Wave Theory Of Planar Gratings," *Journal Of The Optical Society Of America*, 70(12), 1631-1632 (1980).
182. M. G. Moharam and T. K. Gaylord, "Rigorous Coupled-Wave Analysis Of Planar-Grating Diffraction," *Journal Of The Optical Society Of America*, 71(7), 811-818 (1981).
183. M. G. Moharam, E. B. Grann, D. A. Pommet and T. K. Gaylord, "Formulation For Stable And Efficient Implementation Of The Rigorous Coupled-Wave Analysis Of Binary Gratings," *J. Opt. Soc. Am. A-Opt. Image Sci. Vis.*, 12(5), 1068-1076 (1995).

184. M. G. Moharam, D. A. Pommet, E. B. Grann and T. K. Gaylord, "Stable Implementation Of The Rigorous Coupled-Wave Analysis For Surface-Relief Gratings - Enhanced Transmittance Matrix Approach," J. Opt. Soc. Am. A-Opt. Image Sci. Vis., 12(5), 1077-1086 (1995).
185. P. Lalanne and G. M. Morris, "Highly improved convergence of the coupled-wave method for TM polarization," J. Opt. Soc. Am. A-Opt. Image Sci. Vis., 13(4), 779-784 (1996).
186. S. Johnson and J. Joannopoulos, "Block-iterative frequency-domain methods for Maxwell's equations in a planewave basis" Opt. Express, 8, 173-190 (2001).
187. S. Guo and S. Albin, "Simple plane wave implementation for photonic crystal calculations," Optics Express, 11(2), 167-175 (2003).
188. J. D. Jackson, *Classical Electrodynamics*, John Wiley & Sons, New York (1962).
189. G. Strang, *Linear Algebra and its Applications*, Harcourt, Fort Worth, TX (1988).
190. L. Rayleigh, "On the Dynamical Theory of Gratings," Proc. R. Soc. London Ser. A, 79(532), 399-416 (1907).
191. P. Yeh, A. Yariv and C. S. Hong, "Electromagnetic propagation in periodic stratified media. I. General theory," J. Opt. Soc. Am, 67(4), 423-438 (1977).
192. E. Hecht, *Optics*, Pearson-Addison-Wesley, San Francisco (2002).
193. M. Neviere and E. Popov, *Light Propagation in Periodic Media*, New York (2003).
194. L. Li, "Use of Fourier series in the analysis of discontinuous periodic structures " J. Opt. Soc. Am. A, 13(1870- (1996).
195. T. A. Germer, "SCATMECH: Polarized Light Scattering C++ Class Library," Available at <http://physics.nist.gov/scatmech>. (2009).
196. E. J. Hinch, *Perturbation Methods*, Cambridge University Press, New York (1991).

197. S. G. Johnson, M. Ibanescu, M. A. Skorobogatiy, O. Weisberg, J. D. Joannopoulos and Y. Fink, "Perturbation theory for Maxwell's equations with shifting material boundaries," *Phys. Rev. E*, 65(6), 066611 (2002).
198. L. F. Li, "Use of Fourier series in the analysis of discontinuous periodic structures," *J. Opt. Soc. Am. A-Opt. Image Sci. Vis.*, 13(9), 1870-1876 (1996).
199. J. C. Maxwell Garnett, "Colours in Metal Glasses, in Metallic Films and in Metallic Solutions," *Philos. Trans. Royal Soc A*, 203, 385-420 (1904).
200. J. C. Maxwell Garnett, "Colours in Metal Glasses, in Metallic Films and in Metallic Solutions.. II," *Proceedings of the Royal Society of London. Series A*, 205, 237-288 (1906).
201. A. Yariv and P. Yeh, "Electromagnetic propagation in periodic stratified media. II. Birefringence, phase matching, and x-ray lasers," *J. Opt. Soc. Am.*, 67(4), 438-448 (1976).
202. S. M. Rytov, "Electromagnetic properties of a finely stratified medium", *Sov. Phys. JETP*, 2 (3), 466-475 (1956)
203. T. C. Choy, *Effective Medium Theory: Principles and Applications*, Clarendon Press, Oxford (1999).
204. D. A. G. Bruggeman, "Berechnung verschiedener physikalischer Konstanten von heterogenen Substanzen. I. Dielektrizitätskonstanten und Leitfähigkeiten der Mischkörper aus isotropen Substanzen," *Annalen der Physik*, 416(7), 636-664 (1935).
205. H. G. Tomkins, *A User's Guide to Ellipsometry*, Academic Press, (1993).
206. A. Sihvola, P. Ylä-Oijala, S. Järvenpää and J. Avelin, "Polarizabilities of platonic solids," *IEEE Transactions on Antennas and Propagation*, 52(9), 2226-2233 (2004).
207. J. Avelin, R. Sharma, I. Hanninen and A. H. Sihvola, "Polarizability analysis of cubical and square-shaped dielectric scatterers," *IEEE Transactions on Antennas and Propagation*, 49(3), 451 (2001).

208. A. Sihvola, "Dielectric polarization and particle shape effects" *Journal of Nanomaterials*, Article ID 45090 (2007).
209. L. Rayleigh, "On the incidence of aerial and electric waves upon small obstacles in the form of ellipsoids or elliptic cylinders, and on the passage of electric waves through a circular aperture in a conducting screen," *Philosophical Magazine*, 44, 28-52 (1897).
210. H. C. van de Hulst, *Light Scattering by Small Particles*, John Wiley & Sons, New York (1957).
211. D. Stroud, "Generalized effective-medium approach to the conductivity of an inhomogeneous material," *Physical Review B*, 12(8), 3368-3373 (1975).
212. J. Thiault, J. Foucher, J. H. Tortai, O. Joubert, S. Landis and S. Pauliac, "Line edge roughness characterization with a three-dimensional atomic force microscope: Transfer during gate patterning processes," *Journal of Vacuum Science & Technology B: Microelectronics and Nanometer Structures*, 23, 3075 (2005).
213. G. P. Patsis, V. Constantoudis, A. Tserepi, E. Gogolides and G. Grozev, "Quantification of line-edge roughness of photoresists. I. A comparison between off-line and on-line analysis of top-down scanning electron microscopy images," *Journal of Vacuum Science & Technology B: Microelectronics and Nanometer Structures*, 21, 1008 (2003).
214. V. Constantoudis, G. P. Patsis, A. Tserepi and E. Gogolides, "Quantification of line-edge roughness of photoresists. II. Scaling and fractal analysis and the best roughness descriptors," *Journal of Vacuum Science & Technology B: Microelectronics and Nanometer Structures*, 21, 1019 (2003).
215. D. E. Aspnes, J. B. Theeten and F. Hottier, "Investigation of effective-medium models of microscopic surface roughness by spectroscopic ellipsometry," *Physical Review B*, 20(8), 3292-3302 (1979).
216. M. Foldyna, A. De Martino, R. Ossikovski, E. Garcia-Caurel and C. Licitra, "Characterization of grating structures by Mueller polarimetry in presence of strong depolarization due to finite spot size," *Optics Communications*, 282(5), 735-741 (2009).
217. M. Foldyna, E. Garcia-Caurel, R. Ossikovski, A. De Martino and J. J. Gil, "Retrieval of a non-depolarizing component of experimentally determined depolarizing Mueller matrices," *Optics Express*, 17(15), 12794-12806 (2009).

218. M. Ercken, L. H. A. Leunissen, I. Pollentier, G. P. Patsis, V. Constantoudis and E. Gogolides, "Effects of different processing conditions on line-edge roughness for 193-nm and 157-nm resists," *PROC SPIE* 5375, 266–275 (2004).
219. C. Wang, R. L. Jones, E. K. Lin, W. Wu, J. S. Villarrubia, K. W. Choi, J. S. Clarke, B. J. Rice, M. J. Leeson and J. Roberts, "Line edge roughness characterization of sub-50nm structures using CD-SAXS: round-robin benchmark results," *PROC SPIE* 6518, 65181O (2007).
220. T. A. Germer and C. C. Asmail, "Goniometric optical scatter instrument for out-of-plane ellipsometry measurements," *Review of Scientific Instruments*, 70(9), 3688-3695 (1999).
221. S. Cho, S. Yedur, M. Kwon and M. Tabet, "CD and profile metrology of EUV masks using scatterometry based optical digital profilometry," *PROC SPIE* 6349, 63492I (2006).
222. R. M. A. Azzam and N. M. Bashara, "Polarization Characteristics Of Scattered Radiation From A Diffraction Grating By Ellipsometry With Application To Surface-Roughness," *Physical Review B*, 5(12), 4721 (1972).
223. M. Galli, D. Bajoni, M. Belotti, F. Paleari, M. Patrini, G. Guizzetti, D. Gerace, A. Agio, L. C. Andreani, D. Peyrade and Y. Chen, "Measurement of photonic mode dispersion and linewidths in silicon-on-insulator photonic crystal slabs," *IEEE Journal On Selected Areas In Communications*, 23(7), 1402-1410 (2005).
224. A. Shinya, M. Notomi, I. Yokohama, C. Takahashi, J.-I. Takahashi and T. Tamamura, "Two-dimensional Si photonic crystals on oxide using SOI substrate" *Optical and Quantum Electronics*, 34, 113-121 (2002).
225. A. Hessel and A. A. Oliner, "A new theory of Wood's anomalies on optical gratings," *Appl. Opt.*, 4(10), 1275 (1965).
226. V. N. Astratov, M. S. Skolnick, S. Brand, T. F. Krauss, O. Z. Karimov, R. M. Stevenson, D. M. Whittaker, I. Culshaw and R. M. De la Rue, "Experimental technique to determine the band structure of two-dimensional photonic lattices," *IEEE Proc.-Optoelectron.*, 145(6), 398-402 (1998).
227. M. Galli, M. Agio, L. C. Andreani, M. Belotti, G. Guizzetti, F. Marabelli, M. Patrini, P. Bettotti, L. Dal Negro, Z. Gaburro, L. Pavesi, A. Liu and P. Bellutti,

"Spectroscopy of photonic bands in macroporous silicon photonic crystals," *Physical Review B*, 65(11), (2002).

228. M. Ahles, T. Ruhl, G. P. Hellmann, H. Winkler, R. Schmechel and H. von Seggern, "Spectroscopic ellipsometry on opaline photonic crystals," *Optics Communications*, 246(1-3), 1-7 (2005).

229. K. W. K. Shung and Y. C. Tsai, "Surface Effects And Band Measurements In Photonic Crystals," *Physical Review B*, 48(15), 11265-11269 (1993).

230. I. Emanuel and H. S. Edward, "Measurement of the phase shift upon reflection from photonic crystals," *Applied Physics Letters*, 86(15), 151112 (2005).

231. C. C. Barcenas and P. M. Griffin, "Parametric-Based Determination of Cylindrical Variations in Geometric Tolerancing," *J. Manuf. Sci. Eng.* , 122, 549-555 (2000).

## APPENDIX A: OPTICAL SCATTEROMETRY INSTRUMENTS

## A1. Goniometric Optical Scattering Instrument (GOSI)

Fixed wavelength angle resolved measurements of the artifacts were taken using the Goniometric Optical Scattering Instrument (GOSI) at National Institute of Standards and Technology (NIST)<sup>220</sup>. A schematic diagram of the entire system is shown in Figure 23.

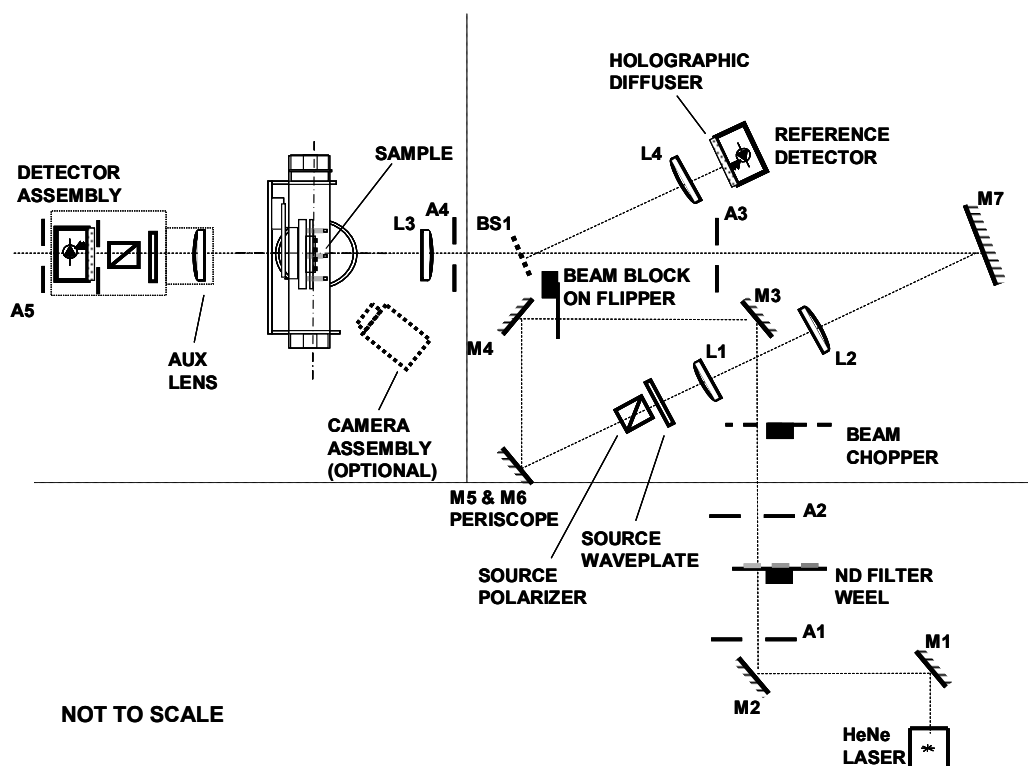


Figure 23. Schematic layout for the Goniometric Optical Scattering Instrument (GOSI)

GOSI is a general purpose instrument for studying both specular and diffuse optical scattering from surfaces at various angles of incidence and azimuthal orientations. It has provision for inserting polarization optics both before and after the samples so that it can be used to perform generalized Stokes polarimetry. The source is configured so that it can be easily interchanged by redirecting the beam path using auxiliary mirrors. For

these experiments, a 35 mW helium-neon (HeNe) LASER operating at a wavelength of 632.8 nm was used as the source. The source was aligned to the existing system by using mirrors M1 and M2 (Figure 23) through apertures A1 and A2. Apertures A3 and A5 fixed during the initial setup of the instrument and are used to ensure that the beam path is aligned approximately to the center of rotation of the goniometer. A set of neutral density (ND) filters was placed on a filter wheel after the LASER so that the intensity could be adjusted to not saturate the detectors during measurements, but to allow for optimal contrast during alignment. A beam chopper was used to modulate the source beam so that the signals from the detectors could be synchronized using lock-in amplifiers after being electronically filtered to remove high frequency noise. After passing through a shutter, the beam is directed through a series of turning mirrors to a set of polarization optics. Typically, LASER sources have a preferred polarization direction. However, the Glan-Thomson polarizer is used to ensure that the polarization extinction ratio is at least 100,000:1 and that the polarization has a fixed orientation with respect to the rest of the system. Depending on the type of polarization measurement being taken, either a half-wave plate or quarter wave plate can be inserted after the source polarizer in order to control the incident polarization. For these experiments, only a half-wave plate was used so the orientation of the incident polarization could be changed, but not the ellipticity. After the polarization optics, a beam expander (L1 and L2) is used to expand the beam in order to more easily control the numerical aperture of the incident beam using aperture A4 and lens L3. A beam splitter (BS1) is used to “pick off” a portion of the beams energy to be collected by lens L4 and focused onto the reference detector. Holographic diffusers are placed in front of both the reference and signal detectors in

order to minimize interference effects that may be caused by a cover glass over the detector. The incident beam is focused onto the sample using L3. The focal length of L3 and the size of aperture A4 were chosen to minimize the numerical aperture of the incident beam while still ensuring that the beam did not significantly overfill the sample area. A detector assembly is located at the end of an arm attached to the third rotary table. It consists of an optional auxiliary lens (AUX LENS), a wave plate and polarizer (similar to the ones used in the source path), a holographic diffuser, an aperture, and the detector. The aperture acts as the field stop for the system. The polarizer and waveplate act to select the polarization state of the detected signal. For these experiments a half-wave plate was used so the linear orientation of the polarization could be selected, but information about the phase difference between two orthogonal polarizations is lost.

The sample is held in place with vacuum on a fixture placed in the center of the goniometer. The goniometer consists of a rotary stage (used to adjust the sample azimuthal angle) fixed to two linear stages that are used to position the sample in the incident beam. This entire assembly rests on a second rotary table that is used to set the incident angle. A third rotary table, used to position the detector, is mounted coaxially to the second rotary table.

## A2. Nanometrics Atlas Scatterometer Platform

The Nanometrics Atlas scatterometer platform<sup>221</sup> contains a normal incidence spectroscopic reflectometer and a fixed angle J.A. Woollam M-88 spectroscopic ellipsometer with integrated wafer handling and pattern positioning hardware and software (Figure 24). The ellipsometer has a sixty-five degree fixed angle of incidence in a rotating analyzer configuration. In order to make rapid measurements, broad band

illumination is used and the spectrum is analyzed with a grating spectrometer and linear array detector. The ellipsometer illuminates the sample with an elliptical spot that is 40 micrometers along the major axis, while the reflectometer measures a 25 micrometer circular spot.

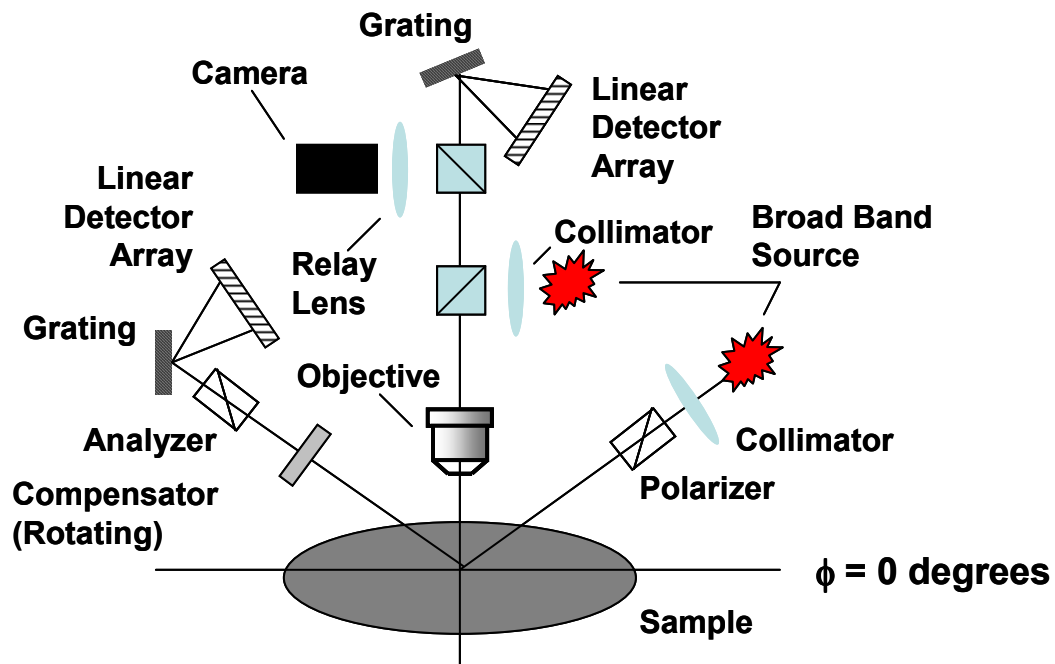


Figure 24 Conceptual schematic of Nanometrics ATLAS scatterometer

The reflectometer records the normal incidence reflectivity of the sample for two orthogonal linear incident polarizations. For the reflectometer, the polarization labeled ‘TE’ is polarized with the electric field normal to the plane of incidence of the ellipsometer while the polarization labeled TM is polarized with the electric field in the plane of incidence of the ellipsometer.

## APPENDIX B: MEASUREMENT OF NOMINAL GRATING PARAMETERS

The angle resolved reflectance data for the grating on the five lobe chip that was fabricated without intentional edge roughness is described in Appendix C. The polarization dependent reflectance of the sample is described by a reflection matrix<sup>222</sup>

$$R = \begin{bmatrix} R_{pp} & R_{ps} \\ R_{sp} & R_{ss} \end{bmatrix} \quad (\text{B.1})$$

where  $R_{ss}$  is the ratio of the reflected intensity of the s-polarized light to the incident intensity of the s-polarized light,  $R_{sp}$  is the ratio of the reflected intensity of the s-polarized light to the incident intensity of the p-polarized light,  $R_{ps}$  is the ratio of the reflected intensity of the p-polarized light to the incident intensity of the s-polarized light and  $R_{pp}$  is the ratio of the reflected intensity of the p-polarized light to the incident intensity of the p-polarized light. The plane of incidence is a plane defined by the surface normal and the incident wave vector. The s-polarization (from senkrecht, a German word meaning perpendicular) has an electric field vector perpendicular to the plane of incidence, while the p-polarization (from the German word for parallel, simply parallel) has an electric field vector completely in the plane of incidence. Since preliminary measurements confirmed that the coupling between orthogonal linear incident polarizations was less than  $1:10^4$ , only the diagonal terms of the matrix ( $R_{ss}$  and  $R_{pp}$ ) were considered.

This data was fit to a grating model using a one dimensionally periodic RCWA algorithm to determine the nominal parameters for the grating used in this study. The

gratings were designed to have a period of 736 nm, a depth of 500 nm, a line width of 368 nm, and vertical sidewalls (Figure 25).

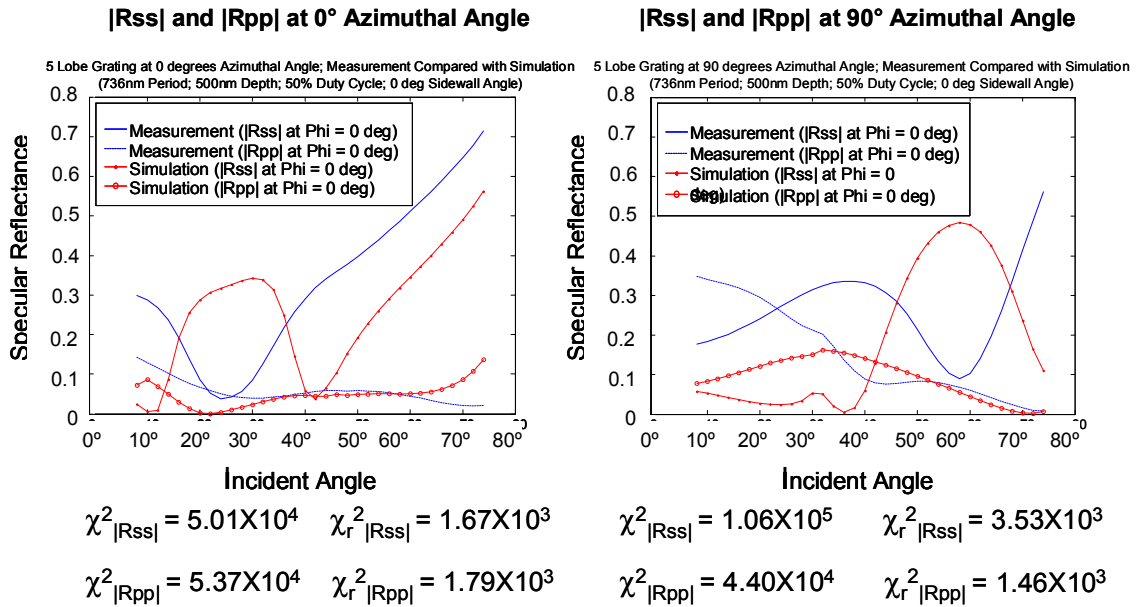


Figure 25. Comparison of measured signal and signal from a model of grating as designed.

Although some of the major features of the measured signal and the modeled signal appear in roughly the same angular position, as indicated by the very large chi square values, the curves are not close at all. The next step in the fitting process is to generate a library of curves having parameters that deviate systematically from the expected parameters and compare the measured curves to each of the library curves. A map of the chi squared value of the fit between the measured curves and the library curves is shown in Figure 26. It is clear that depth and duty cycle (line width) are coupled strongly.

This map indicates that there is significant correlation between the changes in the signal caused by depth variations and changes in the signal caused by variations in the width of the line.

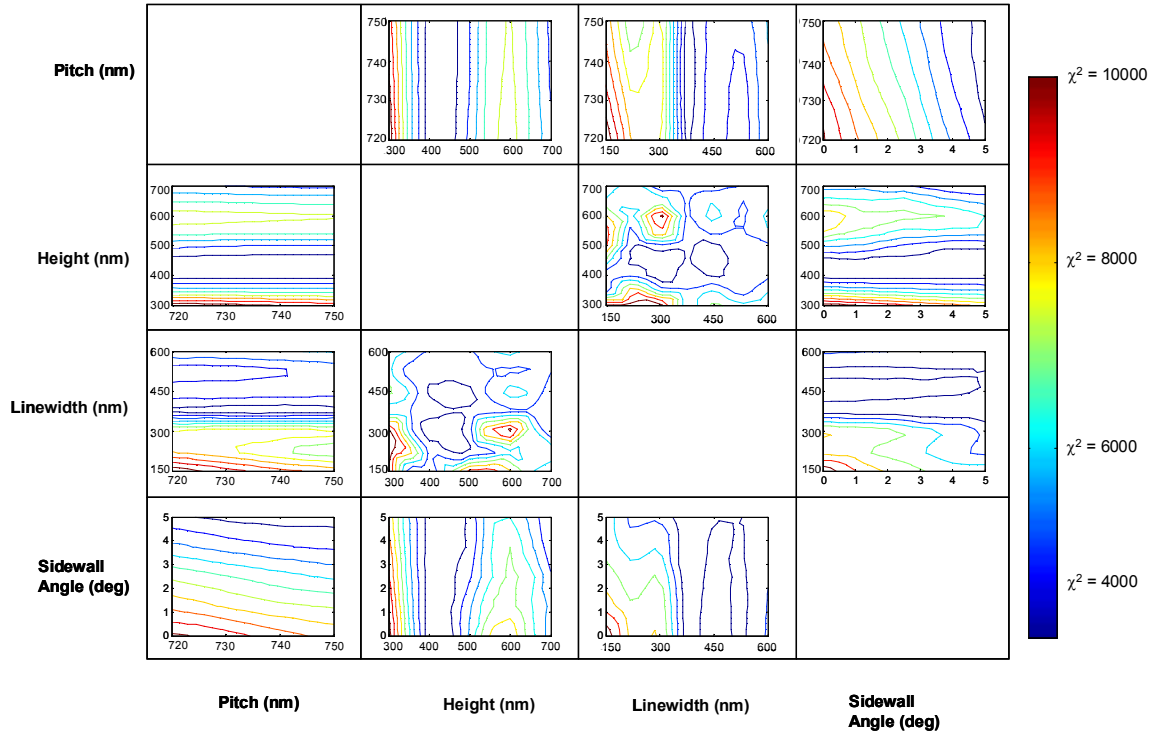


Figure 26. Sensitivity of chi squared fit to variation in model parameters for 0 deg azimuthal angle demonstrating coupling between factors (Averaged over other two parameters) It is clear that depth and duty cycle (line width) are coupled strongly.

Figure 27 shows the comparison between the measured signal and the best fit signal from the library search. This signal was obtained for a grating with a 736 nm period, a 375 nm depth, a 294 nm line width, and vertical sidewalls. As indicated by the chi squared values, the fit is much better, but still larger than would be desired for a reasonable uncertainty in the fit parameters.

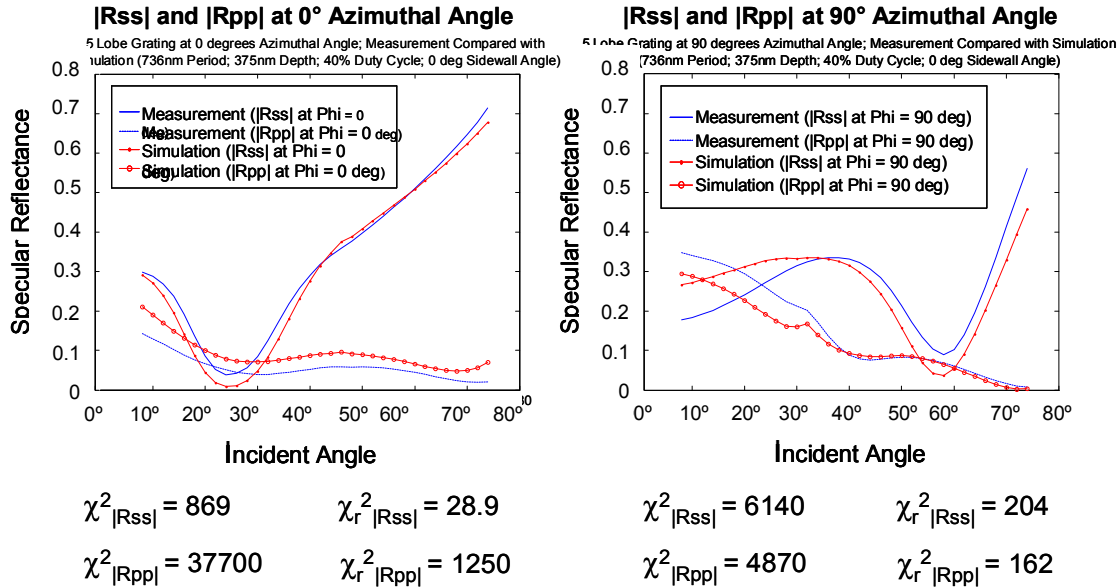


Figure 27. Comparison of measured signal and the best fit model from the library search

One possible method for improving the fit is to fix parameters that can be determined by other means. For example, the pitch of the grating can be determined by measuring the angle between the position when the normally incident beam is reflected back into the aperture and the Littrow position (Figure 28). The first order Littrow position is the position of the grating when the first diffraction order diffracts back along the incident beam such that  $\theta_i = -\theta_d = \theta$  in equation (2.1). If the stage errors are small, then the uncertainty in determining  $\theta$  (in radians) is approximately  $(2/d)u_\delta$ , where  $u_\delta$  is the uncertainty in determining when the centroid of the return spot is aligned with the aperture. Once this angle is determined, the pitch of the grating can be calculated from equation (2.1). Due to the relatively long distance ( $d$ ) between aperture A4 and the sample as depicted in Figure 23, the angle, and therefore the pitch of the grating, can be determined with a very small uncertainty. Using this method, the pitch of the grating was determined to be 735.75 +/- 1.3 nm ( $1\sigma$ ).

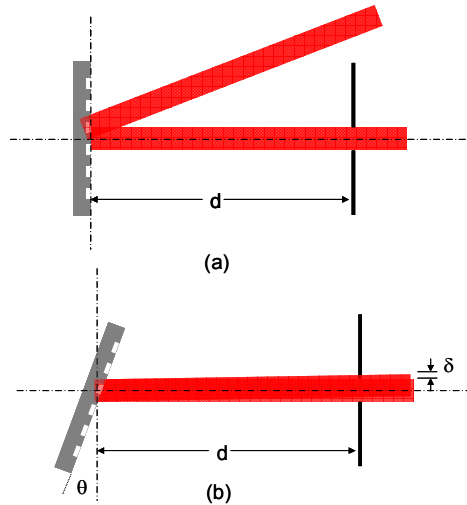


Figure 28. The pitch of the grating can be determined by measuring the angle between the position (a) when the face of the grating is normal to the optic axis and (b) the Littrow position.

With this new value for the period of the grating, the other model parameters were fit to the measured data using a non-linear least squares fit. The results are shown in Figure 29.

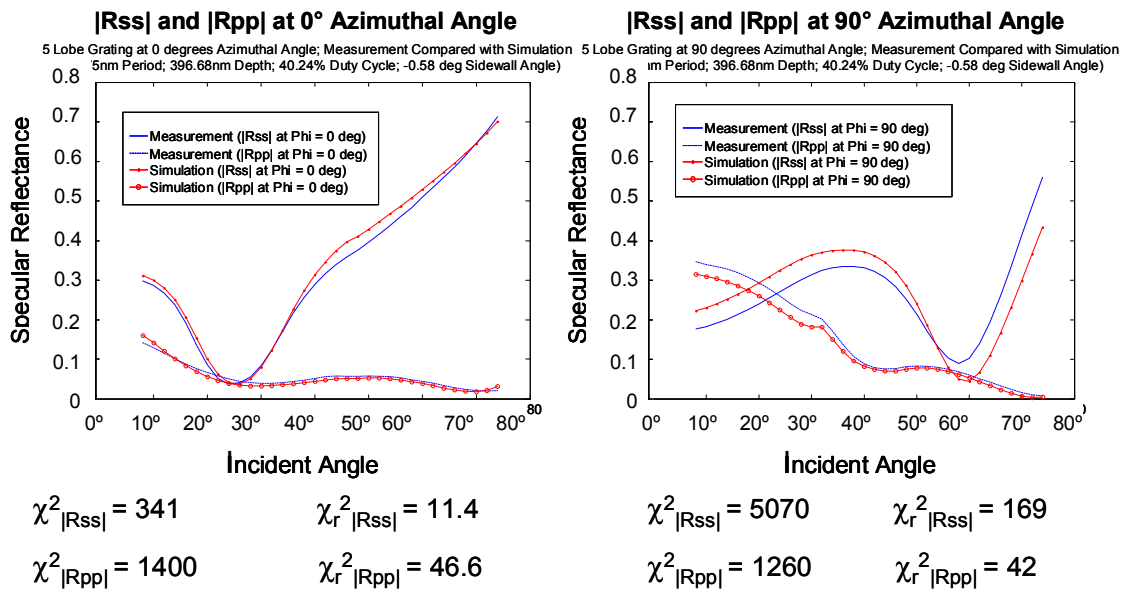


Figure 29. Comparison of the measured signal to the signal from the model with the period determined experimentally and the other parameters determined using a non-linear least squares fit.

The reduced chi squared values are still significantly larger than one. This indicates that there is significant bias in the measured data or that the model is does not contain enough parameters. These are common problems for optical scatterometry measurements. The biased estimate of the grating parameters are summarized in Table 1. The grating period was measured as using the previously described method with an independently estimated uncertainty. However, the uncertainties in the other parameters must be determined from the model fit (as described in section 2.2). Since a significant bias is suspected, it is meaningless to assign uncertainties to these values.

Table 1 Nominal grating parameters used in the models

<i>Grating Period:</i>	735.75 nm +/- 2.6 nm ( $2\sigma$ )
<i>Grating Depth:</i>	396.68 nm
<i>Line Width:</i>	296.06 nm
<i>Sidewall Angle 1:</i>	0 deg
<i>Sidewall Angle 2 :</i>	0 deg

## APPENDIX C: ROUGHNESS ARTIFACT

In order to experimentally examine the effects of edge roughness on scatterometry signals, a set of artifacts was created in silicon with e-beam lithography, using a Raith 150 e-beam lithography system<sup>70</sup>, and reactive ion etching using an STS Silicon Fast Etcher<sup>164</sup>.

Originally, the set of artifacts fabricated on silicon were to be used to develop the fabrication process and an additional set of artifacts was to be created in silicon over an oxide cladding layer using silicon on insulator (SOI) wafers. However, the process that was developed for etching the silicon wafer did not yield acceptable results for the SOI wafers. The artifacts fabricated using the SOI substrate should have aided in confining the field in the direction normal to the substrate surface.<sup>71,223,224</sup> This should have made it possible to resolve the resonant anomalies of the periodic structures<sup>225</sup>, so that the spectral data could have been directly related to the band diagrams for the structures.<sup>223, 226-230</sup> However, the broad spectra from the angle resolved scattering measurements of the silicon artifacts also exhibited sensitivity to the edge roughness. These are the spectra that are compared in Appendix D.

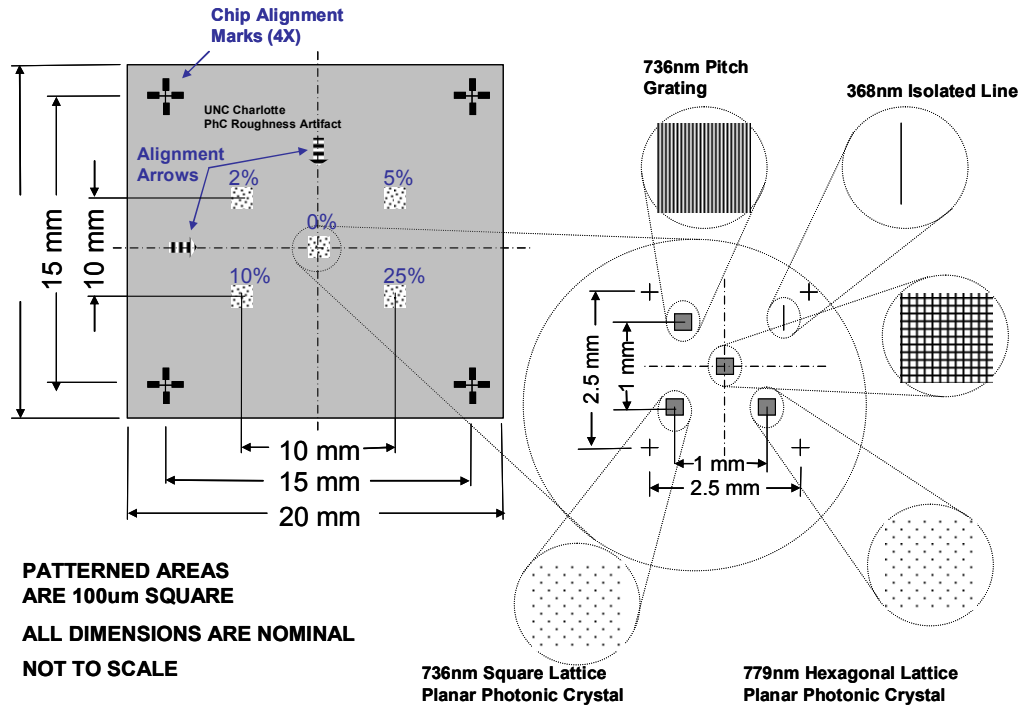


Figure 30 Illustration of the layout of one chip in the artifact set.

The set of artifacts contains four *chips*. Each *chip* consists of five *groups* of four one-hundred micrometer by one-hundred micrometer square pattern *areas*: a 736 nm pitch grating, a 300 nm wide isolated line, a square lattice of 406 nm holes with a 736 nm lattice spacing, and a 776 nm hexagonal lattice of 410 nm holes with a 770 nm lattice spacing (Figure 30 and Figure 31). Each group within a chip is associated with a different level of edge roughness. The central set in each chip is fabricated without any intentional edge roughness. The other groups were fabricated to have intentional peak-to-valley edge roughness that is 2%, 5%, 10%, or 25% of the nominal radius of the hole or half width of the line.

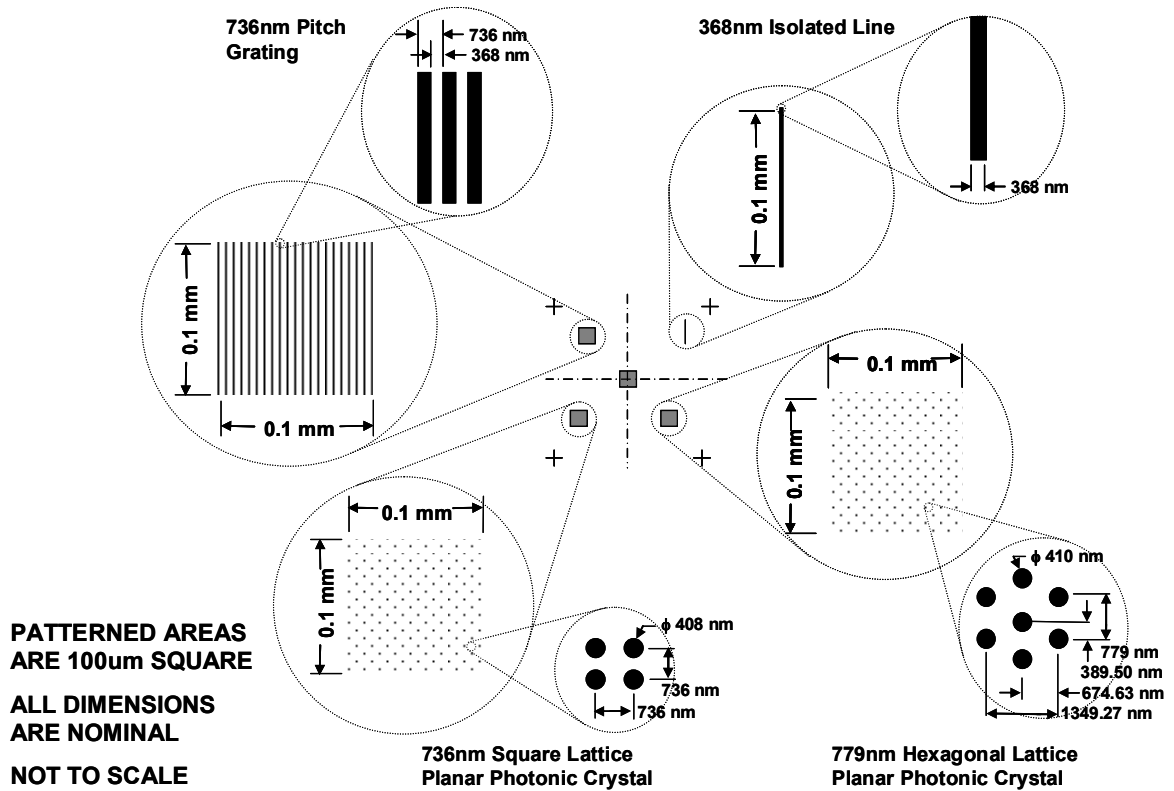


Figure 31 Detail of the nominal patterns within each group.

Lobe structures were used to simulate the edge roughness in a systematic manner. This is similar to the manner used to describe cylindricity in traditional machine tool metrology<sup>139,231</sup>. The profiles of the circular features were defined by the parametric equations.

$$\begin{aligned}
 U(\theta) &= \left(\frac{D}{2}\right) \cos(\theta) (\rho \sin(n\theta + 2\pi\phi) + 1) \\
 V(\theta) &= \left(\frac{D}{2}\right) \sin(\theta) (\rho \sin(n\theta + 2\pi\phi) + 1)
 \end{aligned}
 \tag{C.1}$$

where  $(U(\theta), V(\theta))$  describes the Cartesian coordinates of the edge with respect to the center of the feature,  $D$  is the nominal diameter of the feature,  $\rho$  is the peak to valley roughness,  $n$  is an integer defining the rotational symmetry of the deviations (i.e. the number of lobes),  $\phi$  is a phase factor describing the orientation of the deviations, and  $\theta$

varies from zero to  $2\pi$ . For the linear grating structures, the periods of the deviations of the edges of the lines were defined as if the lobe structures were unwrapped along the edges of the lines.

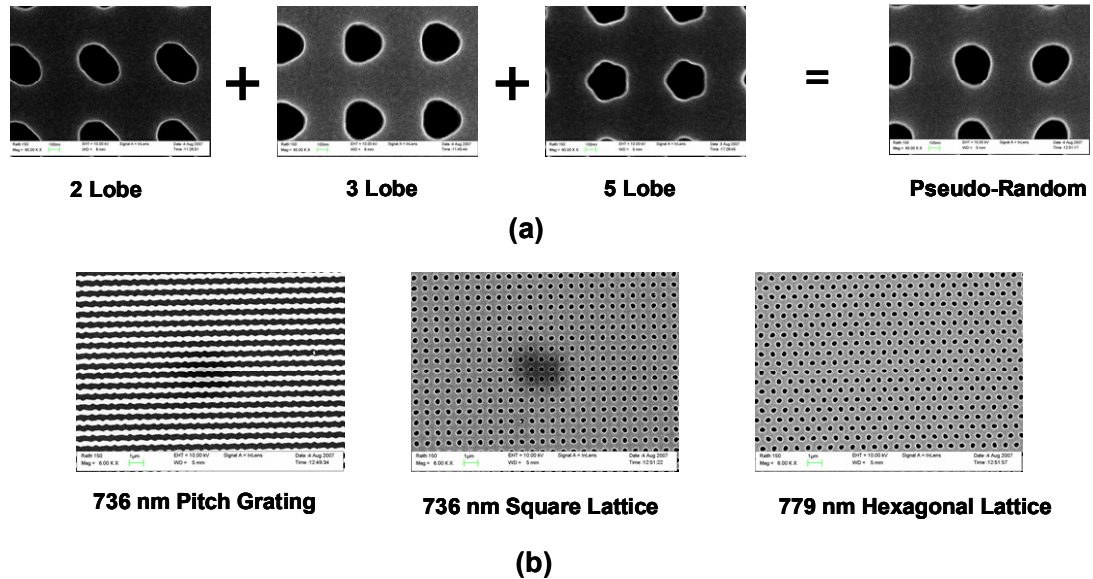


Figure 32. Scanning Electron Micrographs (a) illustrating how two-lobe, three-lobe, and five-lobe roughness was combined to simulate random roughness and (b) examples of random roughness super-cells for linear gratings, square lattice photonic crystals, and hexagonal lattice photonic crystals

Three different chips were fabricated with two, three, and five lobes in order to represent the three lowest order, independent lobe structures. A fourth chip with twenty-one lobes was attempted in order to directly simulate the higher frequency roughness. However, this structure proved to be beyond the resolution of the fabrication process. A fifth chip was created with pseudo-random edge roughness. The pseudo-random edge roughness was created by combining the deviations from the two-lobe, three-lobe, and five-lobe roughness (Figure 32). The three different roughness components were combined with exponential weighting (with the two lobe component having a peak to

valley deviation equal to the stated roughness and the five lobe component having a relative weight of  $\frac{1}{e^2}$ ) and random phase relationships between the three components for each feature within a ten by ten period super-cell. SEM images of the patterns are shown in Figure 33 through Figure 35.

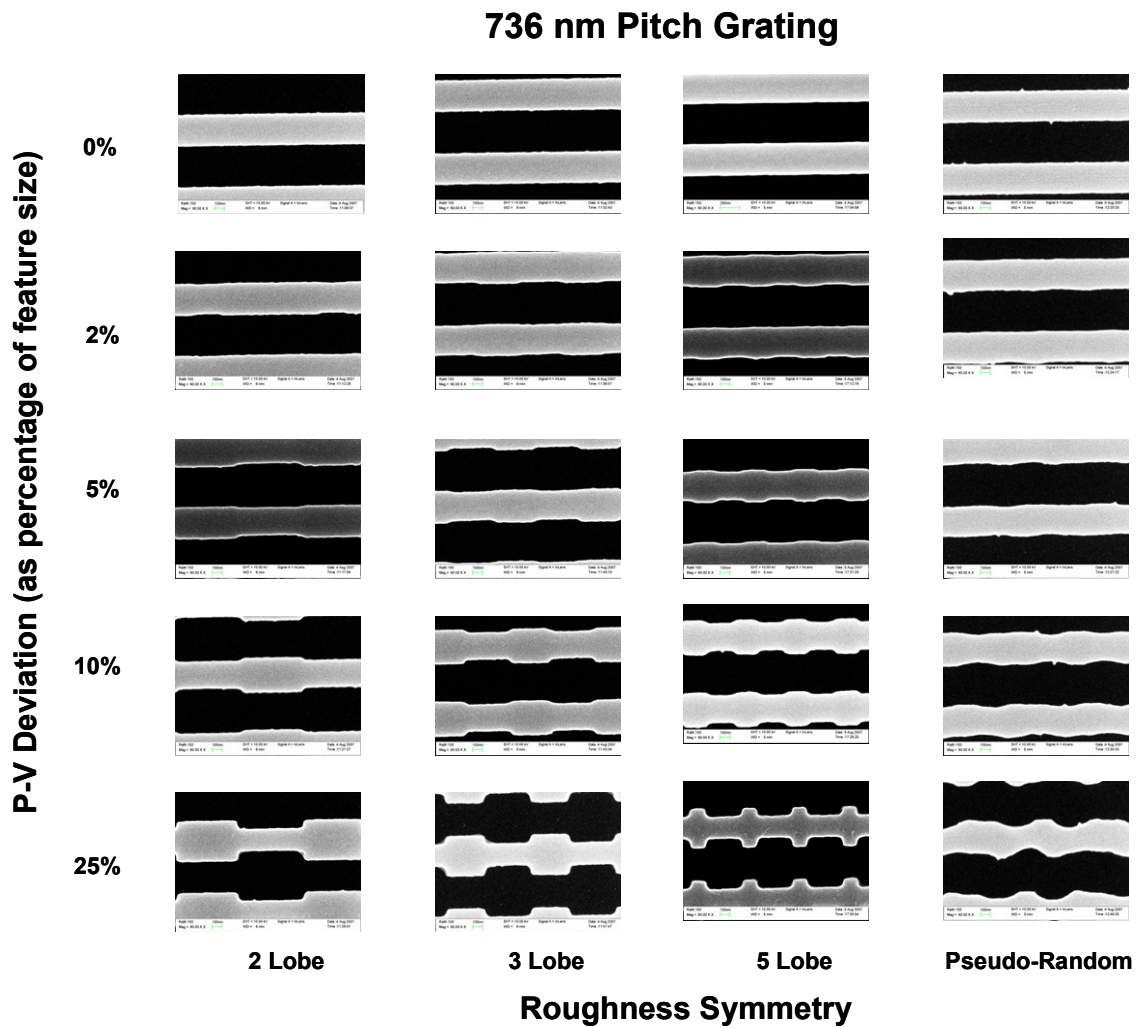


Figure 33 SEM images of the linear gratings fabricated on the roughness artifacts.

### 736 nm Pitch Square Lattice Photonic Crystal

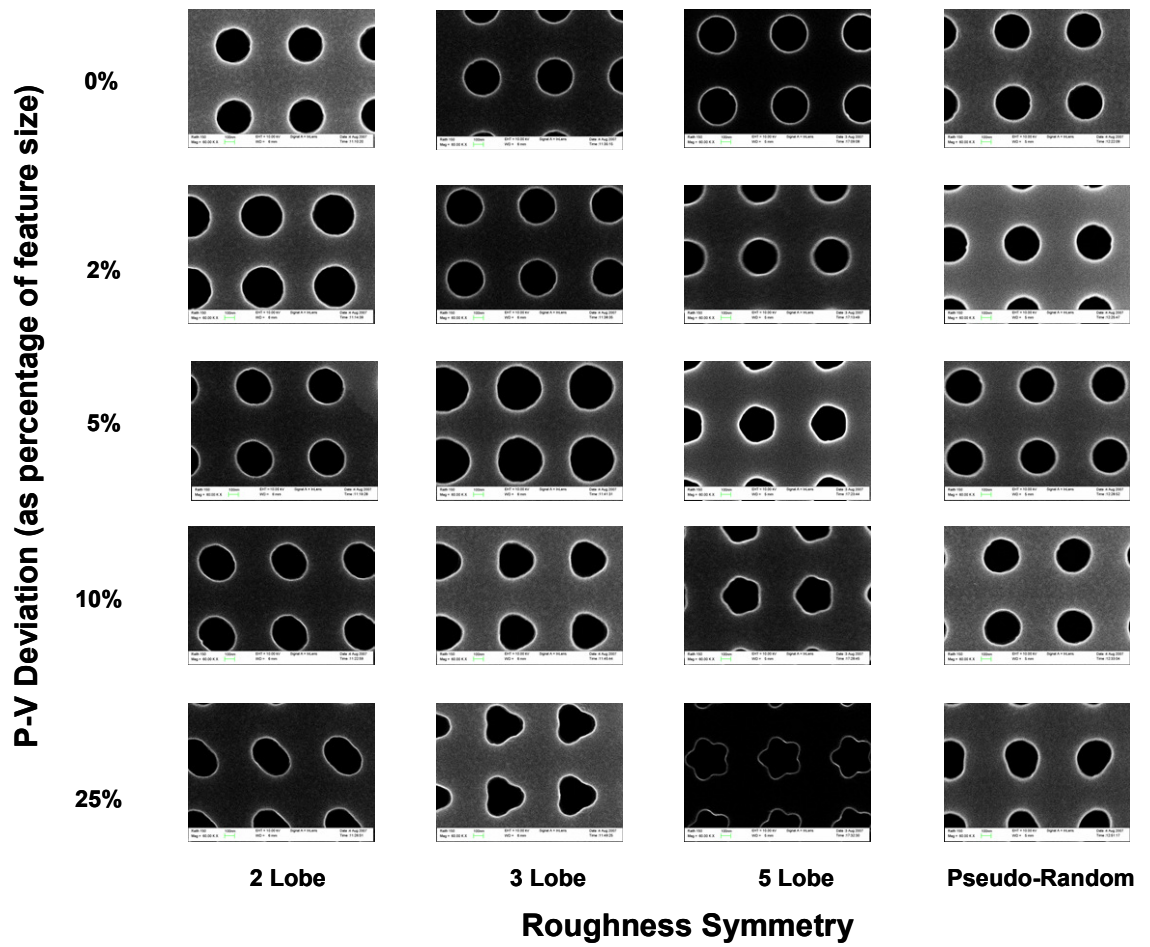


Figure 34 SEM images of the square lattice photonic crystal structure fabricated on the roughness artifacts.

### 736 nm Pitch Hexagonal Lattice Photonic Crystal

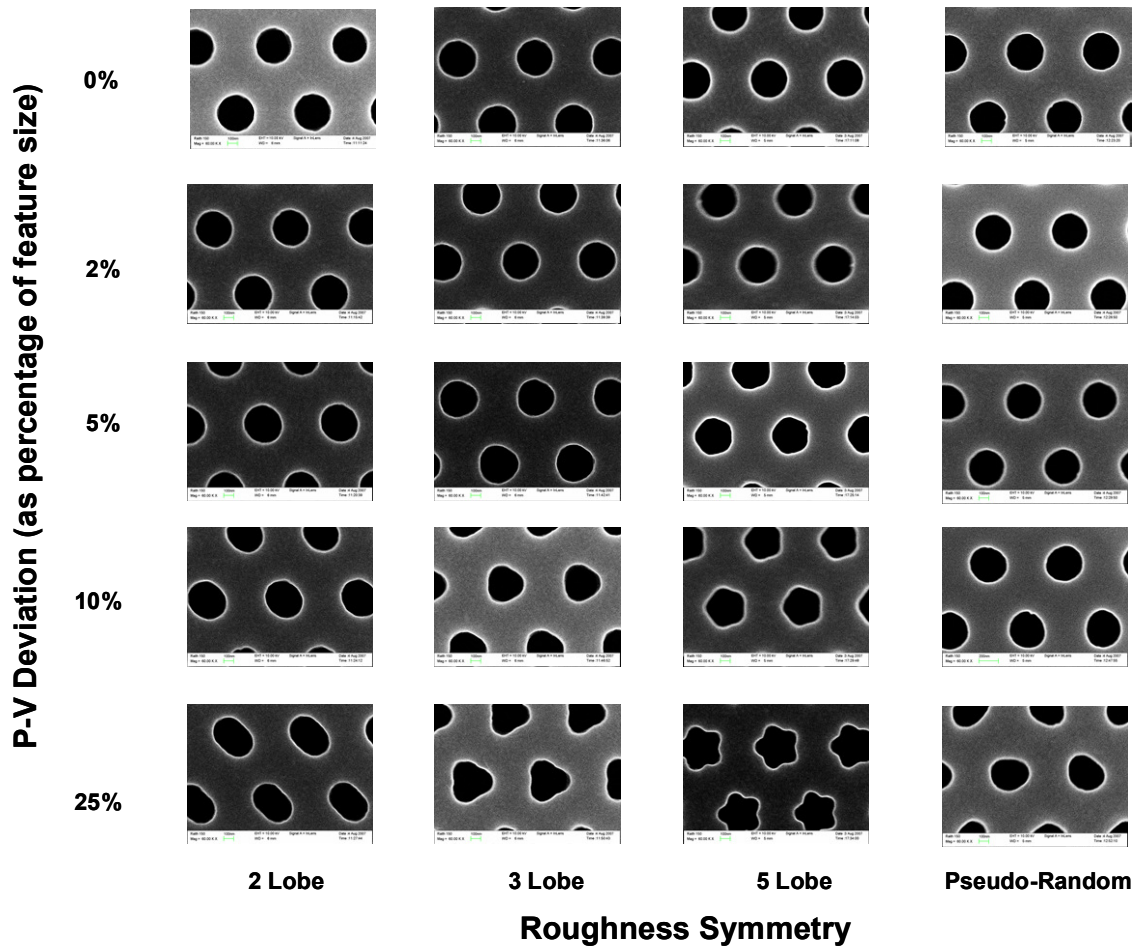


Figure 35 SEM images of the hexagonal lattice photonic crystal structure fabricated on the roughness artifacts.

## APPENDIX D: EXPERIMENTAL DATA FROM ROUGH GRATINGS

Fixed wavelength, angle resolved scattering measurements were taken using the Goniometric Optical Scattering Instrument (GOSI)<sup>220</sup> at the National Institute of Standards and Technology (NIST). Fixed angle spectroscopic ellipsometry measurements were taken using the Nanometric Atlas scatterometry system<sup>221</sup>.

Fixed wavelength, angle resolved measurements were taken of each grating on the roughness artifacts. The results are shown in Figure 36. It is difficult to make any quantitative comparison since there is known bias in the measurements as indicated by the poor chi square fits in Appendix B. This bias is likely due to misalignment of the grating region with the incident beam, additional signal from the region around the grating because the incident spot overfilled the grating region and misalignments of the detector as it was rotated. However, the relative position of peaks within the spectra gives a clear indication that the edge roughness has an effect on the scatterometry signal. Similar measurements were made using the normal incidence spectroscopic reflectometer and fixed angle spectroscopic ellipsometer of the Nanometrics ATLAS scatterometry system (Figure 37 and Figure 38). As with the angle resolved data, features in the spectra tend to become less distinct as the rms value of the roughness is increased. However, for the random roughness case new features begin to appear in the spectra at large values of rms roughness. This is an interesting result that should be examined in detail in future work.

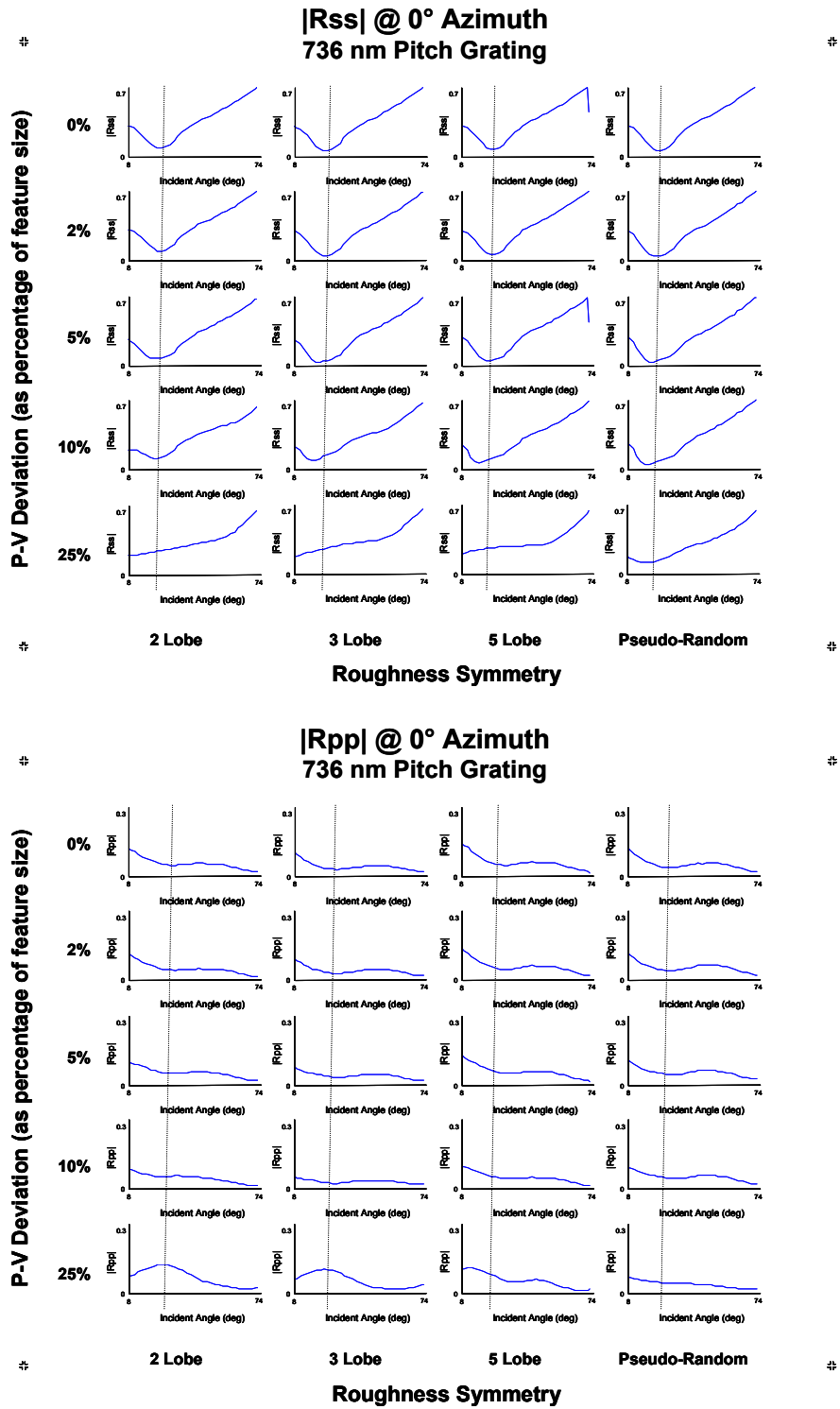


Figure 36 Fixed wavelength (632.8 nm) angle resolved data from gratings with intentional edge roughness. The dashed lines indicate spectral features that change with rms roughness amplitude.

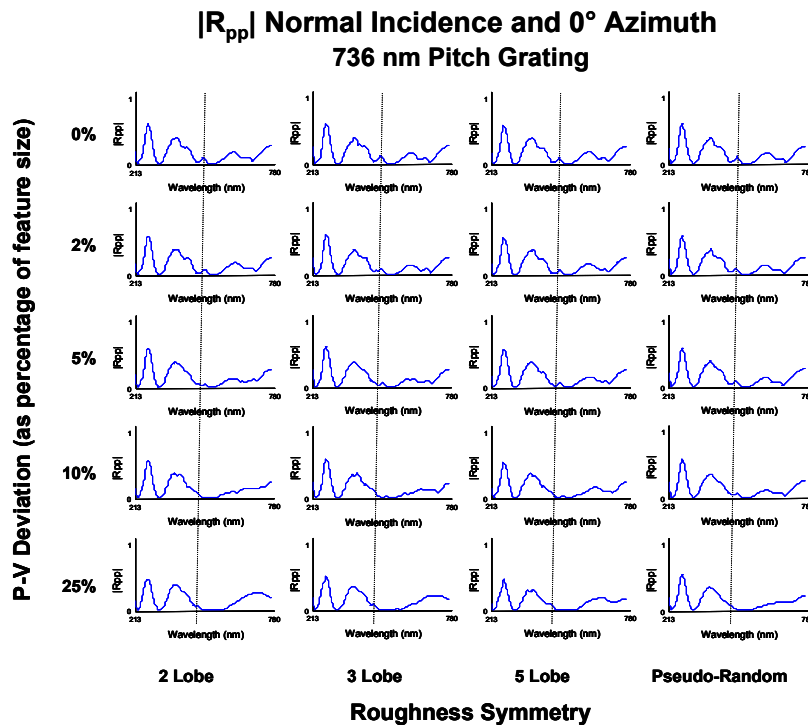
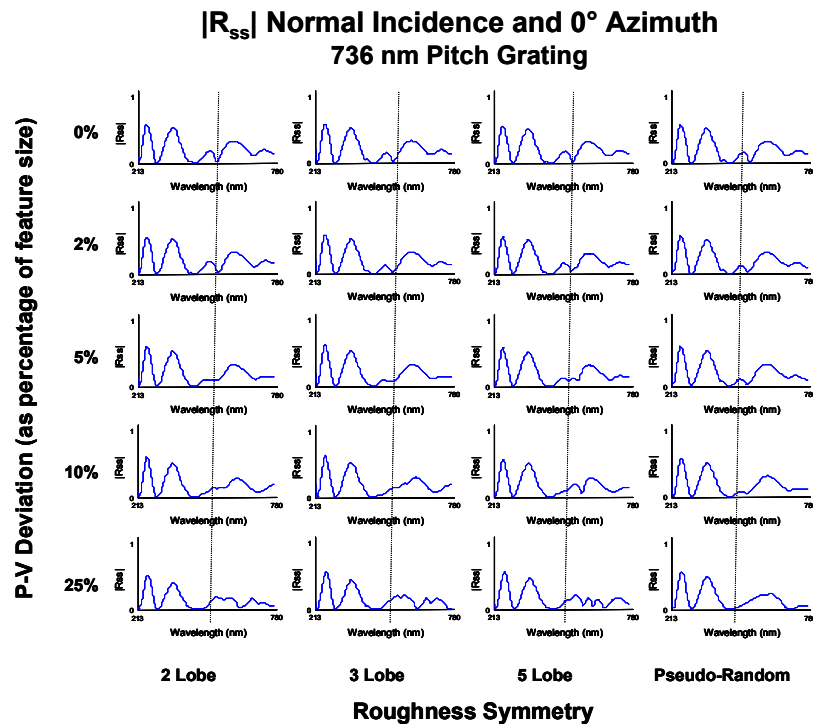


Figure 37 Normal incidence spectroscopic reflectometry data (taken over a spectral range from 213 nm to 780 nm) from gratings with intentional edge roughness. The dashed lines indicate spectral features that change with rms roughness amplitude.

**Psi @ 65° Incidence and 0° Azimuth**  
**736 nm Pitch Grating**

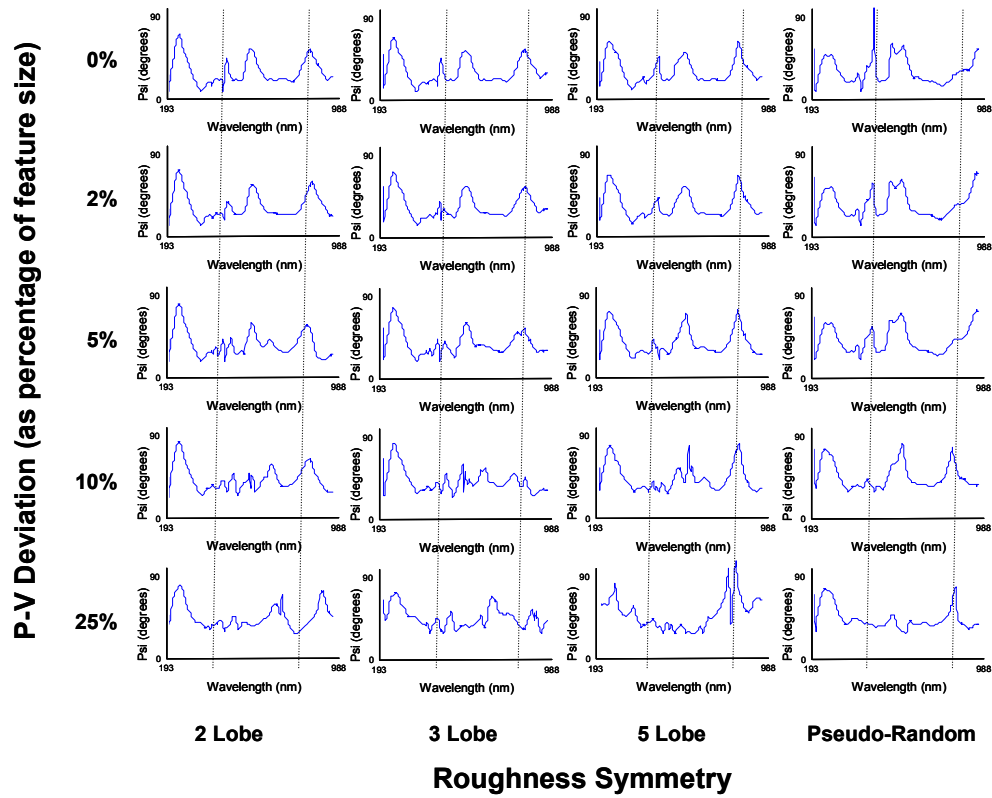


Figure 38 65 degree fixed incident angle spectroscopic ellipsometry data (taken over a spectral range from 198nm to 980 nm) from gratings with intentional edge roughness. The dashed lines indicate spectral features that change with rms roughness amplitude

## APPENDIX E: SCATMECH MODELS

In chapter 4, scatterometry signatures from a randomly rough periodic grating were calculated using a 2D RCWA algorithm and compared with the results from a 1D RCWA model that replaced the roughness by an effective medium layer. The RCWA algorithms used were as described by Moharam *et al.*<sup>183,184</sup> with a modification proposed by Lelanne and Morris<sup>185</sup> and Li<sup>194</sup> and extended to two dimensionally periodic structures by Li<sup>173</sup>. The software that was used for the 1D RCWA simulations is available online<sup>195</sup> while the software used for the 2D RCWA simulations will be made available to the general public in a future release of the software. The software is controlled using scripts written using the Model Integrated Scatter Tool (MIST)<sup>195</sup>. This Appendix includes examples of the script files used to generate the data in chapter 4.

For the 2D RCWA simulations the CrossRCW\_BRDF\_Model was used:

```

; RCW solution for crossed gratings
MODEL = CrossRCW_BRDF_Model

VARIABLES:
  pi = 4*atan(1)
  deg = pi/180

  halfangle = 0.01 ; Half angle over which BRDF is spread for a delta-function
  detector = pi*halfangle^2 ; The solid angle collected by the detector
  thetai = 80 ; Incident Angle in degrees
  inpol = 45 ; 0 for s, 90 for p

  period = 0.2 ; Period of the grating
  depth = 0.2 ; Depth of the grating
  duty_cycle = 0.5 ; Fraction of period filled with grating medium
  sidewall_angle = 0 ; Sidewall Angle in degrees
  wavelength = 0.6328 ; Wavelength of the light in vacuum

  iteration = 1 ; counting variable for multiple realizations
  rms_roughness = 0.0025 ; rms deviation of the edge from nominal
  roughness_period = 0.2 ; period of pattern repeat along the transverse direction
  clength = 0.020 ; correlation length of the roughness
  exponent = 0.2 ; roughness (Hurst) exponent
  mode = 1 ; LER = 1 and LWR = 0

  sample_rotation = 0 ; Rotation angle of sample in degrees
  n = 0 ; Diffraction order
  k.x = sind(thetai)+n*wavelength/period*cosd(sample_rotation) ; Diffraction equation for x
  k.y = n*wavelength/period*sind(sample_rotation) ; Diffraction equation for y
  phis = atan2d(k.y,k.x) ; Azimuthal angle of diffraction
  thetas = thetai
  #quiet = 1

  minsamples = 1
  differential = (2*deg)^2
  incidentangle = thetai*deg
  incidentpol = (1,cos(2*inpol*deg),sin(2*inpol*deg),0)
  rotation = sample_rotation*deg

; Wavelength [um] <double>
lambda = wavelength
#lambda = lambda

; Substrate <dielectric_function>
$substrate = silicon

type = 0 ; (0) for Reflection or (1) for Transmission <int>
#type = type

; Half angle of detector [rad] <double>
alpha = halfangle
#alpha = alpha

```

```

; RCW Simulator <CrossRCW_Model_Ptr>
$RCW = CrossRCW_Model

; Incident angle [deg] <double>
RCW.thetai = thetai
#RCW.thetai = RCW.thetai

; Rotation angle of sample [deg] <double>
RCW.rotation = rotation
#RCW.rotation = RCW.rotation

; Wavelength [um] <double>
RCW.lambda = wavelength
#RCW.lambda = RCW.lambda

; Grating <CrossGrating_Ptr>
$RCW.grating = Random_Wiggle_CrossGrating

; Fourier order in direction #1 <int>
RCW.grating.order1 = 10
#RCW.grating.order1 = RCW.grating.order1

; Fourier order in direction #2 <int>
RCW.grating.order2 = 20
#RCW.grating.order2 = RCW.grating.order2

; Angle of lattice vectors from perpendicular [deg] <double>
RCW.grating.zeta = 0.
#RCW.grating.zeta = RCW.grating.zeta

; Lattice constant #1 [um] <double>
RCW.grating.d1 = period
#RCW.grating.d1 = RCW.grating.d1

; Lattice constant #2 [um] <double>
RCW.grating.d2 = roughness_period
#RCW.grating.d2 = RCW.grating.d2

; Number of sampling points in direction #1 <int>
RCW.grating.grid1 = 2048
#RCW.grating.grid1 = RCW.grating.grid1

; Number of sampling points in direction #2 <int>
RCW.grating.grid2 = 2048
#RCW.grating.grid2 = RCW.grating.grid2

; Incident medium <dielectric_function>
RCW.grating.medium_i = (1,0)
#RCW.grating.medium_i = RCW.grating.medium_i

; Transmitted medium <dielectric_function>
$RCW.grating.medium_t = silicon

; Grating <Grating_Ptr>
$RCW.grating.grating = Single_Line_Grating

```

```

; Period of the grating [um] <double>
RCW.grating.grating.period = period
#RCW.grating.grating.period = RCW.grating.grating.period

; Graded boundary between materials [um] <double>
RCW.grating.grating.boundary = 0
#RCW.grating.grating.boundary = RCW.grating.grating.boundary

; Incident medium <dielectric_function>
RCW.grating.grating.medium_i = (1,0)
#RCW.grating.grating.medium_i = RCW.grating.grating.medium_i

; Transmitted medium <dielectric_function>
$RCW.grating.grating.medium_t = silicon

; Line material <dielectric_function>
$RCW.grating.grating.material = silicon

; Space between lines <dielectric_function>
RCW.grating.grating.space = (1,0)
#RCW.grating.grating.space = RCW.grating.grating.space

; Height of grating <double>
RCW.grating.grating.height = depth
#RCW.grating.grating.height = RCW.grating.grating.height

; Width of top of line [um] <double>
RCW.grating.grating.topwidth = period*duty_cycle
#RCW.grating.grating.topwidth = RCW.grating.grating.topwidth

; Width of bottom of line [um] <double>
RCW.grating.grating.bottomwidth = period*duty_cycle+depth*tan(sidewall_angle*deg)
#RCW.grating.grating.bottomwidth = RCW.grating.grating.bottomwidth

; Shift of bottom relative to top [um] <double>
RCW.grating.grating.offset = 0+iteration*1E-16
#RCW.grating.grating.offset = RCW.grating.grating.offset

; Number of levels <int>
RCW.grating.grating.nlevels = 1
#RCW.grating.grating.nlevels = RCW.grating.grating.nlevels

; Root mean square roughness [um] <double>
RCW.grating.rms = rms_roughness
#RCW.grating.rms = RCW.grating.rms

; Correlation length [um] <double>
RCW.grating.clength = clength
#RCW.grating.clength = RCW.grating.clength

; Roughness exponent <double>
RCW.grating.exponent = exponent
#RCW.grating.exponent = RCW.grating.exponent

; Mode:0 for line edge roughness1 for line width roughness2 for line position roughness <int>
RCW.grating.rmode = 0

```

```

#RCW.grating.rmode = RCW.grating.rmode

$RCW.grating.SaveGratingImage = corr_020_exp_05_rms_025.img

END

VARY:
  FOR iteration FROM 1 TO 15 STEP 1
  FOR thetai FROM 12 TO 72 STEP 4
END

INTEGRALS:
  I = DIFFERENTIAL
    CENTER = (thetas*deg,phis*deg)
    POL = (1,0,0,0); Unpolarized
    END
  Q = DIFFERENTIAL
    CENTER = (thetas*deg,phis*deg)
    POL = (0,1,0,0)
    END
  U = DIFFERENTIAL
    CENTER = (thetas*deg,phis*deg)
    POL = (0,0,1,0)
    END
  V = DIFFERENTIAL
    CENTER = (thetas*deg,phis*deg)
    POL = (0,0,0,1)
    END
  Rs = DIFFERENTIAL
    CENTER = (thetas*deg,phis*deg)
    POL = (0.5,0.5,0,0) ; S-polarized
    END
  Rp = DIFFERENTIAL
    CENTER = (thetas*deg,phis*deg)
    POL = (0.5,-0.5,0,0) ; P-polarized
    END
END

OUTPUTS:
  1 Rs=2*Rs*detector
  2 Rp=2*Rp*detector
  3 RI=I*detector
  4 RQ=Q*detector
  5 RU=U*detector
  6 RV=V*detector
END

FILES:
  ;
  results = ""

  ;
  listing = ""

END

```

For the 1D RCWA simulations using the EMA layer the RCW\_BRDF\_Model was used. The refractive index values for the effective medium layer are calculated using the “Aniso\_Bruggeman“ MATLAB™ script in Appendix F and assigned from a list file using the commands “@variable\_fill\_variable\_depolarization\_index\_list(index,6)”, etc.

```
; Rigorous coupled wave theory for a grating, form fitted into a BRDF_Model
MODEL = RCW_BRDF_Model
```

```
VARIABLES:
```

```
;
pi = 4*atan(1)

;
deg = pi/180

; Half angle over which BRDF is spread for a delta-function
halfangle = 0.01 ; Half angle over which BRDF is spread for a delta-function

; The solid angle collected by the detector
detector = pi*halfangle^2 ; The solid angle collected by the detector

; Incident Angle in degrees
thetai = 80 ; Incident Angle in degrees

; 0 for s, 90 for p
inpol = 45 ; 0 for s, 90 for p

; Period of the grating
period = 0.2 ; Period of the grating

; Depth of the grating
depth = 0.2 ; Depth of the grating

; Fraction of period filled with grating medium
duty_cycle = 0.5 ; Fraction of period filled with grating medium

; Sidewall Angle in degrees
sidewall_angle = 0 ; Sidewall Angle in degrees

; Wavelength of the light in vacuum
wavelength = 0.6328 ; Wavelength of the light in vacuum

; p-v deviation from nominal
pv_roughness = 0.005 ; p-v deviation of the roughness from the nominal profile

; p-v deviation from nominal
roughness_period = 2 ; period of the roughness variation

; Rotation angle of sample in degrees
```

```

sample_rotation = 0 ; Rotation angle of sample in degrees

; Diffraction order
n = 0 ; Diffraction order

; Diffraction equation for x
k.x = sind(thetai)+n*wavelength/period*cosd(sample_rotation) ; Diffraction equation for x

; Diffraction equation for y
k.y = n*wavelength/period*sind(sample_rotation) ; Diffraction equation for y

; Azimuthal angle of diffraction
phis = atan2d(k.y,k.x) ; Azimuthal angle of diffraction

;
thetas = thetai

;
roughness_layer_thickness_fraction = 0.01

;
fill_factor = 0.5

;
#quiet = 1

;
minsamples = 1

;
differential = (2*deg)^2

;
incidentangle = thetai*deg

;
incidentpol = (1,cos(2*inpol*deg),sin(2*inpol*deg),0)

;
rotation = sample_rotation*deg

; Wavelength [um] <double>
lambda = wavelength
#lambda = lambda

; index count
index = 1

; Substrate <dielectric_function>
$substrate = silicon

; (0) for Reflection or (1) for Transmission <int>
type = 0
#type = type

```

```

; Use old method for epsilon matrix <int>
oldmethod = 0
#oldmethod = oldmethod

; Half angle of diffraction cone [rad] <double>
alpha = halfangle
#alpha = alpha

; Maximum order <int>
order = 10
#order = order

; Grating <Grating_Ptr>
$grating = Generic_Grating

; Period of the grating [um] <double>
grating.period = 1
#grating.period = grating.period

; Graded boundary between materials [um] <double>
grating.boundary = 0
#grating.boundary = grating.boundary

; Incident medium <dielectric_function>
grating.medium_i = (1,0)
#grating.medium_i = grating.medium_i

; Transmitted medium <dielectric_function>
$grating.medium_t = silicon

; Assign index values from file
rnx = @variable_fill_variable_depolarization_index_list(index,6)
rny = @variable_fill_variable_depolarization_index_list(index,8)
rnz = @variable_fill_variable_depolarization_index_list(index,10)
inx = @variable_fill_variable_depolarization_index_list(index,7)
iny = @variable_fill_variable_depolarization_index_list(index,9)
inz = @variable_fill_variable_depolarization_index_list(index,11)

; Filename <string>
$grating.filename = Variable_ANISO_BRUG.ggd

; Parameter string <string>
grating.pstring =
(period,depth,period*duty_cycle,sidewall_angle,sidewall_angle,depth/2,1,roughness_layer_thickn
ess_fraction*period/2,fill_factor,rnx,rny,rnz,inx,iny,inz)
#grating.pstring = grating.pstring

; Approximate number of levels <int>
grating.nlayers = 20
#grating.nlayers = grating.nlayers

```

END

VARY:

```

;
mpi_FOR index FROM 66 TO 665 BY 1

;
FOR roughness_layer_thickness_fraction FROM 0.05 TO .15 BY 0.0025

;
FOR thetai FROM 0 TO 90 BY 2

END

INTEGRALS:
I = DIFFERENTIAL
  CENTER = (thetas*deg,phis*deg)
  POL = (1,0,0,0); Unpolarized
  END
Q = DIFFERENTIAL
  CENTER = (thetas*deg,phis*deg)
  POL = (0,1,0,0)
  END
U = DIFFERENTIAL
  CENTER = (thetas*deg,phis*deg)
  POL = (0,0,1,0)
  END
V = DIFFERENTIAL
  CENTER = (thetas*deg,phis*deg)
  POL = (0,0,0,1)
  END
Rs = DIFFERENTIAL
  CENTER = (thetas*deg,phis*deg)
  POL = (0.5,0.5,0,0) ; S-polarized
  END
Rp = DIFFERENTIAL
  CENTER = (thetas*deg,phis*deg)
  POL = (0.5,-0.5,0,0) ; P-polarized
  END

END

OUTPUTS:
  1 Rs=2*Rs*detector
  2 Rp=2*Rp*detector
  3 RI=I*detector
  4 RQ=Q*detector
  5 RU=U*detector
  6 RV=V*detector

END

FILES:
;
results = ""

;
listing = ""

END

```

## APPENDIX F: MATLAB™ m-Files

A self-affine functions were used to describe edge roughness in Chapter 2 and Chapter 4. A self-affine function has an autocorrelation function ( $A(\rho)$ ) of the form:

$$A(\rho) \propto \exp[-(\rho/\xi)^{2\alpha}] \quad (\text{F.1})$$

where  $\rho$  is the distance between two points along the nominal edge,  $\xi$  is the linear correlation length of the rough edge, and  $\alpha$  is called the roughness exponent. The roughness exponent, also referred to as the Hurst exponent, is related to the fractal dimension of the edge and can be used to describe the relative amount of high frequency content in the power spectrum. Various roughness profiles with known statistics were created using the procedure outlined by Zhao et. al.<sup>137</sup>. In summary, the procedure involves:

1. Calculating the auto-correlation (ACF) function for the desired profile
2. Using the Wiener-Khinchin theorem to calculate the power spectral density (PSD) of the profile.
3. Multiplying the square root of the PSD by a random phase function.
4. Taking the inverse Fourier transform to recover a random profile in the spatial domain with a known PSD.

The following MATLAB™ m-file was used to generate these functions:

```
function Profile = calcAffineProfile(corr_length,roughness_exponent,N)

    if nargin < 3
        N = 2048;
    end
    if nargin < 2
        roughness_exponent = 1;
    end
    if nargin < 1
        corr_length = 0.05;
    end

    % Generate ACF
    s = linspace(0,1,(N/2)+1);
    ACF = exp(-(abs(s./2)./corr_length).^(2*roughness_exponent));
    symmetric_ACF = [ACF,fliplr(conj(ACF((2:(N/2)))))];

    % Calculate the PSD
    PSD = fft(symmetric_ACF);

    % Generate a White Noise Function
    rand('state', sum(100*clock));
    White_Noise = (rand(1,N)-0.5);

    % Take the Fourier transform of the white noise
    ftwn = fft(White_Noise);

    % Normalize the Fourier transform of the white noise
    % and make the function complex conjugate symmetric
    nftwn = ftwn./abs(ftwn);

    % Multiply the sqrt of the PSD by the symmetric normalized
    % Fourier Transform of the white noise function
    fty = sqrt(PSD).*nftwn;

    % Take the inverse Fourier transform
    y = ifft(fty);

    % Normalize the answer and subtract the mean
    % and clean up small imaginary part
    x = linspace(0,1,N);
    y = y./calcrms(y);
    y = y - mean(y);
    y = real(y);

    Profile.x = x;
```

```
Profile.y = y;
```

The anisotropic Bruggeman effective medium approximation (ABEMA) was developed in Chapter 3 and used in chapter 4 to model LER. The following MATLAB™ m-file calculates the effective indices (nf) from the indices of the constituent materials (n1 and n2), the fill factors (f1 and f2), and from the depolarization factors (Lx, Ly, and Lz) that describe the ABEMA:

```
function nf = Aniso_Bruggeman(n1, f1, n2, f2, Lx, Ly, Lz)

    if nargin < 2
        f1 = 0.5;
    end
    if nargin < 3
        n2 = 1;
    end
    if nargin < 4
        f2 = 1- f1;
    end
    if nargin < 5
        Lx = 0.5;
    end
    if nargin < 6
        Ly = 1-Lx;
    end
    if nargin < 7
        Lz = 0;
    end

    ax = (f1+f2)*(Lx-1);
    bx = f1.*(n1.^2-Lx.*n1.^2-Lx.*n2.^2)+f2.*(n2.^2-Lx.*n1.^2-
Lx.*n2.^2);
    cx = (f1+f2).*Lx.*n1.^2.*n2.^2;
    if ax == 0
        ax = 0.0000001;
    end

    ay = (f1+f2)*(Ly-1);
    by = f1.*(n1.^2-Ly.*n1.^2-Ly.*n2.^2)+f2.*(n2.^2-Ly.*n1.^2-
Ly.*n2.^2);
    cy = (f1+f2).*Ly.*n1.^2.*n2.^2;
    if ay == 0
        ay = 0.0000001;
    end

    az = (f1+f2)*(Lz-1);
    bz = f1.*(n1.^2-Lz.*n1.^2-Lz.*n2.^2)+f2.*(n2.^2-Lz.*n1.^2-
Lz.*n2.^2);
    cz = (f1+f2).*Lz.*n1.^2.*n2.^2;
    if az == 0
        az = 0.0000001;
    end
end
```

```

nxn = ((-bx-(bx.^2-4*ax.*cx).^ (1/2))/(2*ax)).^(1/2);
nyn = ((-by-(by.^2-4*ay.*cy).^ (1/2))/(2*ay)).^(1/2);
nzn = ((-bz-(bz.^2-4*az.*cz).^ (1/2))/(2*az)).^(1/2);

nxp = ((-bx+(bx.^2-4*ax.*cx).^ (1/2))/(2*ax)).^(1/2);
nyp = ((-by+(by.^2-4*ay.*cy).^ (1/2))/(2*ay)).^(1/2);
nzp = ((-bz+(bz.^2-4*az.*cz).^ (1/2))/(2*az)).^(1/2);

nx = zeros(size(n1));
ny = zeros(size(n1));
nz = zeros(size(n1));
for i = 1:size(nxn)
    if angle(nxn(i))>= 0
        nx(i) = nxn(i);
    else
        nx(i) = nxp(i);
    end
    if angle(nyn(i))>= 0
        ny(i) = nyn(i);
    else
        ny(i) = nyp(i);
    end
    if angle(nzn(i))>= 0
        nz(i) = nzn(i);
    else
        nz(i) = nzp(i);
    end
end
nf = [nx,ny,nz];

```